Department of Physics and Astronomy

Heidelberg University

Master thesis

in Physics

submitted by

Lennart Henning Uecker

born in St. Wendel

2022

Investigation of the effect of material interaction on neutral charm meson mixing at the LHCb experiment

This Master thesis has been carried out by

Lennart Henning Uecker

at the

Physikalisches Institut

under the supervision of

Prof. Dr. Stephanie Hansmann-Menzemer

Prof. Dr. Marco Gersabeck

(University of Manchester)

Untersuchung des Effekts von Materialinteraktionen auf die Mischung neutraler Charm-Mesonen am LHCb-Experiment

Diese Arbeit präsentiert die erste Messung des Effektes von Material auf die Mischung von D^0- $\overline{D}^0$ Mesonen. Die Messung basiert auf einem Datensatz von Proton-Proton Kollisionen, aufgenommen durch das LHCb-Experiment und mit einer Größe entsprechend 5.6 fb^{-1} integrierter Luminosität. Wir messen die Mischung von D^0 Mesonen, die in K und π zerfallen, mittels der WS-zu-RS Methode. Dabei verwenden wir D^0 Mesonen deren Flavour-Zustand in einem Zerfall der starken Wechselwirkung oder in einem semileptonischen schwachen Zerfall bestimmt wurde.
In einer zeitabhängigen Messung werden die Mischungsparameter (R_D, y', x'^2) bestimmt, dabei werden keine signifikanten Abweichungen zu den Welt-Durschnittswerten festgestellt:

$$\begin{aligned}
R_D &= (3.5 \pm 0.8 \pm 0.2)\cdot 10^{-3},\\
y' &= (6\ {}^{+8}_{-10}\ {}^{+2}_{-4})\cdot 10^{-3},\\
x'^2 &= (0.0\ {}^{+0.4}_{-0.2}\ {}^{+0.2}_{-0.1})\cdot 10^{-3}.
\end{aligned}$$

In zeitintegrierten Messungen der WS-zu-RS Verhältnisse, getrennt nach Art der Flavour-Bestimmung, wird keine Abweichung vom Erwartungswert unter der Annahme von Mischung im reinem Vakuum gefunden.

Investigation of the effect of material interaction on neutral charm meson mixing at the LHCb experiment

This work presents the first measurement of the influence of material interactions on D^0- $\overline{D}^0$ mixing. The data sample corresponds to an integrated luminosity of 5.6 fb^{-1} of proton-proton collisions collected during Run 2 by the LHCb experiment. We observe the flavour mixing of D^0 mesons using their decay to $K\pi$ final states with the WS-to-RS method. We utilise flavour-tagged charm decays produced in both prompt and semileptonic processes.
In a time-dependent measurement, we measure the mixing parameters (R_D, y', x'^2) and find no significant tension to the world-average value:

$$\begin{aligned}
R_D &= (3.5 \pm 0.8 \pm 0.2)\cdot 10^{-3},\\
y' &= (6\ {}^{+8}_{-10}\ {}^{+2}_{-4})\cdot 10^{-3},\\
x'^2 &= (0.0\ {}^{+0.4}_{-0.2}\ {}^{+0.2}_{-0.1})\cdot 10^{-3}.
\end{aligned}$$

In time-integrated measurements of the WS-to-RS ratio, separated by tag sources, we find no evidence of deviations from the mixing effect explained purely by mixing in vacuum.

Contents

1 Introduction

The study of flavoured neutral mesons has played a crucial role in the development of the Standard Model of particle physics (SM). In 1947 the neutral Kaon was discovered at the University of Manchester by Rochester and Butler [1]. With the development of strangeness as a quantum number, Gell-Mann and Pais first proposed to describe the neutral Kaon as a two-state quantum system, including distinct mass eigenstates with different mass and lifetimes [2]. This discussion also included the description of the $K^0 \leftrightarrows \pi^+\pi^- \leftrightarrows \overline{K}^0$ transition, *i.e.* a flavour changing neutral current via intermediate particles. This prompted a follow-up paper from A. Pais and O. Piccioni [3] proposing an experimental setup that would regenerate a K^0_S component out of a pure K^0_L beam by shooting the K^0_L beam on a target. A pure K^0_L beam could be experimentally produced, enabling the experiment. These experiments started bearing fruits with R.H. Good *et al.* measuring the mass difference for the first time [4] and the Nobel Prize-winning discovery of *CP* violating in neutral Kaon mixing by J. H. Christenson, J. W. Cronin, V. L. Fitch and R. Turley [5] in 1964.

The mixing phenomenon has also been observed for B^0- $\overline{B}^0$ [6], B^0_s- $\overline{B}^0_s$ [7] and D^0- $\overline{D}^0$ [8] mesons. Measurements of the time dependence of mixing are an important test of the Standard Model because virtual particles not included in the Standard Model could enhance the mixing rates. This approach has been successful before. The larger-than-expected B^0- $\overline{B}^0$ mixing rate observed by the ARGUS collaboration was an early indication of the large mass of the top quark.

The regeneration effect has, to our knowledge, never been studied for any of the heavier meson pairs, as they cannot be conveniently produced as a beam, and they decay faster than K^0_L mesons. Both make constructing a regeneration experiment, similar to the neutral Kaon ones, unfeasible.

However, at the LHCD^0 mesons[1] are produced in great abundance and the LHCb detector has a potential target stand-in very close to the production point. Therefore, this analysis proposes to use the existing, large set of reconstructed D^0 decays from the LHCb experiment to search for those D^0 mesons that have passed through our target stand-in, the RF-foils, to analyse their mixing behaviour.

In addition, we believe this type of analysis is potentially promising for Run 3 of the LHCb and beyond, as the number of candidates improves based on an increased luminosity, higher trigger efficiency and the new RF-foils that are positioned closer to the interaction region. All this combines to a significant jump in the number of candidates for a follow-up analysis using Run 3 data.

In chapter 2 of this thesis, we introduce the Standard Model of particle physics,

[1] The inclusion of charge-conjugate processes is implied throughout this thesis unless explicitly stated otherwise.

with a focus on those parts relevant to neutral meson mixing and in A we present a possible extension of the mixing framework to include the effect of material interactions. In chapter 3 we introduce the relevant experimental devices, the LHC particle accelerator and the LHCb detector. Chapter 4 gives a brief overview of the measurement. Chapter 5 elaborates on the creation of models for the RF-foils, and chapter 6 on the treatment and selection of the data sample used in the analysis. In chapter 7 we explain how the WS-to-RS ratios are determined and in chapter 8 we explore how peaking backgrounds influence these ratios. In chapter 9 we explore the effect of secondary D decay contamination of the sample. Finally, we determine the mixing parameters in a time dependent fit and perform a time-integrated test of mixing in excess of vacuum mixing in chapter 10.

2 Theory

This chapter presents an overview of the Standard Model of particle physics. Special attention is given to flavour physics, which describes neutral meson mixing and regeneration. These effects are central to the measurements presented in this thesis.

2.1 The Standard Model of particle physics

The Standard Model of particle physics is a quantum field theory combining three of the four fundamental forces:

- The electromagnetic force describes the interaction of electrically charged particles. Its effects are the most visible on a macroscopic scale, such as electric currents and light.
- The strong force describes interactions of quarks and the formation of hadrons.
- The weak force is best known for its role in radioactive decays and is fundamental to flavour physics.

The fourth fundamental force - not included in the Standard Model of particle physics - is the gravitational force. On the scale of particle physics, gravitational interaction cross sections are many orders of magnitude too small to be observed.

The Standard Model of particle physics is widely accepted and tested in varied measurements of particles (listed in table 2.1) and their interactions.

2.2 Foundation of the Standard Model

The Standard Model Lagrangian is often written down in a very compact form:

$$
\begin{aligned}
\mathscr{L}_{\mathrm{SM}} = & -\frac{1}{4} F_{\mu\nu} F^{\mu\nu} \\
& + i\bar{\psi} \not{D} \psi \\
& + \psi_i Y_{ij} \psi_j \phi + \text{h.c.} \\
& + \left| D_\mu \phi \right|^2 + \mu^2 \phi^\dagger \phi - \lambda (\phi^\dagger \phi)^2 .
\end{aligned}
\tag{2.1}
$$

The Lagrangian incorporates all the interactions and fundamental particles of the Standard Model and we explain the relevant individual terms in this chapter. The Lagrangian is locally gauge invariant with respect to the group:

Table 2.1: The particle content of the Standard Model. Experimentally determined masses taken from [9].
† Neutrinos are massless particles in the Standard Model. Experimental observation of neutrino mixing necessitates a mass on which upper limits have been established. A detailed review can be found in chapter 14 of Ref. [9].

Fermions

	Quarks			*Leptons*		
Generation	Type	Q [e]	Mass	Type	Q [e]	Mass
1	u	2/3	2.2 MeV/c^2	ν_e	0	$0^\dagger$
	d	-1/3	4.7 MeV/c^2	e^-	-1	0.511 MeV/c^2
2	c	2/3	1.27 GeV/c^2	ν_μ	0	$0^\dagger$
	s	-1/3	93 MeV/c^2	μ	-1	105.7 MeV/c^2
3	t	2/3	172.7 GeV/c^2	ν_τ	0	$0^\dagger$
	b	-1/3	4.18 GeV/c^2	τ	-1	1777 MeV/c^2

Bosons

Type	Q [e]	Spin	Mass
γ	0	1	0
g	0	1	0
$W^\pm$	±1	1	80.4 GeV/c^2
Z	0	1	91.2 GeV/c^2
H^0	0	0	125.3 GeV/c^2

$$G_{\mathrm{SM}} = SU(3)_C \otimes SU(2)_L \otimes U(1)_Y. \tag{2.2}$$

$SU(3)_C$ describes strong interactions and $SU(2)_L \otimes U(1)_Y$ the electroweak interactions, as the Standard Model includes a unification of electromagnetic and weak forces.

From these gauge groups arise the physical spin 1 gauge bosons of the Standard Model. The generators of the symmetry groups correspond to the gauge bosons. Thus there are eight gluons associated with $SU(3)_C$, these are the massless bosons propagating the strong force. They only interact with particles that carry a charge under $SU(3)_C$, *i.e.* the quarks and gluons. The coupling constant of the strong force is g_S. $SU(2)_L$ has three massless bosons W_i $(i = 1, 2, 3)$ coupling to the T_3 component of the weak isospin and the associated coupling constant g. The weak isospin is deeply connected to the chiral structure of the Standard Model. The fact that only left-handed fermions carry weak isospin explains the subscript 'L' in $SU(2)_L$. $U(1)_Y$ has one massless boson B coupling to the weak hypercharge Y and the associated coupling constant is g'.

The Standard Model Lagrangian also contains matter fields ψ. These represent spin 1/2 particles (fermions), three generations of quarks and leptons, namely:

$$\begin{aligned}
\text{Quarks: } Q_L^i &= \left\{ \begin{pmatrix} u_L \\ d_L \end{pmatrix}, \begin{pmatrix} c_L \\ s_L \end{pmatrix}, \begin{pmatrix} t_L \\ b_L \end{pmatrix} \right\}, \\
U_R^i &= (u_R, c_R, t_R), \\
D_R^i &= (d_R, s_R, b_R), \\
\text{Leptons: } L_L^i &= \left\{ \begin{pmatrix} \nu_{e,L} \\ e_L^- \end{pmatrix}, \begin{pmatrix} \nu_{\mu,L} \\ \mu_L^- \end{pmatrix}, \begin{pmatrix} \nu_{\tau,L} \\ \tau_L^- \end{pmatrix} \right\}, \\
E_R^i &= (e_R^+, \mu_R^+, \tau_R^+).
\end{aligned} \tag{2.3}$$

Here the index i enumerates the generations and the subscripts 'L', 'R' indicate chirality. The three generations carry the same charges under the gauge group and differ only in their masses. Particles within each generation are classified according to their representation under the three respective gauge groups.

$$\begin{aligned}
&\text{Quarks: } Q_L^i\left(3, 2, +\frac{1}{6}\right) \quad U_R^i\left(3, 1, +\frac{2}{3}\right) \quad D_R^i\left(3, 1, -\frac{1}{3}\right) \\
&\text{Leptons: } L_L^i\left(1, 2, -\frac{1}{2}\right) \qquad\qquad\qquad\qquad E_R^i\left(1, 1, -1\right)
\end{aligned} \tag{2.4}$$

For example, Q_L^i is a triplet under $SU(3)_C$, a doublet under $SU(2)_L$ and has $U(1)_Y$ hypercharge $+\frac{1}{6}$, while E_R^i is a singlet under both $SU(3)_C$ and $SU(2)_L$, thus not participating in either interaction. For the $SU(2)_L$ doublets Q_L^i and L_L^i it is also worthwhile to indicate the weak isospin T_3, the quantum number associated to $SU(2)_L$ symmetry. The left-handed up-type quarks carry $T_3 = +\frac{1}{2}$, as do the neutrinos, while the left-handed down-type quarks as well as e^-, μ^-, τ^- carry $T_3 = -\frac{1}{2}$, all remaining fermions have $T_3 = 0$.

The final piece to the Standard Model is the Higgs sector. The spin 0 Higgs field ϕ is the only known scalar field. It is a complex $SU(2)$ scalar doublet:

$$\phi(1, 2, +\frac{1}{2}) = \frac{1}{\sqrt{2}} \begin{pmatrix} \phi^+ \\ \phi^0 \end{pmatrix}. \tag{2.5}$$

Looking at $\mathscr{L}_{\mathrm{SM}}$ we see that the Higgs field has a gauge term, interacting with the electroweak gauge bosons, a potential term resulting in self-interaction and a Yukawa term coupling it to the fermion fields.

In the potential term:

$$V(\phi) = \mu^2 \phi^\dagger \phi - \lambda(\phi^\dagger \phi)^2, \tag{2.6}$$

$\mu^2 > 0$ and $\lambda > 0$ induce spontaneous symmetry breaking (SSB). When calculating the expectation value of the Higgs field,

$$\langle \phi^\dagger \phi \rangle = -\frac{\mu^2}{\lambda} \equiv \frac{v^2}{2}, \tag{2.7}$$

it yields a non-vanishing vacuum expectation value (VEV). The ground state of the Higgs field becomes:

$$\phi = \frac{1}{\sqrt{2}} \begin{pmatrix} 0 \\ v \end{pmatrix}. \tag{2.8}$$

The degeneracy of the minimum lies in the complex phase of v. This non-vanishing VEV induces SSB and we can absorb the complex phase of v as a $U(1)$ gauge freedom.

The spontaneous breaking of $SU(2)_Y \otimes U(1)_Y$ symmetry is fundamental to explain the massive fermions and bosons of the Standard Model [10, 11]. The gauge term of the Higgs field gives rise to mass terms of the weak and electromagnetic gauge bosons, which are linear combinations of the electroweak gauge bosons.

$$W^\pm = (W_1 \pm iW_2)/\sqrt{2}, \tag{2.9}$$
$$Z = \cos\theta_W W_3 - \sin\theta_W B, \tag{2.10}$$
$$\gamma = \sin\theta_W W_3 + \cos\theta_W B. \tag{2.11}$$

Here, $W^{\pm}$ and Z gain masses while the photon remains massless. In short, the VEV breaks the electroweak symmetry:

$$SU(2)_L \otimes U(1)_Y \stackrel{\text{SSB}}{\to} U(1)_{\text{EM}}. \tag{2.12}$$

The electric charge appears as the linear combination $Q = Y + T_3$ of hypercharge and weak isospin. After SSB, the Higgs field also gives rise to the masses of the fermions via the Yukawa coupling. The coupling to the Higgs field is described in flavour space by the 3 matrices Y_U, Y_D, Y_E.

$$\mathscr{L}_{\text{Yukawa}} = -\sum_{i,j} \left\{ Y_U^{ij} \bar{Q}_L^i U_R^j \tilde{\phi} + Y_D^{ij} \bar{Q}_L^i D_R^j \phi + Y_E^{ij} \bar{L}_L^i E_R^j \phi + \text{h.c.} \right\} \tag{2.13}$$

Here we introduced the differently charged conjugate isodoublet $\tilde{\phi} = i\sigma_2 \phi^*$, which transforms identically under $SU(2)_L$ but carries opposite hypercharge and allows us to give masses to the up-type quarks.

$$\tilde{\phi}(1, 2, -\frac{1}{2}) = \begin{pmatrix} \frac{1}{\sqrt{2}}(v + h^*(x)) \\ -h^- \end{pmatrix} \tag{2.14}$$

Notably, no mass term for neutrinos can be constructed due to the lack of a right-handed neutrino field. After SSB, the Higgs field takes on its vacuum expectation value, thus giving masses to the quarks and the charged leptons:

$$\mathscr{L}_{\text{Mass}} = -\frac{v}{\sqrt{2}} \sum_{i,j} \left\{ Y_U^{ij} \bar{U}_L^i U_R^j + Y_D^{ij} \bar{D}_L^i D_R^j + Y_E^{ij} \bar{E}_L^i E_R^j + \text{h.c.} \right\} \tag{2.15}$$

Here we split the left-handed quark field $Q_L^i = \{U_L^i, D_L^i\}^T$ and single out the charged part of L_L as E_L to clarify that the mass terms always involve the left- and right-handed fermion fields.

The mass terms can now be identified as:

$$m_X^{ij} = \frac{v}{\sqrt{2}} Y_X^{ij} \tag{2.16}$$

The Yukawa matrices Y are in general complex and non-diagonal. This gives rise to the flavour structure of the Standard Model, which is described in detail in the following chapter.

2.3 Introduction to flavour physics

The flavour structure of the quark sector is fundamental to this thesis. In the following, we focus on the quark fields, while for the lepton fields, much is equivalent. The first step in explaining the flavour structure is finding a basis for the fermion fields that yields diagonal mass terms. This can be achieved with the unitary transformations

$$\begin{aligned} U_R &\to V_{u_R} u_R, \qquad & U_L &\to V_{u_L} u_L, \\ D_R &\to V_{d_R} d_R, \qquad & D_L &\to V_{d_L} d_L. \end{aligned} \tag{2.17}$$

The Yukawa matrices are thus diagonalised as

$$Y_u = V_{u_L}^{\dagger} Y_U V_{u_R}, \qquad Y_d = V_{d_L}^{\dagger} Y_D V_{d_R}. \tag{2.18}$$

The mass matrices are then easily formed.

$$\mathbf{M_u} = \frac{v}{\sqrt{2}} Y_u = \begin{pmatrix} m_u & 0 & 0 \\ 0 & m_c & 0 \\ 0 & 0 & m_t \end{pmatrix}, \quad \mathbf{M_d} = \frac{v}{\sqrt{2}} Y_d = \begin{pmatrix} m_d & 0 & 0 \\ 0 & m_s & 0 \\ 0 & 0 & m_b \end{pmatrix} \tag{2.19}$$

These masses are free parameters in the Standard Model. However, experimentally, a mass hierarchy has been found, $m_u \ll m_c \ll m_t$ and $m_d \ll m_s \ll m_b$, see table 2.1.

Since this transformation requires different treatment of the u_L and d_L type quarks, both parts of the same Q_L $SU(2)$ doublet, charged weak currents are not invariant under this transformation. The quark gauge term of $\mathscr{L}_{SM}$ (second line in eq. 2.1) includes the weak charged current term, here written in flavour basis

$$\mathscr{L}_{\text{Gauge}}^{\text{CC, q}} = \frac{g}{\sqrt{2}} \left\{ \bar{U}_L \gamma_\mu W^{+\mu} D_L + \bar{D}_L \gamma_\mu W^{-\mu} U_L \right\} \tag{2.20}$$

$$\overset{2.17}{=} \frac{g}{\sqrt{2}} \{ \bar{u}_L \underbrace{V_{u_L}^{\dagger} V_{d_L}}_{V_{\text{CKM}}} \gamma_\mu W^{+\mu} d_L + \bar{d}_L \underbrace{V_{d_L}^{\dagger} V_{u_L}}_{V_{\text{CKM}}^{\dagger}} \gamma_\mu W^{-\mu} U_L \}. \tag{2.21}$$

By applying the transformations into the mass basis, the flavour mixing structure emerges and we see that it is governed by the Cabibbo-Kobayashi-Maskawa (CKM) matrix [12, 13]. In general, a 3×3 complex matrix has 18 free parameters. The unitarity condition reduces this to nine free parameters. Five of these can be absorbed into the six quark fields as unphysical phases. The remaining four free parameters are represented as three Euler angles $(\theta_{12}, \theta_{23}, \theta_{13})$ explaining the flavour transitions and one CP-violating phase (δ_{13}). In terms of these parameters, V_{CKM} is given as:

$$V_{\mathrm{CKM}} = \begin{pmatrix} 1 & 0 & 0 \\ 0 & \cos\theta_{23} & \sin\theta_{23} \\ 0 & -\sin\theta_{23} & \cos\theta_{23} \end{pmatrix} \begin{pmatrix} \cos\theta_{13} & 0 & \sin\theta_{13}e^{-i\delta_{13}} \\ 0 & 1 & 0 \\ -\sin\theta_{13}e^{i\delta_{13}} & 0 & \cos\theta_{13} \end{pmatrix} \begin{pmatrix} \cos\theta_{12} & \sin\theta_{12} & 0 \\ -\sin\theta_{12} & \cos\theta_{12} & 0 \\ 0 & 0 & 1 \end{pmatrix}. \tag{2.22}$$

A hierarchical structure of the CKM matrix has been observed experimentally, where it is diagonal at first approximation. The very common Wolfenstein-parametrisation [14] highlights this fact. New parameters are introduced in terms of the standard parameters:

$$\begin{aligned} \lambda &\equiv \sin\theta_{12}, \\ A\lambda^2 &\equiv \sin\theta_{23}, \\ A\lambda^3(\rho - i\eta) &\equiv \sin\theta_{13}e^{-i\delta_{13}}. \end{aligned} \tag{2.23}$$

This definition allows us to express V_{CKM} as a power series of $\lambda \equiv |V_{us}| \approx 0.23$,

$$V_{\mathrm{CKM}} = \begin{pmatrix} V_{ud} & V_{us} & V_{ub} \\ V_{cd} & V_{cs} & V_{cb} \\ V_{td} & V_{ts} & V_{td} \end{pmatrix} = \begin{pmatrix} 1-\frac{1}{2}\lambda^2 & \lambda & A\lambda^3(\rho - i\eta) \\ -\lambda & 1-\frac{1}{2}\lambda^2 & A\lambda^2 \\ A\lambda^3(1-\rho-i\eta) & -A\lambda^2 & 1 \end{pmatrix} + \mathcal{O}(\lambda^4), \tag{2.24}$$

and highlights that transitions within the same generation of quarks (*e.g.* $c \to s$) are favoured (Cabibbo-favoured (CF)) while transitions between generations of quarks are suppressed (Cabibbo-suppressed (CS)). The most suppressed transitions are the most extreme, *i.e.* $b \to u$ and $t \to d$.

2.4 The charm sector

This thesis focuses on the decays that involve the transition of a c quark to the lighter s and d quarks. The two prominent decays of this thesis are $D^0 \to K^-\pi^+$ and $D^0 \to K^+\pi^-$. Their dominant Feynman diagrams are depicted in figure 2.1. Since the $D^0 \to K^+\pi^-$ decay involves two off-diagonal CKM transitions, it is referred to as doubly Cabibbo suppressed (DCS). Both decays have the same hadronic final state but flipped charges. In this thesis, we name the Cabibbo favoured decay the Right-Sign (RS) decay and its DCS counterpart the Wrong-Sign (WS) decay.

If the D^0 is directly produced in the proton-proton collision, there is no way to differentiate between a Right-Sign decay of a D^0 or a Wrong-Sign decay of a $\overline{D}^0$. To gain knowledge about the flavour content of the neutral D^0 meson, it has to be

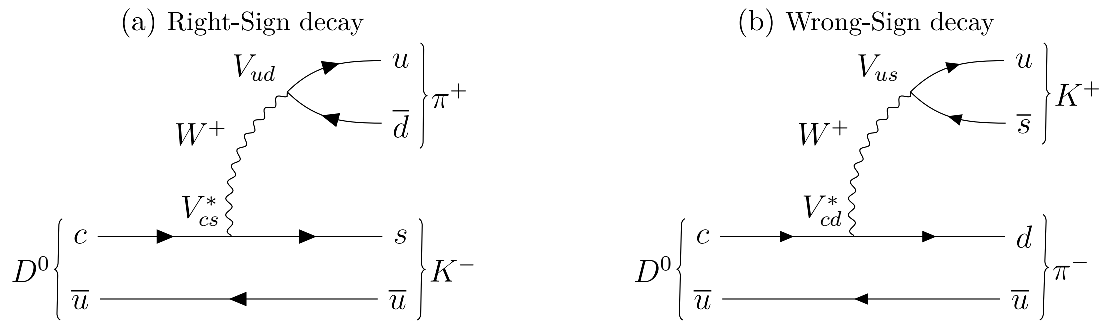

Figure 2.1: Feynman diagrams of both relevant decays for this thesis.

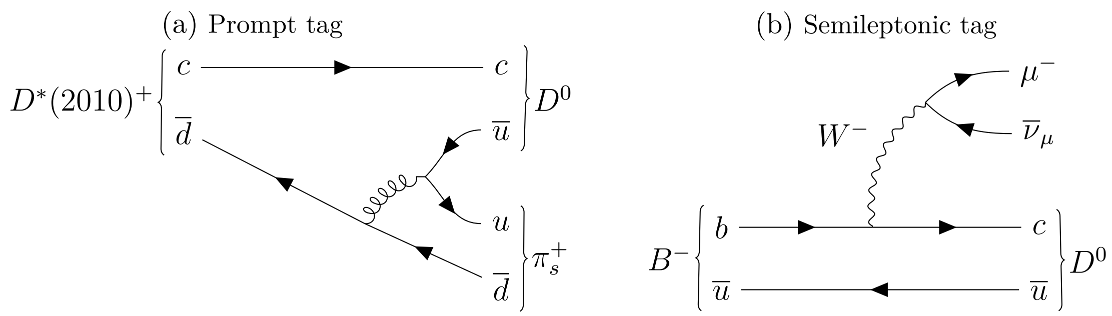

Figure 2.2: Feynman diagrams of the decays used to provide charm flavour tags in this analysis.

tagged. There are two types of flavour tags used in this analysis. The dominant Feynman diagrams of both decays are depicted in figure 2.2.

The prompt tagging procedure involves the strong decay of the excited $D^*(2010)^+$ meson[1] to a D^0 and a pion π^+. A positive charge on the soft pion corresponds to the production of an D^0, *i.e.* $C = +1$. Since the mass difference between D^{*+} and D^0 is $145.43\,\mathrm{MeV}/c^2$, only slightly above the pion mass ($m_{\pi^+} = 139.57\,\mathrm{MeV}/c^2$), the pion is called the soft pion π_s^+. As the D^{*+} decays via the strong interaction, it has a lifetime of less than 10^{-20}s, meaning its decay vertex is experimentally consistent with its production vertex, often the primary vertex.

The semileptonic tagging method relies on the semileptonic decay of a B meson. A negative charge on the muon indicates the production of a D^0 meson. Here the weak transition from a b quark to a c quark results in the production of a negatively charged muon. This decay is experimentally more difficult to reconstruct due to the missing energy of the neutrino component, which cannot be reconstructed.

Due to the different production cross section of charm and beauty and the branching fractions involved, prompt tagged events are about an order of magnitude more abundant.

[1] From here on abbreviated as D^{*+}

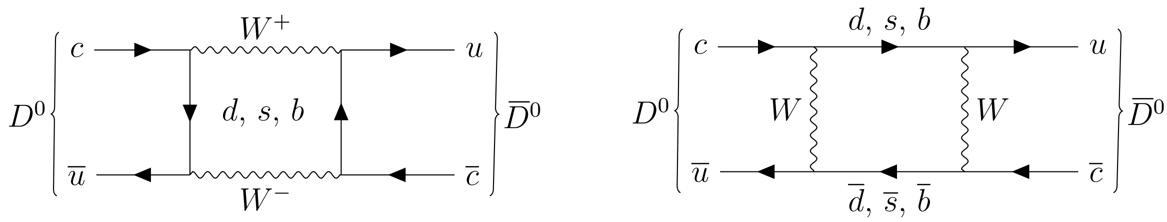

Figure 2.3: Short distance contributions to charm mixing.

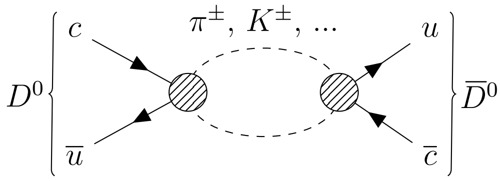

Figure 2.4: Long distance contribution to charm mixing.

2.5 Mixing in flavoured neutral mesons

Mixing describes the quantum-mechanical effect of neutral mesons transitions between flavour states, *e.g.* a $D^0 \to \overline{D}^0$ transition. The process has been observed in the four flavoured neutral meson pairs, namely K^0- $\overline{K}^0$, D^0- $\overline{D}^0$, B^0- $\overline{B}^0$ and B^0_s- $\overline{B}^0_s$. In the following, we use the generic name P^0- $\overline{P}^0$ as a stand-in with a generic flavour number P to describe the phenomenon in detail. While the mathematical description is equal for all four systems, the phenomenology differs widely between all four examples.

For flavoured neutral mesons, the mass eigenstates, *i.e.* the physical states that have well-defined masses and decay widths, do not coincide with the flavour eigenstates that they are produced in, yielding a quantum mechanical two-state system. We describe the general state $|\psi\rangle$ as a linear combination of the two flavour eigenstates:

$$|\psi\rangle = a(t)|P^0\rangle + b(t)|\overline{P}^0\rangle. \tag{2.25}$$

Since we are interested in $\Delta P = \pm 2$ transitions, it is useful to apply the Weisskopf-Wigner approximation [15, 16] by neglecting the flavour conserving strong and electromagnetic interactions, *i.e.* we assume to be at a time scale much larger than time scales related to those interactions. The time evolution of the state is governed by the Schrödinger-equation

$$i\hbar\frac{\partial}{\partial t}\psi = \mathscr{H}\psi, \tag{2.26}$$

with an effective 2×2 non-Hermitian Hamiltonian $\mathscr{H}$. It can be decomposed into a

Table 2.2: Constraints on the effective Hamiltonian $\mathscr{H}$ based on the Hermitian nature of the components and the imposition of the discrete symmetries *CP*, *CPT*.

Origin	**Constraints**	
CPT	$M_{11} = M_{22}$	$\Gamma_{11} = \Gamma_{22}$
CP	$M_{12} = M_{21} \in \mathbb{R}$	$\Gamma_{12} = \Gamma_{21} \in \mathbb{R}$
Hermitian	$M_{11,22} \in \mathbb{R}$	$\Gamma_{11,22} \in \mathbb{R}$
	$M_{12} = M_{21}^*$	$\Gamma_{12} = \Gamma_{21}^*$

Hermitian mass matrix $\mathbf{M}$ and an anti-Hermitian decay matrix $\frac{i}{2}\mathbf{\Gamma}$ [2]

$$\mathscr{H} = \mathbf{M} - \frac{i}{2}\mathbf{\Gamma} = \begin{pmatrix} M_{11} - \frac{i}{2}\Gamma_{11} & M_{12} - \frac{i}{2}\Gamma_{12} \\ M_{21} - \frac{i}{2}\Gamma_{21} & M_{22} - \frac{i}{2}\Gamma_{22} \end{pmatrix}. \tag{2.27}$$

Some constraints can be put on both matrices by imposing the discrete symmetries *CP*, and *CPT* as derived in chapter seven of [17]. Table 2.2 gives a list of the constraints. In the following, we will make use of the *CPT* constraints but will not assume that *CP* symmetry holds.

The off-diagonal mass matrix elements M_{12} and M_{21} describe the dispersive part of mixing transitions, *i.e.* via virtual (off-shell) intermediate states, the off-diagonal terms Γ_{12} and Γ_{21} describe the absorptive part of the transition, *i.e.* via real (on-shell) intermediate states. The diagonal elements of $\mathbf{\Gamma}$ yield the decay into real final states.

We calculate the eigenvalues of the effective Hamiltonian $\mathscr{H}$ and the corresponding eigenvectors to simplify the time evolution. The basis change to the mass eigenstate basis is given by

$$\begin{pmatrix} |P_1\rangle \\ |P_2\rangle \end{pmatrix} = \mathbf{Q} \begin{pmatrix} |P^0\rangle \\ |\overline{P}^0\rangle \end{pmatrix} \text{ with } \mathbf{Q} = \begin{pmatrix} p & q \\ p & -q \end{pmatrix}, \tag{2.28}$$

here $\mathbf{Q}$ is the matrix that diagonalises the Hamiltonian. The corresponding eigenvectors are

$$\begin{pmatrix} p \\ q \end{pmatrix}, \begin{pmatrix} p \\ -q \end{pmatrix}. \tag{2.29}$$

The parameters p, q are complex numbers satisfying

$$\frac{q}{p} = \sqrt{\frac{M_{21} - \frac{i}{2}\Gamma_{21}}{M_{12} - \frac{i}{2}\Gamma_{12}}} \qquad \text{and} \qquad |p|^2 + |q|^2 = 1. \tag{2.30}$$

[2] $\mathbf{\Gamma}$ itself is Hermitian.

We can express the eigenvalues $\lambda_{1,2}$ as a function of the elements of $\mathscr{H}$ as well as a function of the physical parameters, their masses $M_1,\ M_2$ and decay widths $\Gamma_1,\ \Gamma_2$.

$$\begin{aligned}
\lambda_1 = M_1 - \frac{i}{2}\Gamma_1 \quad &= M_{11} - \frac{i}{2}\Gamma_{11} + \frac{q}{p}\left(M_{12} - \frac{i}{2}\Gamma_{12}\right), \\
\lambda_2 = M_2 - \frac{i}{2}\Gamma_2 \quad &= M_{22} - \frac{i}{2}\Gamma_{22} - \frac{q}{p}\left(M_{12} - \frac{i}{2}\Gamma_{12}\right).
\end{aligned} \tag{2.31}$$

The mass and width differences and means are defined as:

$$\begin{aligned}
\Delta M = M_1 - M_2 = \mathcal{R}e(\lambda_1 - \lambda_2), \qquad M = \frac{M_1 + M_2}{2}, \\
\Delta\Gamma = \Gamma_1 - \Gamma_2 = -2\mathcal{I}m(\lambda_1 - \lambda_2), \quad \Gamma = \frac{\Gamma_1 + \Gamma_2}{2},
\end{aligned} \tag{2.32}$$

and further dimensionless mixing parameters constructed:

$$x = \frac{\Delta M}{\Gamma}, \qquad\qquad y = \frac{\Delta\Gamma}{2\Gamma}. \tag{2.33}$$

The general solution to the Schrödinger equation 2.26 is given by

$$|\psi(t)\rangle = e^{-i\mathscr{H}t}|\psi(0)\rangle, \tag{2.34}$$

thus the previous diagonalisation of $\mathscr{H}$ allows us to simply state the time evolution of the mass eigenstates:

$$\begin{aligned}
|P_1(t)\rangle = e^{-i\lambda_1 t}|P_1(0)\rangle, \\
|P_2(t)\rangle = e^{-i\lambda_2 t}|P_2(0)\rangle.
\end{aligned} \tag{2.35}$$

The time evolution in the flavour basis can be obtained with a basis change

$$\mathbf{Q}^{-1}\begin{pmatrix} e^{-i\lambda_1 t} & 0 \\ 0 & e^{-i\lambda_2 t} \end{pmatrix}\mathbf{Q} = \begin{pmatrix} g_+(t) & \frac{q}{p}g_-(t) \\ \frac{p}{q}g_-(t) & g_+(t) \end{pmatrix}, \tag{2.36}$$

where the time evolution functions are defined as:

$$\begin{aligned}
g_+(t) = \frac{e^{-i\lambda_1 t} + e^{-i\lambda_2 t}}{2}, \\
g_-(t) = \frac{e^{-i\lambda_1 t} - e^{-i\lambda_2 t}}{2}.
\end{aligned} \tag{2.37}$$

Table 2.3: Overview of parameters important to mixing in the flavoured neutral systems, masses and width give the average over both mass eigenstates, except for K^0 width. Values from HFLAV [19] and PDG [9]. The uncertainties are given in brackets as multiples of the least significant digit.

Meson	**Mass in MeV/c^2**	**Lifetime in ps**	**x**	**y**
K^0	497.611 (13)	89.64 (4) 51160 (210)	0.946 (2)	0.997 (1)
D^0	1864.84 (5)	410.3 (10)	0.41 (5) %	0.62 (6)%
B^0	5279.66 (12)	1.519 (4)	0.769 (4)	*< 0.09*
B^0_s	5366.92 (10)	1.520 (5)	26.89(7)	0.064 (4)

From this, we can calculate the transition probabilities for pure flavour initial states at $t = 0$:

$$
\begin{aligned}
\left|\langle P^0|P^0(t)\rangle\right|^2 &= \left|\langle \overline{P}^0|\overline{P}^0(t)\rangle\right|^2 \\
&= |g_+(t)|^2 = \frac{1}{2}e^{-\Gamma t}\left(\cosh(y\Gamma t) + \cos(x\Gamma t)\right), \\
\left|\langle P^0|\overline{P}^0(t)\rangle\right|^2 &= \left|\frac{p}{q}\right|^2 |g_-(t)|^2 = \frac{1}{2}\left|\frac{p}{q}\right|^2 e^{-\Gamma t}\left(\cosh(y\Gamma t) - \cos(x\Gamma t)\right), \\
\left|\langle \overline{P}^0|P^0(t)\rangle\right|^2 &= \left|\frac{q}{p}\right|^2 |g_-(t)|^2 = \frac{1}{2}\left|\frac{q}{p}\right|^2 e^{-\Gamma t}\left(\cosh(y\Gamma t) - \cos(x\Gamma t)\right).
\end{aligned} \tag{2.38}
$$

It is worth pointing out some additional detail. Both the *CP* eigenstates and the flavour eigenstates are orthogonal bases. The same is, in general, not true for the mass eigenstates. In the CP-symmetric limit the mass eigenstates and CP eigenstates will coincide with $|P_1\rangle$ as being *CP* even and $|P_2\rangle$ *CP* odd, in this case $p = q = \frac{1}{\sqrt{2}}$.

In table 2.3 the relevant parameters are given and a visualisation of the transition probabilities is given in figure 2.5. It is clear that the same quantum-effect results in very different dynamics for K^0, D^0, B^0 and B^0_s. The Kaon system is dominated by the large differences in lifetimes, while the B^0_s system has the fasted changes in transition probabilities. Meanwhile, the D^0 system has the smallest mixing effects, mostly due to the small mass difference. Additionally, figure 2.6 presents the current status on the charm x-y plane, the first confirmation of a non-vanishing mass difference in the charm sector was published by the LHCb collaboration in a time-dependent analysis of $D^0 \to K^0_S\pi^+\pi^-$ [18].

In Appendix A we include a small discussion of a possible extension of the mixing theory to include the effect of material interactions.

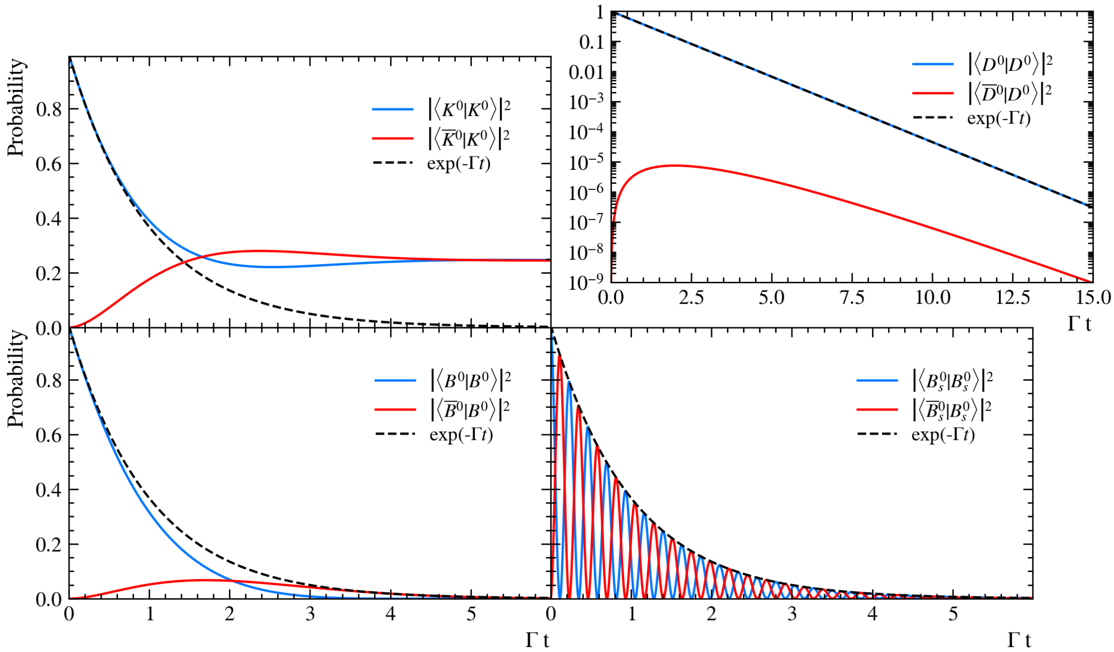

Figure 2.5: Transition probabilities of flavoured neutral mesons, K^0 (top left), D^0 (top right), B^0 (bottom left) and B_s^0 (bottom right). We use the dimensionless timescale Γt, *i.e.* the time in units of mean lifetime. Mixing in the charmed system is such a small effect that a log-scale for the probability and larger time scale had to be chosen to visualise the effect.

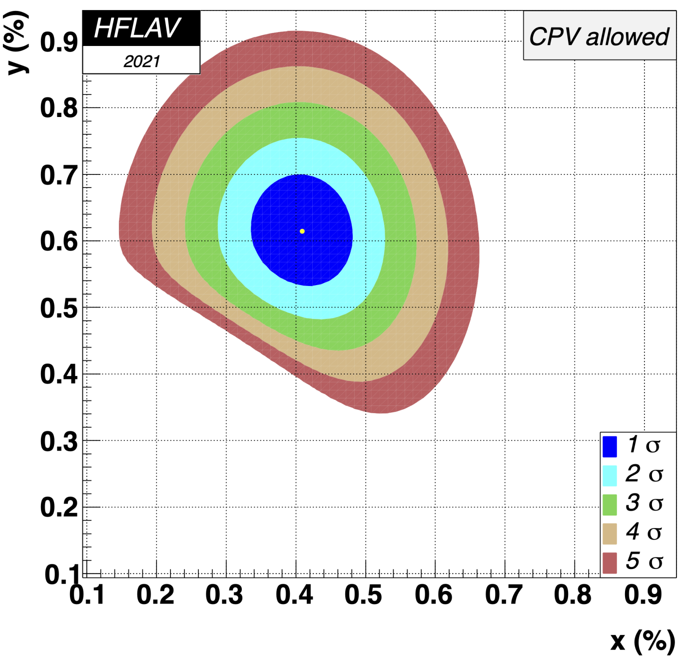

Figure 2.6: Global fit of the x and y mixing parameters for neutral charm mesons as of 21.12.2021 by HFLAV [19]. The no-mixing point $(x, y) = (0, 0)$ is excluded.

3 The LHC and the LHCb experiment

The LHCb collaboration has recorded the events analysed in this thesis during Run 2, *i.e.* the operating period from 2015 to 2018. The LHCb detector is one of the four main experiments at the Large Hadron Collider (LHC) operated by CERN.

3.1 The Large Hadron Collider

The CERN accelerator complex includes a series of machines accelerating particles to ever higher energy. Protons that end up in the LHC are sourced from hydrogen gas and progressively accelerated by the Linac2[1], the Proton Synchrotron Booster, the Proton Synchrotron and finally Super the Proton Synchrotron, which injects protons at energies of 450 GeV into the LHC. See figure 3.1 for an overview of the CERN accelerator complex. The LHC [20] is located in the 27 km tunnel that formerly housed the Large Electron-Positron Collider (LEP) and earth's most energetic particle accelerator. The LHC accelerates protons and maintains two proton beams travelling in opposing directions. These beams consist of bunches with a spacing of 25 ns, each consisting of $\sim 10^{11}$ protons. The bunches are held on path and shaped by superconducting magnets and accelerated in 16 radiofrequency cavities. The two opposing beams are brought to collision in four interaction points, where the experiments are located. The instantaneous luminosity, a measure for the potential number of collisions per second, peaked at $\sim 2 \cdot 10^{34} cm^{-1} s^{-1}$ during Run 2. High luminosity is needed to observe even rare decays. However, operating a detector at high luminosity can make it difficult to find and reconstruct interesting events. Therefore, LHCb has chosen to operate at a lower luminosity, thus having to resolve fewer events per bunch crossing.

3.2 The LHCb experiment

The LHCb experiment uses a right-handed cartesian coordinate system: The z-axis coincides with the beam-pipe so that the positive direction (downstream) points away from the interaction point towards the magnet. The y-axis goes up and the x-axis point away from the centre of the LHC. Also used is the pseudorapidity η, encoding the angle of a flight path with respect to the beam pipe,

[1] In Figure 3.1 the updated layout for 2022 is shown where Linac4 supersedes Linac2 in preparation for higher luminosity.

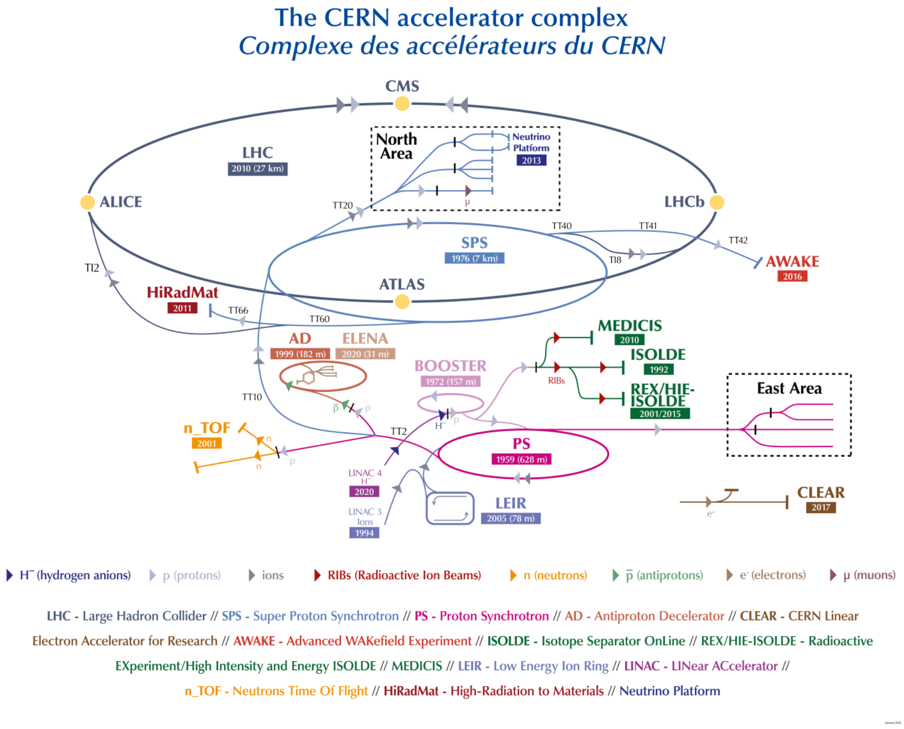

Figure 3.1: Illustration of the CERN accelerator complex including the various machines that lead up to the LHC, as well as different experiments [21].

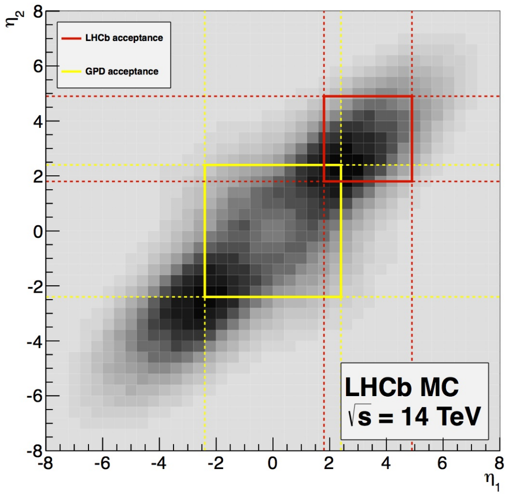

Figure 3.2: $b\bar{b}$ production rates as function of the pseudorapidities η_1 and η_2 plotted for collisions with centre-of-mass energies of 14 TeV. The acceptances of LHCb and a general purpose detector (GPD) are indicated. Figure from [24].

$$\eta \equiv -\ln\left[\tan\left(\frac{\theta}{2}\right)\right]. \tag{3.1}$$

The LHCb detector [22, 23] was explicitly designed to study heavy flavour physics. Its design goal is the search for direct evidence of physics beyond the Standard Model in rare decays of beauty and charm hadrons and precision measurements of *CP* violation.

At the design collision energy of 14 TeV, $b\bar{b}$ pair are produced with a cross section of ~ 500 µb, making the LHC the largest source of B mesons. The production of $b\bar{b}$ pairs happens mostly in gluon-gluon fusion, which results in large boosts along the beam pipe. As a result, the LHCb is a single-arm spectrometer with coverage in the forward direction. Although LHCb covers only about 4% of the solid angle ($1.9 < \eta < 4.9$), 24% of all $b\bar{b}$ pairs are inside its coverage. In figure 3.2 this is compared to the acceptance of a general purpose detector ($-2.4 < \eta < 2.4$), which covers about 90% of the solid angle and 41% of $b\bar{b}$ pairs. This forward design has advantages in the events that can be selected, such as b decay vertices with large displacements (due to the large boosts), but also engineering advantages, such as the ability to put dead material outside the acceptance, reducing sources of multiple scattering.

In figure 3.3 all the different subdetectors of the LHCb are shown. Charged tracks, and thus momenta, are measured with the Vertex Locator (VELO) and tracking stations up- and down-stream of the magnet, which has a bending power of 4 Tm. Photons and electrons are identified using the pad/preshower (SPD/PS) detectors and

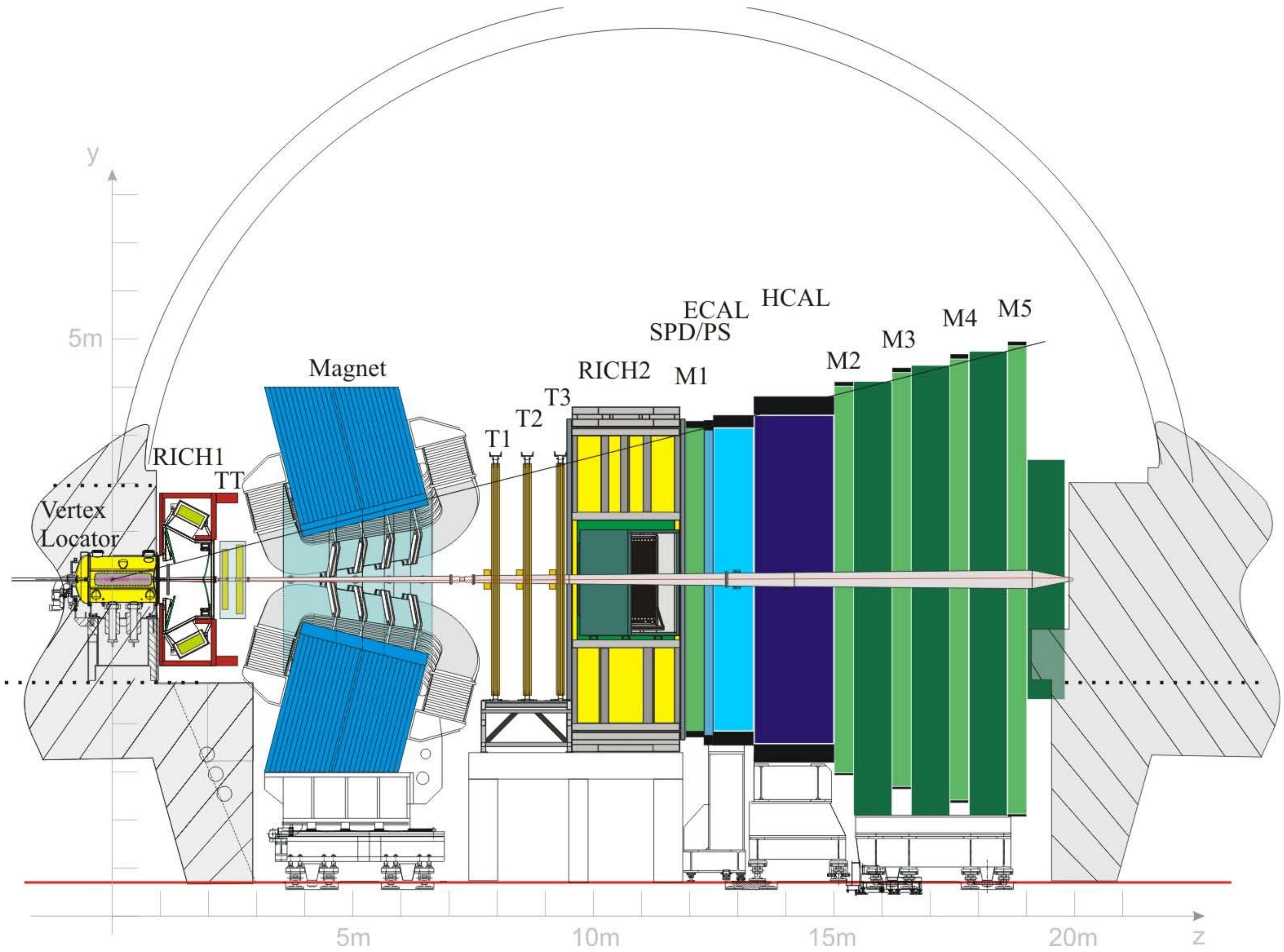

Figure 3.3: Side view of the LHCb detector that operated from 2010 to 2018. Figure from [25].

the electromagnetic calorimeter (ECAL). A hadronic calorimeter (HCAL) completes the calorimeter system. Two Ring imaging Cherenkov (RICH) detectors aid particle identification (PID). The muon stations are located downstream and dedicated to the tracking and identification of muons (M1-5).

3.2.1 Vertex Locator (VELO) and RF-foils

The Vertex Locator is the tracking detector closest to the interaction region and is utilised to identify the displaced secondary vertices of b and c-hadron decays. The detector consists of an array of modules, each made up of two silicon sensors, one measuring in R and one in ϕ, arranged along the beam pipe as shown in figure 3.4. The whole detector is composed of two halves that can be moved away from the beam. This is needed since the sensors are closer to the interaction point than the aperture required by LHC during the injection of new proton beams. Once a stable beam configuration has been reached by LHC, both halves can be moved into the measurement position, i.e. the VELO is closed. The half associated with positive x values is also referred to as the A-side and the other one as C-side[2]. Each half contains 21 sensor modules near and downstream of the interaction region. The sensors are arranged so that each particle originating from the interaction region and in the acceptance of the remaining tracking systems traverses a minimum of three sensor modules. For this purpose, there is also some overlap between both halves, as seen in the bottom left illustration of figure 3.4. Additional sensors are placed upstream of the interaction region as part of the pile-up system.

The sensor modules are contained within so-called RF-boxes that contain a secondary (detector) vacuum separated from the primary (beam) vacuum. The components of the RF-boxes facing the beam are called RF-foils. They are manufactured from a 300 µm AlMg3 foil and follow a complex shape to accommodate the needed overlap between both sides. The RF-foils are exposed to a pressure differential, which must not exceed 5 mbar to protect the foils against deformations. Monitoring systems are in place to ensure that this limit is respected during all operations. In addition to containing the detector vacuum, the RF-boxes and foils shield the sensors from RF pickup from the LHC beams and guide wakefields to prevent disturbance of the LHC beams. The VELO halves are movable in x and y and are centred on the interaction region (accounting for current beam conditions) when being closed at the beginning of each fill. The closing happens in several steps and it has been measured that the position can be reproduced better than 10 µm [26]. Furthermore, the symmetric closure of both halves is observed to have an accuracy of better than 4 µm. The first active silicon strips are at a radius of 8.2 mm to the LHC beam and the inner surface of the RF-foils at distances as close as 5.5 mm.

As detailed in figure 3.4, the sensors of both VELO halves overlap in the z-plane and are positioned with offset in the z-direction. The RF-foils must follow complex

[2]'A' for ascenseur or access, 'C' for cryo, a naming convention that applies beyond the VELO detector.

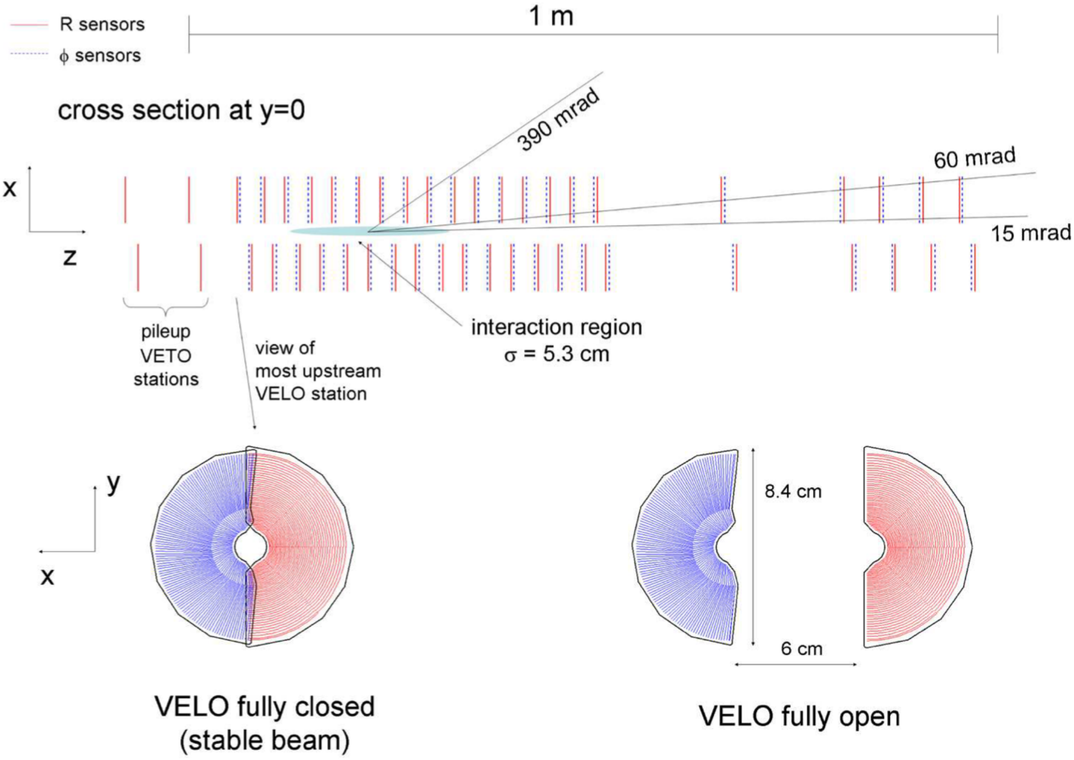

Figure 3.4: Illustration of the sensor configuration of the VELO detector. Top: Cross section in the (x,z) plane of the VELO sensors in the closed position. Bottom: A pair of sensor modules in the open and closed position when looking downstream. Figure from [22].

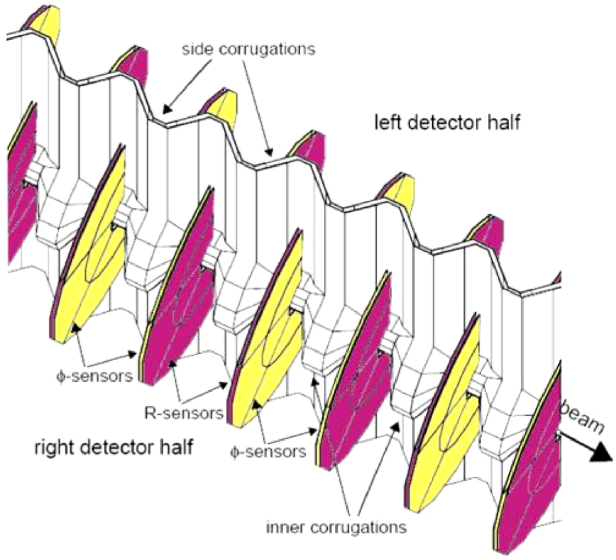

Figure 3.5: Section of the simulation models of the RF-foils (white) and the sensor modules in the fully closed VELO position. Figure taken from [22].

shapes to enable this and still contain both halves in their own RF-boxes. These complex shapes can be well understood from the simplified model used in LHCb detector simulation, depicted in figure 3.5. There we see how the RF-foils bend in and out to give space to the sensor of the opposite site. We also see the inner corrugations designed to shape the RF-fields inside the beam vacuum. The model used in simulations is simplified in so far, as it is composed of polygons. The real RF-foils are smooth and bend according to the designs depicted in figure 3.6. The curvature in the z-plane is composed of interlocking circles, as shown in the left image. The shape in the y-plane, with the RF-foils bending away from the beam between sensor positions, is shown on the right.

3.2.2 Tracking stations and magnet

For the momentum measurement of charged particles, a large room temperature dipole magnet creates a magnetic field in the acceptance of the LHCb detector, providing a bending power of 4.2 Tm. As shown in figure 3.3, tracking upstream of the magnet is provided by the VELO detector and Trigger Tracker (TT)[3]. Downstream tracking is provided by the T1, T2 and T3 tracking stations. The TT is a silicon microstrip detector, while the T1-3 stations are composed of two different subdetectors: The regions close to the beam pipe are covered by the silicon microstrip Inner Tracker (IT). The remaining area is covered by the straw tube Outer Tracker (OT), best seen in figure 3.7.

Each tracking station is made up of 4 different layers. They measure the variables

[3]Also known as Tracker Turicensis.

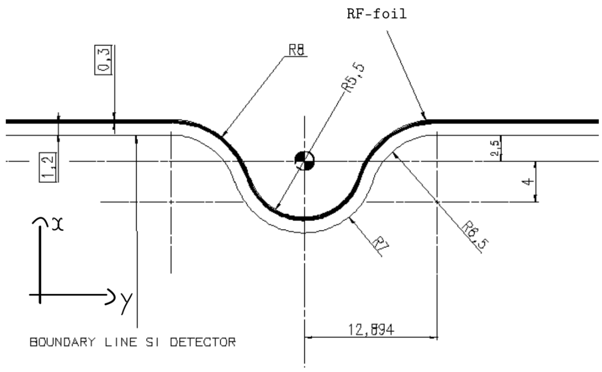

(a) z-plane

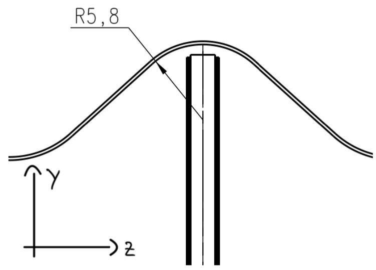

(b) y-plane

Figure 3.6: Technical drawings of the design RF-foil shape cross sections at the point of closest approach between foil and beam axis. Here only one of the two foils is shown. In b) the thick black vertical lines indicate the two silicon sensors making up one module.

x, u, v and x in that order. In the x layers, the strips/tubes are oriented vertically; in the u/v layers, they are rotated by $\pm 5\%$. This way, the y coordinate can be extrapolated and the vertical arrangement has mechanical advantages, especially needed for the straw tubes. However, this solution provides a worse resolution in the y direction than in the x direction. This is acceptable since charged particles are bent in the x direction and this variable is thus more important for good track reconstruction.

3.2.3 RICH detectors

The experiment uses two Ring Imaging Cherenkov detectors, RICH1 and RICH2, for the identification of charged hadrons with momenta in a range of 2 to 100 GeV/c. The two RICH detectors bookend the tracking stations, RICH1 between VELO and TT, RICH2 downstream of T3. Both detectors cover different momentum ranges. RICH1 covers momenta staring at 2 GeV/c up to 60 GeV/c. RICH1 uses C_4F_{10} gas as radiator. The downstream RICH2 covers momenta from 15 GeV/c to 100 GeV/c and utilises CF_4 gas. This focus on higher momentum particles is also reflected in the angular acceptance, as shown in figure 3.8, RICH2 acceptance only extends to 120 mrad. With two different radiators, the RICH systems are an important part of reliable particle identification over a large range of momenta.

Using the knowledge from the tracking system, the expected position of the Cherenkov radiation ring can be calculated. The radius of this ring is then compared to the different particle hypotheses - K, π and p. For each hypothesis, a likelihood is calculated. From these likelihoods, particle identification can be made directly via log-likelihood differences, or they can be used as an input for more sophisticated systems.

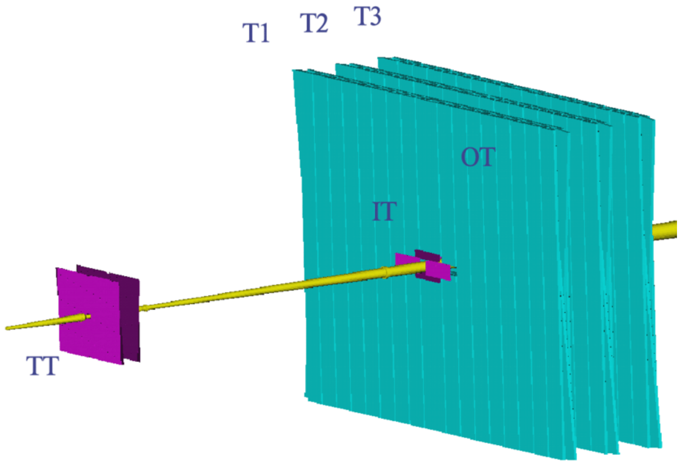

Figure 3.7: Illustration of the main tracking system. Illustration taken from [27].

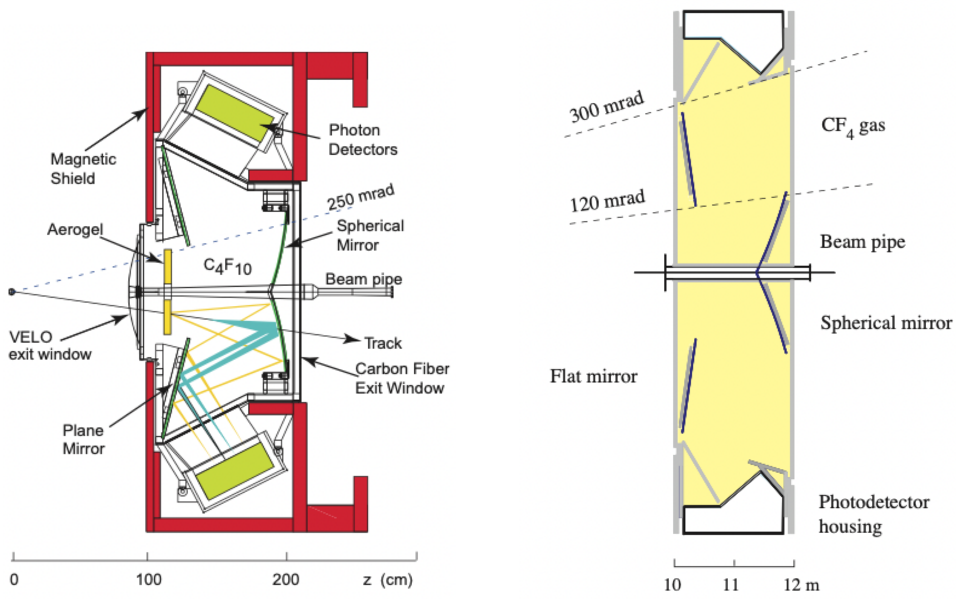

(a) RICH1 (b) RICH2

Figure 3.8: Cross section of both RICH detectors. Also marked are the angular acceptances. Note that RICH2 angular acceptance only extends to 120 mrad.

3.2.4 Electromagnetic and hadronic calorimeters

The calorimeter systems are not only used for the measurement of positions and energy of electrons, photons and hadrons but also contribute to their identification. The LHCb detector has four calorimeter systems: Scintillating Pad Detector (SPD), Preshower calorimeter (PS), electromagnetic calorimeter (ECAL) and hadronic calorimeter (HCAL). Both SPD and PS are constructed from planes of scintillator tiles, ECAL follows a shashlik-type construction, and HCAL has a sampling structure of passive iron layers and active scintillator tiles. In all cases, the light produced by particle interactions is carried away towards photomultiplier tubes (PMT) via wavelength-shifting fibres (WLS). The calorimeter systems cover the full acceptance of the tracking system.

The SPD and PS detectors are used to separate electrons and photons from hadrons. The detectors collect information on the longitudinal development of the induced showers. The SPD and PS are two identical planes of scintillating pads separated by a 15 mm thick layer of lead, equivalent to 2.5 radiation lengths (X_0). Since the hadronic interaction length is much larger than the radiation length X_0, photons and electrons are much more likely to induce a shower at this stage, thus helping to separate electrons and photons from hadrons. In addition, electrons deposit more energy in the SPD than photons; thus, SPD further enhances the PID capabilities.

The ECAL provides energy and position measurements of electrons and photons. With a thickness equivalent to 25 X_0, most electromagnetic showers can be fully contained. The sampling structure consists of 2 mm thick absorption layers of lead and 4 mm thick active layers of scintillator tiles interjected with WLS to carry the light towards PMTs.

The HCAL provides energy and position measurements of protons and neutrons as well as other long-lived hadrons. Since the containment of hadronic showers is not as crucial for the operation of LHCb, the HCAL thickness is only equivalent to 5.6 hadronic interaction lengths. The detector is composed of thin iron plates and scintillating tiles and the light yield is transported in WLS towards PMTs downstream of the HCAL. The HCAL was designed to be an important part of low-level trigger decisions.

3.2.5 Muon system

The LHCb muon system contributes to PID and trigger decisions for muons. The system contains five modules M1 to M5. M1 is located immediately upstream of the calorimeter system, and M2 to M5 downstream. It is depicted in figure 3.9. Muons almost always traverse the full detector because they lose less energy to bremsstrahlung than electrons. The muon stations are segmented into four regions (R1-4) based on occupancy. They are equipped with Multi Wire Proportional Chambers (MWPC) in all regions but the highest occupancy region of M1, which instead uses a Gas Electron Multiplier (GEM) detector. Multiple layers of MWPCs are used to achieve the required efficiency. Iron absorbers of 80 cm thickness are

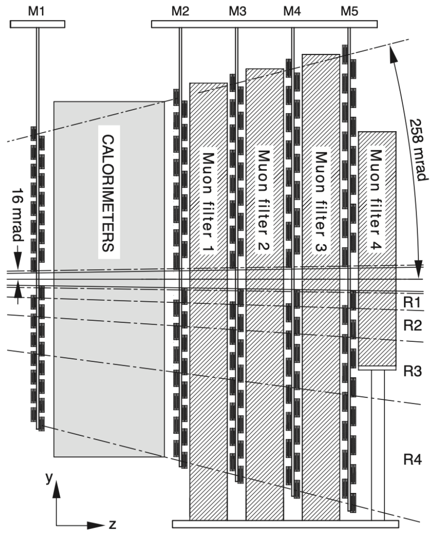

Figure 3.9: Side view of the muon system including the definitions of the regions R1-R4. Figure taken from [22].

stationed between the layers M2-M5 to act as muon filters. The total thickness of absorbers plus the calorimeter system is equivalent to 20 interaction lengths, so the minimum momentum for a muon to cross all five stations is about 6 GeV/c. Stations M1 to M3 are focused on resolution in the bending plane to contribute to the track reconstruction and thus momentum resolution. M4 and M5 are limited in spatial resolution and mainly identify highly penetrating muons.

3.2.6 LHCb trigger system

The LHCb trigger system decides which of the interactions happening at the LHC proton bunch crossing rate of 40 MHz should be recorded. The goal is to allow for data taking with minimal deadtime. An overview of the system is shown in figure 3.10. Since the maximum rate at which the entire LHCb detector can be read out is limited by the electronics to about 1 MHz, a fast system is needed to determine which events are kept.

The L0 hardware trigger is a system of field-programmable gate arrays with a fixed latency of 4 μs that make these low-level trigger decisions. There are separate L0 trigger lines for information from the SPD, PS, ECAL, HCAL and the muon stations. For example, L0 selects events with high transverse energy deposits in the calorimeters or straight-line tracks in all five muon stations but can also exclude events that exceed a maximum number of hits in the SPD. All these conditions are individually optimised based on the year (different collision rates) and the different trigger lines.

The High Level trigger (HLT) is composed of two stages: HLT1 and HLT2. HLT1 performs a partial reconstruction, including information from the tracking systems.

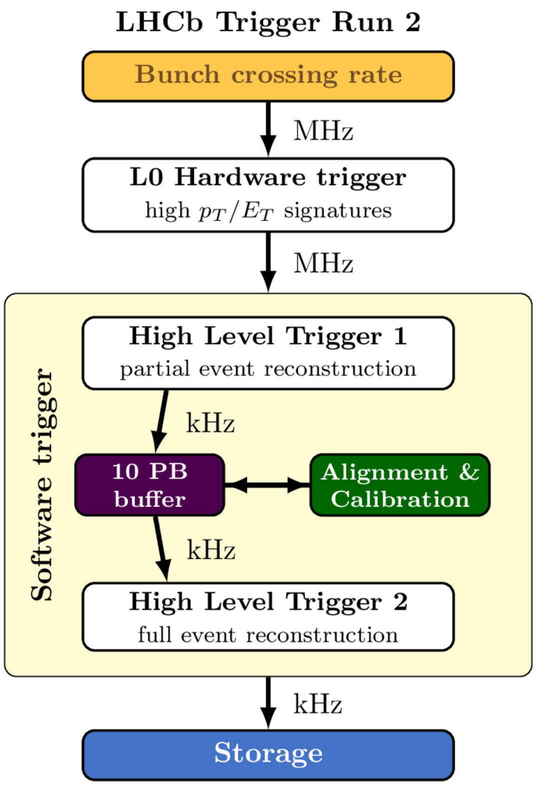

Figure 3.10: Overview of the Run 2 trigger system. Figure taken from [28].

This can identify tracks with high transverse momentum, *i.e.* $p_T > 500\,\mathrm{MeV}/c$. Tracks with large displacement from the primary vertex (PV) can also be identified using VELO information. This is a typical signature of b/c physics. Additional selections based on dimuon combinations or displaced muon tracks are also made. Events selected by HLT1 are buffered to a disk at a rate of 100 kHz. This buffering is done for two purposes, further processing can be performed in between LHC-fills and the LHCb detector can be aligned and calibrated for the individual runs[4] using this data.

After alignment and calibration, all events are fully reconstructed in HLT2. This means tracks of charged particles are formed, neutral particles are reconstructed and PID is performed. After the reconstruction, a large variety of triggers are applied. This result in an output rate of 12.5 kHz to be saved for offline analysis. The LHCb trigger system retains the information if a given signal candidate has activated a specific trigger line. In this analysis, the two relevant categories are:

- *Trigger On Signal* (`TOS`): The signal candidate produced a positive trigger decision.
- *Trigger Independent of Signal* (`TIS`): An unrelated candidate produced a positive trigger decision.

In addition, LHCb implemented Turbo streams in Run 2 [29]. These allow for offline analysis using information coming directly from HLT2. Turbo streams eliminate the need to save the full detector read-out for each signal candidate, thus reducing the needed bandwidth. This increased efficiency was crucial to the reach and diversity of the Run 2 charm programme.

[4]Data taking at the LHCb detector is divided into fills and runs. A fill is the period between the announcement of stable-beam conditions and the beam dump, typically around 12 hours. A run is a smaller segmentation, no longer than one hour in time. Not to be confused with Runs, as the time between long shutdowns of the LHC.

4 Analysis overview

A brief overview of the experimental techniques to measure the mixing parameters of the charm sector is given.

4.1 Previous measurements of charm mixing

There are several measurements of charm mixing parameters and *CP* violation by the LHCb collaboration. Most relevant to this thesis is the work utilising the WS-to-RS ratio technique on $D^0 \to K\pi$ decays, with the most recent measurement using events collected in Run 1 and the first half of Run 2 [30]. This high-precision measurement is performed using decays with a prompt flavour tag. The charm mixing parameters are determined in a time-dependent fit against the simplified mixing model. The time dependence of the WS rate arises due to the interference of the doubly Cabbibo-suppressed $D^0 \to K^+\pi^-$ decay and the Cabbibo-favoured $D^0 \to K^-\pi^+$ decay and the D^0-$\overline{D}^0$ mixing. Using the limit of small mixing parameters $|x|, |y| \ll 1$ and no *CP* violation we can expand the analytical equations for charm mixing (eq. 2.38) in decay time Γt and, dropping all but the leading terms in R_D, derive a time-dependent formula for the ratio [31–34]:

$$R(t) \approx R_D + \sqrt{R_D} y' \Gamma t + \frac{x'^2 + y'^2}{4} (\Gamma t)^2. \tag{4.1}$$

Here R_D is the ratio of suppressed-to-favoured decay rates, the parameters (x', y') are linear combinations of the dimensionless mixing parameters (x, y) based on the strong phase difference δ:

$$\begin{aligned} &\frac{\mathcal{A}(D^0 \to K^+\pi^-)}{\mathcal{A}(\overline{D}^0 \to K^+\pi^-)} = \sqrt{R_D} e^{-i\delta}, \\ &x' = x\cos\delta + y\sin\delta, \\ &y' = y\cos\delta - x\sin\delta. \end{aligned} \tag{4.2}$$

In these high precision measurements additional degrees of freedom are introduced to allow for the measurement of *CP* violation. An observed WS-to-RS ratio is then determined in several decay time bins, where the decay time of a particle is based on the relativistic calculation:

$$t_D = \frac{m_{D^0} \vec{L} \cdot \vec{p}(D^0)}{p^2(D^0)}, \tag{4.3}$$

where $\vec{L}$ is the vector connecting the D^0 production vertex with its decay vertex.

In each of these decay time bins, the ratio is determined with a fit to the reconstructed D^* mass to both the RS and WS channels. The mixing parameters are then determined in a χ^2 fit, which accounts for nuisance parameters such as detection efficiencies, background contamination and other systematic effects.

4.2 Adaptation to charm in material

The first large difference in our analysis is the sample choice, while previous analyses only consider D^0 mesons that decay inside the primary vacuum, we do the opposite and select D^0 meson with a flight path intersecting the RF-foils. For this selection, a model of the RF-foils is created, detailed in chapter 5.

In Appendix A we include a small discussion of the possible signature of material interaction in neutral charm mixing on this measurement.

We also include D^0 decays with a semileptonic tag in the analysis to extend the statistical viability of the analysis. For the same reason, we do not separate the samples by year or magnet polarity and the measurement is flavour averaged. This allows systematic effects, such as charge-dependent detection efficiencies to cancel in the measurement. The selection of both the prompt and semileptonic tagged sample is explained in chapter 6, where we also explain the selection based on the flight path and the RF-foils.

We also differ in the determination of the WS-to-RS ratio (chapter 7), for the prompt sample we fit the signal shape in the mass difference $\Delta m = m(D^*) - m(D^0)$, which suppresses some peaking background better than a fit to the D^* mass alone. For the semileptonic sample, a fit to the reconstructed D^0 mass is performed.

We investigate the size and influence of peaking backgrounds to both channels in chapter 8 and the presence of secondary decays in the prompt sample in chapter 9.

Finally, in chapter 10 we perform a fit to the mixing parameters ($R_D,\ x',\ y'$) and perform a time-integrated hypothesis-test of mixing effects beyond mixing in vacuum for both kinds of tags.

As part of the analysis, a blinding is implemented so that no undue influence is exerted on the results.

5 Modelling the RF-foils

The RF-foils are a part of the VELO detector of the LHCb experiment. A detailed description of the detector and the function of the RF-foils as part of VELO is given in section 3.2.1. Detailed models of the RF-foils are needed to perform this analysis, as outlined in chapter 4.

5.1 SMOG-models of the RF-foils

As part of a search for dark photons [35] high resolution models of the RF-foils were developed [36]. These are derived by fitting a parametric model of the RF-foils against data taken during LHCb operation in fixed target mode. Specifically, the System for Measuring Overlap with Gas (SMOG) was used to produce collisions between high-energy protons and a helium gas injected into the primary LHC vacuum inside the VELO detector. Particles produced in this fixed target mode then decay inside the RF-foils due to material interactions, thus allowing for a position measurement of both RF-foils. In the following, we refer to these models as the SMOG-models. In figure 5.1 we can see the strong improvement of these SMOG-models compared to the models used for LHCb detector simulations.

5.2 Improving the SMOG-models

For this thesis, we build improved models of the RF-foils based on the SMOG-models, which we call the charm-models. Calculations relevant to the event selection are

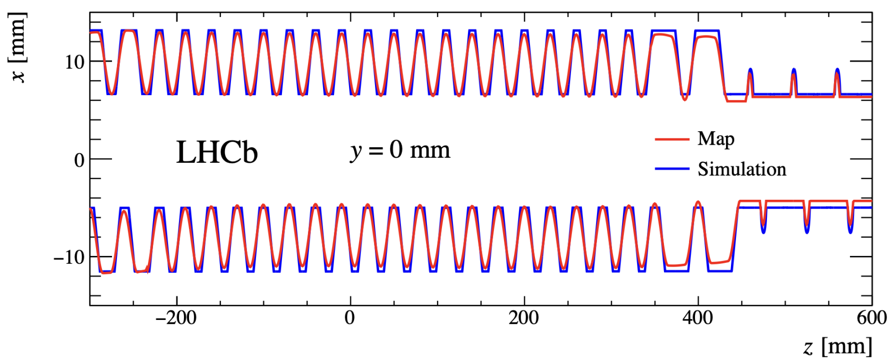

Figure 5.1: Cross section of the y-plane of the VELO detector. The SMOG-models are shown in red, and the models used in the LHCb simulation are in blue. Figure taken from [36].

performed based on these charm-models of the RF-foils.

5.2.1 Data set

We use an extensive data set of $D^0 \to K^-\pi^+$ decay selected with the prompt Turbo lines, also described in chapter 6. We do not require any selection criteria beyond the inclusion in the Turbo line. We use the spatial location of the $D^0 \to K^-\pi^+$ decay vertex from these candidates. To extract the position of the RF-foils from this data set, we use the same methodology as used in creating the SMOG-model. Decays can happen at any spatial location, but the interaction with the material of the RF-foils increase the decay probability. Therefore the local density of decay vertices increases at the position of the RF-foils. Several million decays are included in the vicinity of the RF-foils. This data set of charm decays was chosen due to two advantages. First, it is a very large, high-quality data set readily available and trusted due to its many applications in different studies. Secondly, we use similar decays in the analysis and thus, this data set enables us to have a high resolution in the charm-models exactly where it is needed for our analysis. To prepare this data set for use in this analysis, we adjust the position of the decay vertices to account for the shifting position of the RF-foils in different fillings of the LHC. In this chapter and this chapter only, we mean this data set when referring to the charm data set or similar.

5.2.2 Tests of the SMOG-models of the RF-foils

To motivate the creation of the charm-models of the RF-foils, we compare the SMOG-models to the data set of charm decays. An example of these tests can be seen in figure 5.2. Here we show a cross section of the VELO detector in the z-plane at z=80 mm. In red, the positions of the SMOG-models are indicated and in green/blue, a histogram of the decay vertex density in this plane. In this part of the VELO detector, a sensor is located in the left half of the figure. The figure shows how the local peak in the density of charm decays lines out the shape of the RF-foils. However, we see that there are also differences between the red line (SMOG-model) and the position indicated by charm data. To make this difference more visible, we also include a metric for these differences in the side panels. The mean x-position of the charm decay vertices within the red band is subtracted from the SMOG-model x-position, binned in y. This systematic difference between the SMOG-models and the charm data set has been observed over the entire VELO detector. While these deviations are small in absolute terms, they greatly impact the decay selection for this analysis. Thus we do not use the SMOG-models for this analysis but create the charm-models of the RF-foils based on the charm data set.

5.2.3 The charm-models of the RF-foils

The charm-models of the RF-foils are built on the basis of the SMOG-models. The charm-models are corrected versions of the SMOG-models, where the corrections are

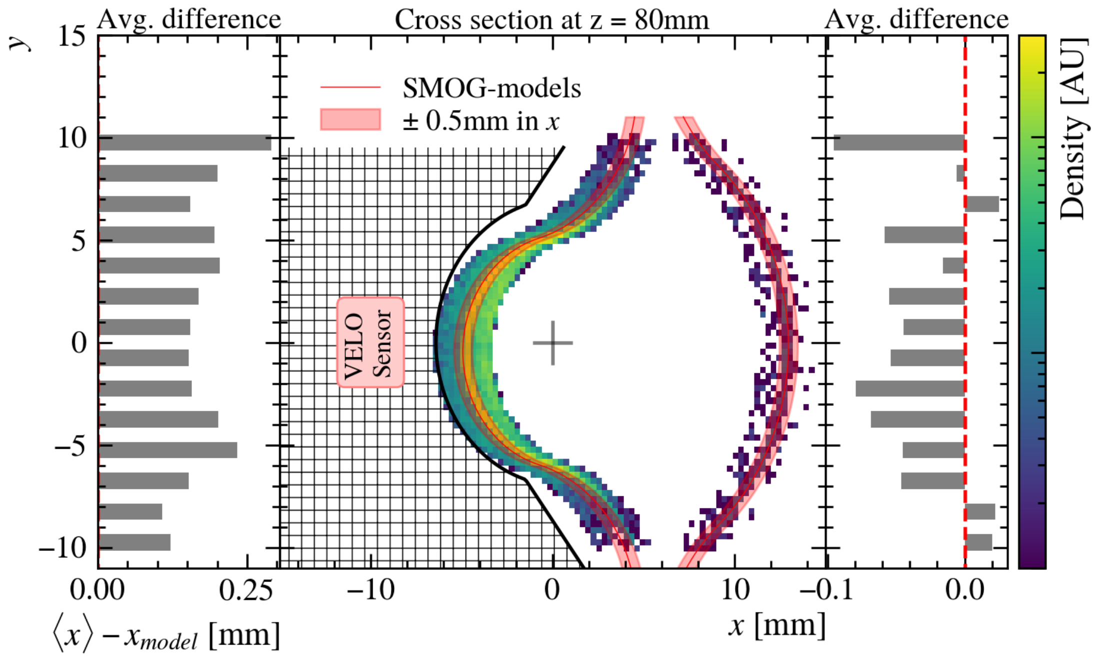

Figure 5.2: Illustration of the differences between the SMOG-models and the position indicated by the charm data set. The centre panel shows a cross section of the spatial distribution of $D^0 \to K^-\pi^+$ candidate decay vertices at $z = 80\,\text{mm}$ (yellow - high density, blue - low density). The data set has been reduced to only include decays near the RF-foils position. The position of the SMOG-models is indicated in red. The two side panels indicate the differences between SMOG-models and charm data set by comparing the mean of the x-position of the decay vertices in the red band to the SMOG-models position. The nearby VELO sensor is located in the hatched area.

based on the charm data set. To understand how these corrections are calculated, we first need to explain how the SMOG-models are parameterised. For each (y, z) coordinate, the SMOG-models assign x-values to describe the respective RF-foils positions. The charm-models take the assigned x-values from the SMOG-models and add a correction term. We build the charm-models for the spatial region defined by $-10\,\mathrm{mm} < y < 10\,\mathrm{mm}$ and $-50\,\mathrm{mm} < z < 300\,\mathrm{mm}$. This region contains the segments of the RF-foils where the majority of D^0 mesons are expected to intersect the RF-foils.

The correction terms used in the charm-models are the differences between the positions given by the SMOG-models and those indicated by the charm data set. This difference is similar to those calculated and shown in the side panels of figure 5.2. In the following, we explain the details of how these calculations are performed. There are two major difficulties with this approach. We have a large amount of background in the charm data set, where the background is genuine $D^0 \to K^-\pi^+$ decays that happen without any relation to the RF-foils. The signal is $D^0 \to K^-\pi^+$ candidates, whose decay was prompted by interactions with the RF-foils material and that decay inside the RF-foils. The background follows an exponential distribution with a higher density closer to the interaction points, which in turn is correlated to the x-coordinates. This can also be observed in figure 5.2. This background shape results in a bias towards smaller absolute x-values if we were to simply calculate the mean x-coordinate of the charm data set within a bin along the x-axis. This bias becomes larger with bigger bin sizes, where the bin size is the width of the red band in figure 5.2. However, we cannot reduce the width arbitrarily, they are centred around the positions of the SMOG-models but must also contain the position indicated by the charm data set. This can be solved with an iterative approach. In a first iteration, a large bin width along the x-axis is chosen and biased corrections are calculated. In the next iteration, the bins are centred on the SMOG-model position plus the biased corrections calculated in the previous iteration. In this iteration, the bin width can be reduced, resulting in a smaller bias. A second problem is the choice of binning along the y- and z-axis to accommodate large variations in the density of the charm data set. The density is very high in locations near a VELO sensor, meaning small bins can and should be used. In regions between two VELO sensors, the RF-foils are further away from the beam pipe. Thus the samples are less dense and larger bin sizes are needed. These variations in density are illustrated well in figure 5.2, where the C-side (left) is near a sensor and the A-side is between sensors on their respective halves. The machine-learning tool XGBoost [37] is used to calculate the differences. XGBoost belongs to the class of gradient boosted decision tree algorithms, which have proven to be very powerful and reliable machine learning tools. Here it is used to circumvent the restrictions of a fixed binning in the y and z coordinates.

The charm data set is subdivided into training and validation data sets. The training data set contains 6.6 million decay vertices within 2 mm of the SMOG-models RF-foils positions. We use the y-, z-coordinates of these vertices as the input (predictive) variables of the XGBoost algorithm. The difference between the

x-coordinate of the vertices and the x-positions of the SMOG-models are used as the target (output) variables. In effect, the XGBoost algorithm in this setup performs a non-parametric regression towards the mean. Thus the real positions of the RF-foils, without the need to choose the y-, z-binning.

A total of four iterations are performed, each iteration starting with smaller x bin sizes, starting at 2 mm and ending at 0.8 mm. In figure 5.3 we show the same cross section of the VELO detector as in figure 5.2, but now with the charm-models included. In this updated figure, we see that the charm-models (in red) track the RF-foils positions, as indicated by the charm data set, better than the SMOG-models (in black). We also see that the differences, now calculated with respect to the charm-models and shown in the side panels, are smaller than they are for the SMOG-models. The same improvement is observed in the full domain of the charm-models. An overview is given in figure 5.4, here we show the same difference as in the side-panels of figure 5.3, but as a function of both y and z and calculated with the validation portion of the charm data sample. While there are some repeating patterns, for example the A-side RF-foil model shows repeating negative differences at around $y = \pm 6$, these patterns are rather weak. The low z regions also show large differences. However, these mostly indicate the low density of the charm data set in these regions. Since we used the validation charm data set to calculate the differences, *i.e.* a data set independent of the data set used to create the charm-model, the pattern of random noise we observe is a sign of a good fit.

5.2.4 Software implementation of the charm-models

To use the charm-models in our analysis, we have to implement them in software. The positions we have determined from the charm data set are the centre-of-mass position of the RF-foils, but we are interested in the RF-foils as three-dimensional objects with volumes. As a first step, we apply smoothing to the output of the XGBoost algorithm, which is non-continuous due to its tree nature. These discontinuities are purely computational artefacts and do not reflect physical reality. Next, we apply a Gaussian filter on the order of 200 μm. This incurs a minimal loss of information about the shapes of the RF-foils. Finally, we add the smoothed XGBoost outputs to the SMOG-models to obtain the centre-of-mass charm-models of the RF-foils.

To transform these two-dimensional surfaces into three-dimensional volumes, meshgrids of the surfaces are created, with step sizes of 10 μm in the y-coordinate and 50 μm in the z-coordinate. This choice is made as a trade-off between resolution of the final charm-models and the computational requirements while working with the charm-models. Uncertainties arising from the meshgrid resolution are insignificant compared to the uncertainty of the charm-models themselves. We then calculate the normal vectors on the centre-of-mass surface and shift the centre-of-mass meshgrid points ± 150 μm inwards and outwards to create the surfaces of 300 μm thick models of the RF-foils, where 300 μm is the design parameter for the RF-foils thickness.

As part of this thesis, Python software is written that is capable of performing several geometric calculations involving the VELO detector. This software contains

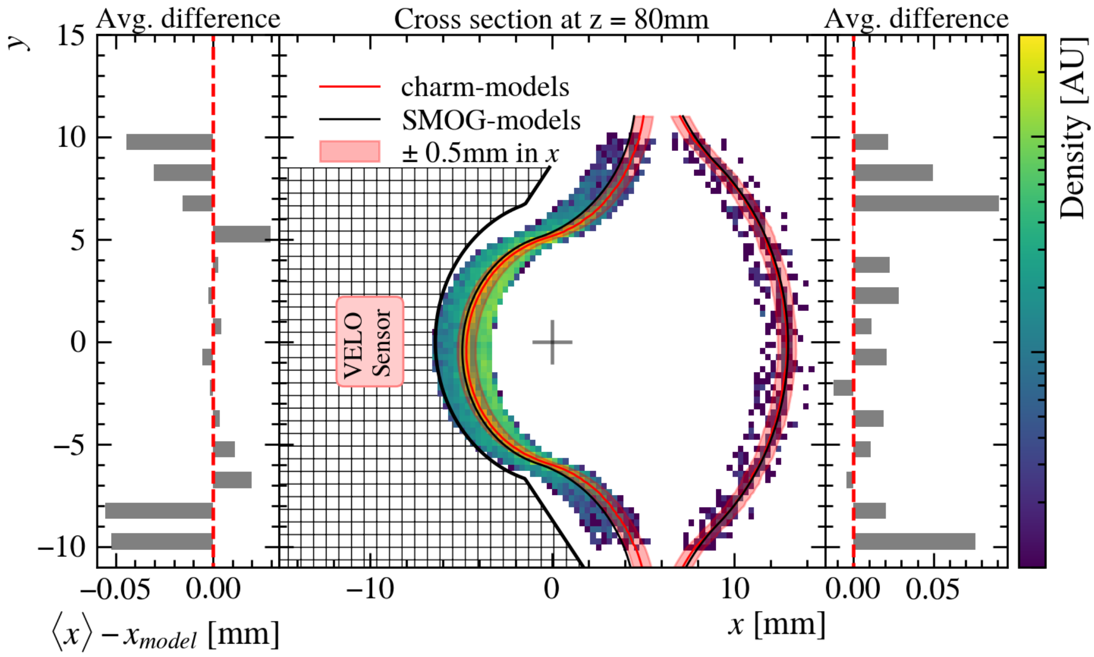

Figure 5.3: Illustration of the differences between the charm-models and the position indicated by the charm data set. The centre panel shows a cross section of the spatial distribution of $D^0 \to K^- \pi^+$ candidate decay vertices at $z = 80\,\mathrm{mm}$ (yellow - high density, blue - low density). The data set has been reduced to only include decays near the RF-foils position. Also indicated are the position of the SMOG-models (black) and charm-models (red) of the RF-foils. The two side panels indicate the difference between charm-models and charm data set by comparing the mean of the x-position of the decay vertices in the red band to the charm-models position. The nearby VELO sensor is located in the hatched area.

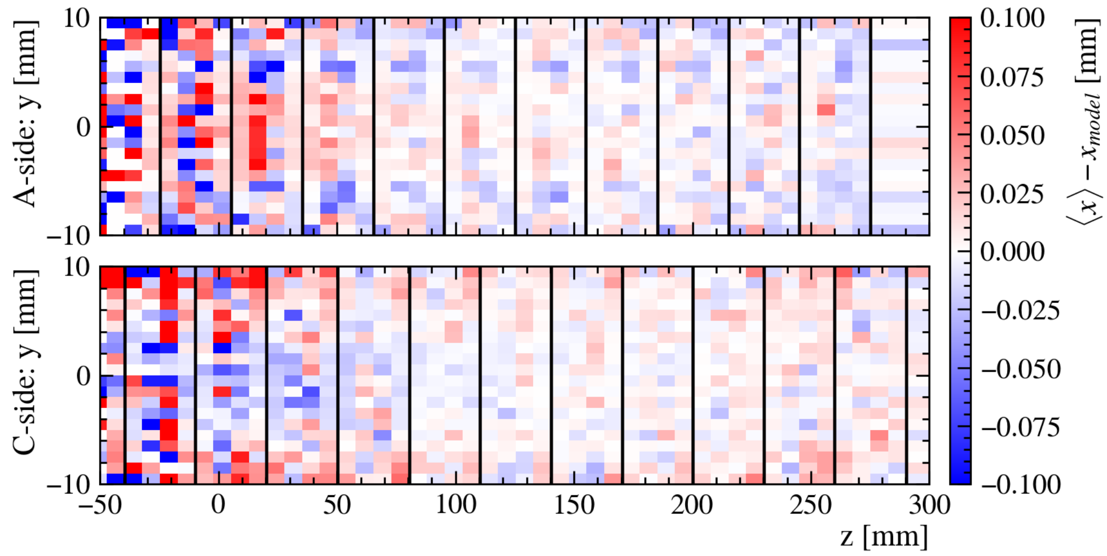

Figure 5.4: Binned view of the difference along the x-axis in the $y - z$ plane. Black lines indicate the positions of the VELO sensors in the respective halves. Differences are calculated from the validation sample.

the geometric and spatial information of the RF-foils from the charm-models as well as the VELO sensor. The sensor positions and geometry are taken from the work described in Ref. [36]. The relevant calculations performed using this software are the minimum distance between a vertex and RF-foils or the sensors in euclidean and uncertainty space. The calculations in uncertainty space are based on the Mahalanobis distance. It returns the minimum distance in terms of standard deviations based on the vertex uncertainty, including the full covariance matrix. The software also includes checking if a particle's flight path crosses a VELO sensor or the RF-foils. If one RF-foil is crossed, it is possible to calculate how many millimetres of the flight path is contained in the RF-foils material. It also returns more detailed information about the number of intersects, their position in the flight path and the contribution to the total amount of material in flight path.

5.3 Tests of the charm-models of the RF-foils

To test the charm-models and their software implementation, we perform additional tests. For each $D^0 \to K^-\pi^+$ decay vertex in the charm data set, also used in the creation of the charm-models, we calculate the distance to the closest RF-foil surface. By using a signed distance, we get the position of the reconstructed decay vertices along the surface normals of the charm-models. If we integrate this distance over a small surface area, we expect to see the following signed distance distribution: The position of the foil should be represented by a uniform distribution convoluted with a normal distribution. To first order, we expect the likelihood of interaction within the foil material to be constant, thus the uniform distribution. This uniform distribution should be washed out by a normal distribution describing the limited detector resolution along the surface normal. The background is described by an exponential distribution, which is derived from the exponential decay of genuine D^0 particles, as well as a normal distribution used to catch asymmetries. To reduce the background from decays not induced by interactions with the material, a requirement on the mass of both D^0 and $D^*(2010)^+$ is imposed, such that the nominal mass peaks are excluded at $\pm 20\,\mathrm{MeV}/c^2$.

We perform a fit against these distributions over several y-z-bins. We cover the area $y \in [-8, 8]\,\mathrm{mm}$ and $z \in [0, 250]\,\mathrm{mm}$ in the LHCb coordinate system. In the z-dimension, four bins of equal size are created between two neighbouring sensors. In the y-dimension, we create twenty bins, whose sizes vary with the shape of the RF-foil, *i.e.* smaller bins for larger gradients. This binning leads to sizeable averaging and thus cannot resolve small-scale structure in the charm data. However, it is a good test of the charm-models and their software implementation, with respect to the charm data set they are supposed to represent.

In figure 5.5 we see the fitted position of the individual bins. Here a position value of zero (white) means that the charm-models centre-of-mass position aligns with the centre-of-mass indicated by the charm data set. While there is some structure in these plots, we can see that the charm-models are reliable up to deviations of $50\,\mu\mathrm{m}$, a fraction of the width of the RF-foils.

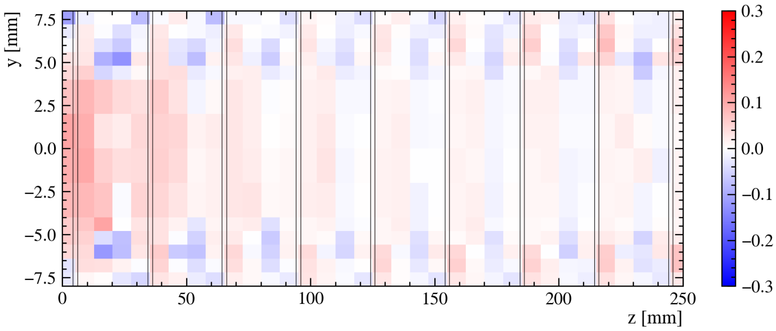

(a) Position evaluation A-side

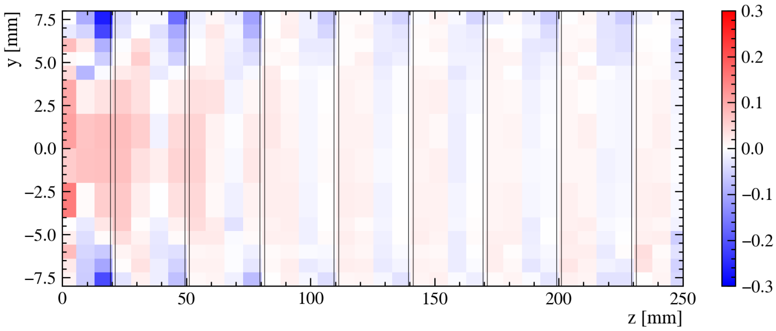

(b) Position evaluation C-side

Figure 5.5: Results of the tests of the charm-models of the RF-foils. Shown are the fitted foil position of the RF-foils, as integrated over the bins. The vertical black lines indicate the positions of sensor modules.

6 Data samples and event selection

This chapter explains the selection of $D^0 \to K^-\pi^+$ and $D^0 \to K^+\pi^-$ candidates with either prompt or semileptonic flavour tags. The measurement in this thesis is based on samples of proton-proton collision data collected by LHCb during 2016-2018 (Run 2) at $\sqrt{s} = 13\,\text{TeV}$ corresponding to an integrated luminosity of $5.4\,\text{fb}^{-1}$.

6.1 Prompt tagged sample

The selection of prompt tagged RS (WS) events is based on the dedicated Turbo lines [38]
`Hlt2CharmHadDstp2D0Pip_D02KmPipTurbo` (`_D02KpPimTurbo`). A summary of the implied selection criteria can be found in Tab. 6.1.

The candidates resulting from the HLT2 selection require further offline selection. They are first refitted offline using the `DecayTreeFitter` (`DTF`) [39] algorithm with a primary-vertex and/or a D^0 mass constraint. A successful offline fit, *i.e.* $\chi^2/\text{ndf} > 0$, is a condition for inclusion in the sample. In the following, all kinematic variables refer to those calculated by the `DecayTreeFitter`. This does not include variables related to the vertices themselves, such as impact parameter related variables or vertex positions. We also require vertices to be fitted successfully with a $\chi^2 > 0$ requirement and by setting upper limits on the uncertainty of the vertex position.

For the further offline selection (also Tab 6.1) we have several trigger requirements:

- (`L0Hadron_TOS` on D^0 OR `L0Global_TIS` on D^{*+}) AND
- (`Hlt1TrackMVA_TOS` OR `Hlt1TwoTrackMVA_TOS` on D^0).

To suppress misidentification backgrounds, we require the decay products of the D^0 to meet PID requirements. The PID requirements on the D^0 decay products are specifically designed to suppress candidates, where the particle identification on both D^0 decay products is swapped between pion and kaon, the so-called doubly misidentified background. We enforce the requirement `ProbNNpi`$(K)/$`ProbNNpi`$(\pi) < 0.2$ and `ProbNNk`$(\pi)/$`ProbNNk`$(K) < 0.8$. Other misidentification backgrounds can be excluded with kinematic requirements.

We also pose requirements on the direction angle of the D^0. The direction angle is the angle between the momentum of the particle ($\vec{p}$) and the displacement vector ($\vec{d}$), $\measuredangle(\vec{p}, \vec{d})$. For a fully reconstructed particle, this angle should vanish. Thus the HLT2 selection requires the angle to be smaller than 17.3 mrad.

The particle identification on the soft pion is performed using a simple `ProbNNpi` requirement. In addition, we require that the invariant $K\pi$ mass is within 24 MeV/c^2-

Table 6.1: Summary of the selection criteria for RS and WS prompt decays.

Quantity	HLT2	Offline	Units
$p_T(K, \pi)$	> 800	-	MeV/c
p(K, π)	> 5	-	GeV/c
IP$\chi^2(K, \pi)$	> 4	-	-
PIDK (K)	> 5	-	-
PIDK (π)	< 0	-	-
`ProbNNpi` (π_s)	-	> 0.5	-
`ProbNNpi` (K) / `ProbNNpi` (π)	-	< 0.2	-
`ProbNNk` (π) / `ProbNNk` (K)	-	< 0.8	-
$p_T(D^0)$	> 2	-	GeV/c
p(D^0)	> 5	-	GeV/c
p_T of at least one D^0 decay product	>1.5	-	GeV/c
K, π distance of closest approach	< 0.1	-	mm
D^0 direction angle	< 17.3	-	mrad
logIP$\chi^2(D^0)$ + 0.65 logIP$\chi^2(\pi_s)$	-	< 3.5	-
D^0 flight distance χ^2	> 25	-	-
D^0 vertex-fit χ^2/ndf	-	[0,10]	-
D^{*+} vertex-fit χ^2/ndf	-	[0,25]	-
PV vertex-fit χ^2/ndf	-	[0, 10]	-
m(K π)	$[1.715, 2.015]$	$[1.84084, 1.88884]$	GeV/c^2
|m(K K, π π) - m$_{D^0}$|	-	> 40	MeV/c^2
$p_T(\pi_S)$	> 100	> 500	MeV/c
π_s: Track based ghost probability	-	< 0.20	-
Vertex-fit and `DTF` convergence	-	True	-
m(K π π_s) - m(K π)	< 160	-	MeV/c^2
Multiple Candidate selection	-	True	-
WS candidate matched RS candidates	-	False	-
`DTF`(_PV,_D0M) χ^2/ndf	-	$[0, 6]$	-

equivalent to three standard deviations - of the nominal D^0 mass. We also exclude candidates with K^+K^- and $\pi^+\pi^-$ masses, *i.e.* the reconstructed D^0 mass after we change one of the PID hypothesis, closer than $40\,\mathrm{MeV}/c^2$- equivalent to five standard deviations - to the PDG D^0 mass.

To remove D^0 candidates that were not produced in the primary pp interaction, also called secondary D^0, we apply the following requirement to the impact parameter IPχ^2 of the D^0 and soft pion candidates:

$$\log(\mathrm{IP}\chi^2(D^0)) + 0.65 \cdot \log(\mathrm{IP}\chi^2(\pi_S)) < 3.5. \tag{6.1}$$

A detailed explanation of this requirement is given in the dedicated chapter 9.

Ghost soft pions are built from correctly attributed clusters in the VELO and TT with incorrectly attributed tracks in the downstream tracking system. This leads to a wrong reconstructed momentum of the soft pion and can also lead to a misidentified charge and, thus, a wrongly tagged candidate. Since the incorrectly matched downstream pion still has to have low momentum to be included in the sample, these events can lead to a peaking contribution in Δm. These events can be excluded by requiring the track-based ghost probability of the soft pion candidate to be less than 0.20. The value was chosen based on signal significance in the WS sample.

The sample also contains a small subset of multiple candidates, a phenomenon explained in [40]. From inspection, it is clear that the multiplicity results from the same D^0 candidates with a different association of soft pions. We resolve this multiplicity by choosing the candidate with the lowest D^{*+} vertex χ^2. As can be observed in figure 6.1, where the Δm distribution of removed candidates is shown, the so removed events candidates do not peak in the signal region.

As a final step, we remove WS candidates that share a D^0 candidate with a RS event candidate. The main source of such events is the accidental association of a second soft pion with an opposite charge with the same D^0 candidate. Since RS events are much more likely to be real, we sort the event into the RS sample. The PID requirements filter out all these events, so the selection has no effect. This is not true in general and, in this case, most likely happens due to the small sample size.

6.2 Semileptonic tagged sample

The selection of semileptonic tagged RS and WS events is based on the Turbo lines [38] `Hlt2SLB_B2D0Mu_{KmPip, KpPim}` and is largely inherited from a previous semileptonic $D^0 \to h^-h^+$ analysis [41]. A summary of the implied selection criteria are found in table 6.2. We select the `L0` trigger `L0MuonDecsion_TOS` on the muon and the HLT1 trigger combination:

- (`Hlt1TrackMuonDecision_TOS` OR `HLT1TrackMuonMVADecision_TOS` on μ) AND

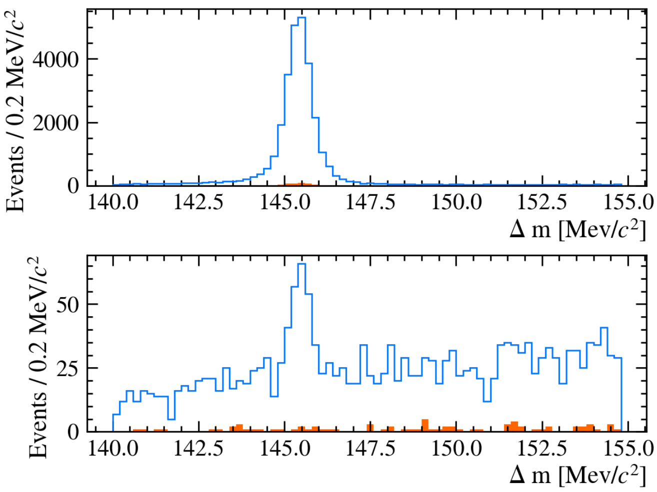

Figure 6.1: Δm distribution of events removed due to the multiple candidate selection (orange) and the full sample after offline selection (blue). On top is the RS sample and the WS sample is on the bottom.

- (`Hlt1TrackMuonDecision_TOS` OR `Hlt1TwoTrackMuonDecision_TOS` on B).

Events that pass the trigger level selections are further filtered in the offline selection. We first ensure a good reconstruction by requiring that the `DecayTreeFitter` [39] reconstructing the B decay converges and has a χ^2/ndf of less than 9.5. An additional check that the reconstructed process is physically useful is to require that the B and D^0 decay vertices are reconstructed in the correct order with $vtx_z(D^0) - vtx_z(B) > 0$. We also require a veto on events that are consistent with originating from a J/ψ or $\psi(2S)$ decay. If the D^0 decay product with opposite charge to the muon tag carries the `isMuon` PID-flag, we calculate the invariant $m(\mu\mu)$ mass by replacing the mass hypothesis of the D^0 respective decay product. If this mass is consistent with one of the charmonium masses, the candidate is removed from the analysis.

$$
\begin{aligned}
&m(\mu\mu) \notin [3050, 3144]\,\mathrm{MeV}/c^2, \\
&m(\mu\mu) \notin [3630, 3740]\,\mathrm{MeV}/c^2.
\end{aligned}
\tag{6.2}
$$

The `isMuon` PID-flag is a binary variable, which returns a true value, if the particle in question passes a sufficient number of Muon station [42].

A set of fiducial requirements is applied on the muon to remove regions with large muon detection asymmetries. In these areas, muons of one charge are more likely to be bent out of the detector's acceptance. The veto is enforced with the following requirement:

$$
\begin{aligned}
&|p_x| < 0.315 \cdot p_z - 1032.5\,\mathrm{MeV}/c, \\
&|p_x| > 1000\,\mathrm{MeV}/c \text{ OR } |p_x| < 700\,\mathrm{MeV}/c.
\end{aligned}
\tag{6.3}
$$

We impose additional PID requirements on the D^0 decay products and requirements on the visible mass of the B meson, *i.e.* $m(D^0\mu)$. The corrected B mass is is defined as $m_{corr}(B) \equiv \sqrt{m^2(D^0\mu) + p_\perp^2(D^0\mu)} + p_\perp(D^0\mu)$ and corrects for the unreconstructed B decay products based on $p_\perp(D^0\mu)$, *i.e.* the momentum of the $(D^0\ \mu)$ system perpendicular to the B flight direction. An additional selection, mostly used to reduce the combination of D^0 with an unrelated muon, is $p_\perp(D^0) < 1.5\,\text{GeV}/c + 1.1c \cdot (m_{corr}(B) - 4.5\,\text{GeV}/c^2)$. To further improve particle identification, we require the D^0 decay products to have high transverse momentum, which is in line with the requirements on the prompt channel $p_T(K,\pi) > 800\,\text{MeV}/c$. If an event is reconstructed with more than one B candidate, one is chosen at random. This removes 0.3% of events and has no visible effect on the $m(D^0)$ distribution. As with the prompt tagged event selection, we also check if an event is contained in both the RS and WS sample and if so attribute it to the RS sample. This requirement removes 0.3% of Wrong-Sign events without visible effect on the $m(D^0)$ distribution.

6.3 Material based selection

The selection steps presented in the two previous sections mostly follow the established analysis for WS-to-RS measurements in the channels. Since this analysis is focused on D^0 mesons with flight paths that intersect the RF-foils, additional selection criteria are applied.

We require that the D^0 mesons traverse at least 0.3 mm of RF-foil material. This quantity is calculated based on the charm-models presented in chapter 5. The value of 0.3 mm is equivalent to the RF-foil width and, thus, the minimal amount of material a particle can fly through while passing through the RF-foil.

Since we rely heavily on the charm-models, we only select events with D^0 decay vertices in the fiducial volume of the charm-models, *i.e.* $-10\,\text{mm} < y < 10\,\text{mm}$ and $-50\,\text{mm} < z < 300\,\text{mm}$.

The sample contains a large number of candidates that are consistent with decaying inside the foil. For this measurement, we are not interested in decay within the RF-foils, but only those D^0 candidates that decay in vacuum. To enforce this, we require the probability of the vertex being inside the RF-foils to be less than 0.3%, calculated based on the three-dimensional covariance of the reconstructed D^0 decay-vertex. For the semileptonic tag sample, we also enforce the same restriction on the B decay vertex, *i.e.* the D^0 production vertex.

Lastly, we also veto any candidates whose flight paths are consistent with intersecting one of the VELO sensor modules. This is done to have strong control over the amount and kind of material in the flight path, as the structure of the sensor modules is too complex to be included in the calculated material budget of a candidate.

In figure 6.2, we show the spatial distribution of events that pass this selection and are used in the analysis.

We can further examine their decay time and momentum distribution in figure 6.3. The prompt sample selects D^0 mesons with very long lifetimes, as they have to

Table 6.2: Summary of the selection criteria for RS and WS semileptonic decays.

Quantity	HLT2	Offline	Units
$p_T(K,\,\pi)$	> 200	> 800	MeV/c
p(K, π)	> 2	-	GeV/c
IP$\chi^2(K,\,\pi)$	> 9	-	-
PIDK (K)	> 5	> 7	-
PIDK (π)	< 0	< 0	-
$p_T(\mu)$	> 1	-	GeV/c
$p(\mu)$	> 3	-	GeV/c
IP$\chi^2(\mu)$	> 9	-	-
PIDμ (μ)	> 0	-	-
(π, K, μ): Track based ghost probability	< 0.4	-	-
D^0 vertex-fit χ^2/ndf	-	[0,9]	-
χ^2 distance D^0 vertex to PV	> 9	-	-
m(K π)	$[1.775, 1.955]$	-	GeV/c^2
χ^2 distance of closest approach between B decay products	< 10	-	-
B direction angle	< 45	-	mrad
m(B)	$[2.3, 10.0]$	$[3.1, 5.0]$	GeV/c^2
$m_{corr}(B)$	$[2.8, 8.5]$	$[4.3, 5.5]$	GeV/c^2
B vertex-fit χ^2/ndf	-	$[0, 9]$	-
$vtx_z(D^0)$ - $vtx_z(B)$	-	> 0	mm
J/ψ and $\psi(2S)$ veto	-	True	-
Vertex and `DTF` convergence	-	True	-
`DTF` χ^2/ndf (B)	-	$[0, 9.5]$	-
$p_\perp(D^0) < 1.5 + 1.1c{\cdot}(m_{corr}(B)$ - 4.5)	-	True	-
Muon fiducal requirement	-	True	-
μ `isMUON`	-	True	-
Multiple Candidate selection	-	True	-
Veto on WS candidates matched to RS candidates	-	True	-

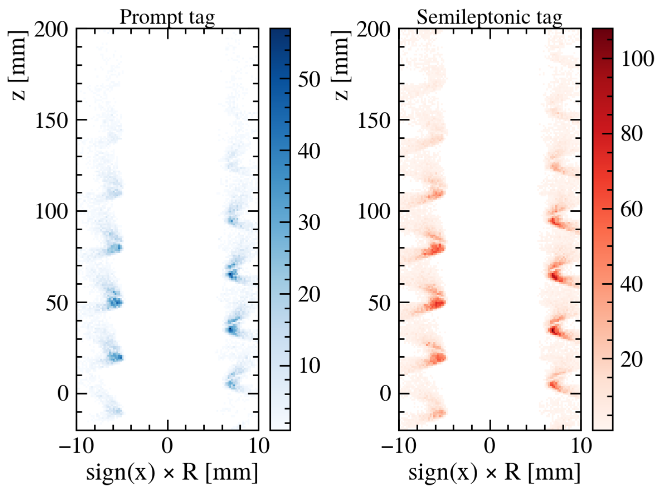

Figure 6.2: Shown are the spatial distribution of the D^0 decay vertices that passed the full selection for both the prompt and semileptonic tagged samples. We use the signed radius as a coordinate to separate the offset structure of both VELO halves.

survive to reach the RF-foil. The same is not true for the semileptonic tagged sample, as the B meson can be significantly displaced from the primary vertex. This gives us access to a wide range of decay times. For the same reason, we also implicitly select very high momentum D^0 candidates in the prompt sample.

In figure 6.4, we can see the distribution of the amount of material in the flight paths. For both samples, the mode is at about 0.6 mm. This is consistent with the distribution of the number of RF-foil intersects in each flight path as shown in figure 6.5, *i.e.* most selected D^0 mesons pass through the RF-foils only once and at a shallow angle. We can also make out peaks correlated to the subset of candidates with two intersects at 1.2 mm. In the bottom half of figure 6.4, we also see that for the semileptonic tag sample, the position of the first intersect is evenly distributed within the flight path, while for the prompt tag sample, they are distributed towards the right tail, as we would expect.

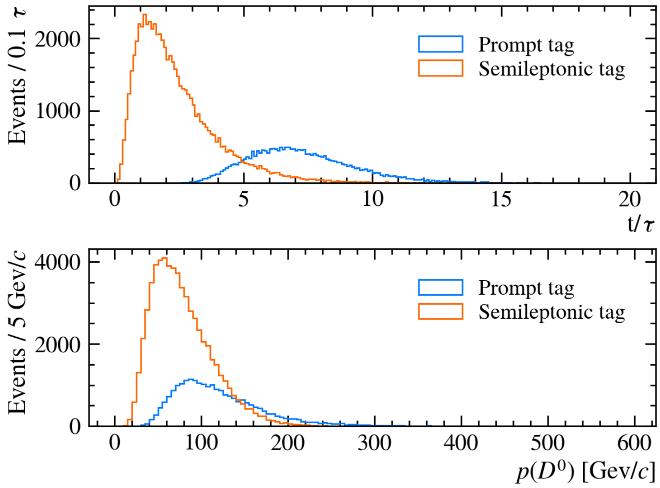

Figure 6.3: Top: Decay time distribution in units of mean D^0 lifetimes τ. Bottom: D^0 momentum distribution. Both are given for the prompt and semileptonic tagged samples.

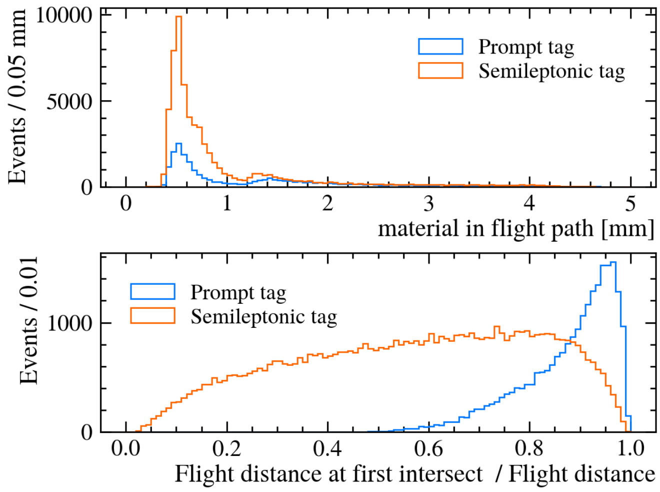

Figure 6.4: Top: Distribution of the amount of RF-foil material in the flight path in millimetres. Bottom: Distribution of the relative position of the first foil intersects within the D^0 flight path. Both are given for the prompt and semileptonic tagged samples.

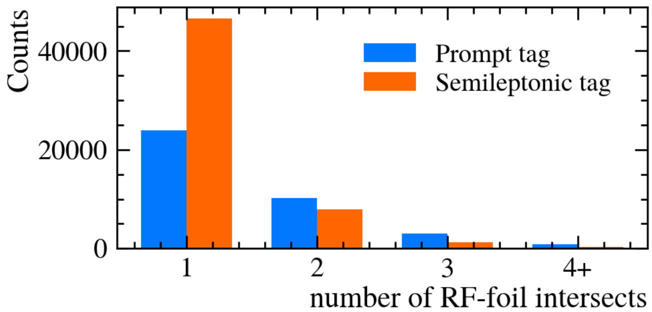

Figure 6.5: Distribution of the amount of RF-foil intersects for both the semileptonic and prompt tagged samples.

7 Determination of WS-to-RS ratios

In this analysis, we determine the ratio of Wrong-Sign to Right-Sign decays in simultaneous unbinned negative log-likelihood fits of the WS and RS signal peaks. Both signal peaks share the same shape with independent backgrounds and yields. We fit different quantities in the semileptonic and prompt tagged sample and thus have to describe the models separately. We perform time-integrated and decay time-binned measurements for both samples. Four equally populated bins are chosen for a minimum viable binning. The fitting tool zfit [43] is used to implement the fits.

7.1 Prompt decays

To determine the signal yields in the prompt tagged sample, we fit the signal peaks in the $\Delta m \equiv m(K\pi\pi_s) - m(K\pi)$ distributions. For the calculation of Δm we use a `DTF` offline reconstruction that enforces the origin vertex to be the primary vertex and the reconstructed D^0 mass to be the PDG value. A fit on this quantity is chosen to safeguard against random soft pions mistags.

The signal is described by a Johnson S_U function [44]

$$\mathscr{J}(x|\mu,\sigma,\delta,\gamma) = \frac{\exp(-\frac{1}{2}\left[\gamma + \delta\sinh^{-1}\left(\frac{x-\mu}{\sigma}\right)\right]^2)}{\sqrt{1+\left(\frac{x-\mu}{\sigma}\right)^2}}, \tag{7.1}$$

which accounts for most of the asymmetric tails of the distribution, to which we add two independent Gaussian distributions modelling the core of the distribution. The background, which we assume to be composed of random associations of tracks, *i.e.* combinatorial background, is best described by a flipped ARGUS function [45]

$$\mathscr{A}(x|m_0,c,p) = (2m_0 - x)\left[1-\left(\frac{2m_0-x}{m_0}\right)^2\right]^p \exp\left[c\left(1-\left(\frac{2m_0-x}{m_0}\right)^2\right)\right], \tag{7.2}$$

where the parameter m_0 is fixed to the pion mass. The complete model is given as

$$\begin{aligned}
\mathbb{P}^{\mathrm{Y}}(m) \quad &= N^{\mathrm{Y}}_{\mathrm{sig}} \cdot [f_{\mathrm{J}}\mathscr{J}(m|\mu_{\mathrm{J}},\sigma_{\mathrm{J}},\delta_{\mathrm{J}},\gamma_{\mathrm{J}}) \\
&\qquad + f_{\mathrm{G1}}\mathscr{G}(m|\mu_{\mathrm{G1}},\sigma_{\mathrm{G1}}) + f_{\mathrm{G2}}\mathscr{G}(m|\mu_{\mathrm{G2}},\sigma_{\mathrm{G2}})] \\
&\quad + N^{\mathrm{Y}}_{\mathrm{bkg}}\mathscr{A}(m|m_\pi,c^{\mathrm{Y}},p^{\mathrm{Y}}),
\end{aligned} \tag{7.3}$$

Table 7.1: Results for the simultaneous fit of R in the prompt sample, given for each decay time bin.

Decay time bin [t/τ]	R [10^{-3}]
2.2 - 5.3	6.3 ± 1.8
5.3 - 6.6	7.2 ± 1.3
6.6 - 8.2	7.0 ± 1.1
8.2 - 15.0	8.8 ± 1.6
Time-integrated	7.4 ± 0.8

Table 7.2: Results of the fitter evaluation using pseudo-experiments in the prompt sample, given for each decay time bin.

Decay time bin [t/τ]	μ	σ
2.2 - 5.3	1.01	0.24
5.3 - 6.6	1.01	0.18
6.6 - 8.2	0.98	0.18
8.2 - 15.0	1.00	0.15
Time-integrated	1.01	0.12

where $Y = \{\text{RS, WS}\}$, so that the shape parameters of the signal are shared in each decay time bin and we can easily extract the target quantity $R = \frac{N_{\text{sig}}^{\text{WS}}}{N_{\text{sig}}^{\text{RS}}}$. The advantage of using a simultaneous fit is that the correlation of the shape parameters on R can be fully considered. The distributions with the fit projections overlaid are reported in Appendix B. The fit results are listed in the table 7.1.

7.1.1 Fitter bias

To evaluate the accuracy of the fits and possible bias, we evaluate the fitter using pseudo-experiments. The fit results in table 7.1 include uncertainties that are given as part of the fitting tool and based on the negative log-likelihood. For each fit, we run 100 pseudo-experiments, where a sample is created according to the original fit, allowing for statistical variation in both sample sizes. The fitting tool is initialised with randomised values to avoid bias and refitted. The results for each of the decay time bins are depicted in figure 7.1, we fit a Gaussian distribution to the normalised values $\frac{R_{\text{fit}}}{R_{init}}$. The results of these fits are listed in table 7.2. We see that the mean is close to unity for each decay time bin. This means that the fit returns, on average, the same values for R with which we initialised the pseudo-experiment, *i.e.* the fit is unbiased. We also compare the width of the Gaussian to the uncertainty returned by the fitting tool and see that the fitter returns an accurate uncertainty on the result.

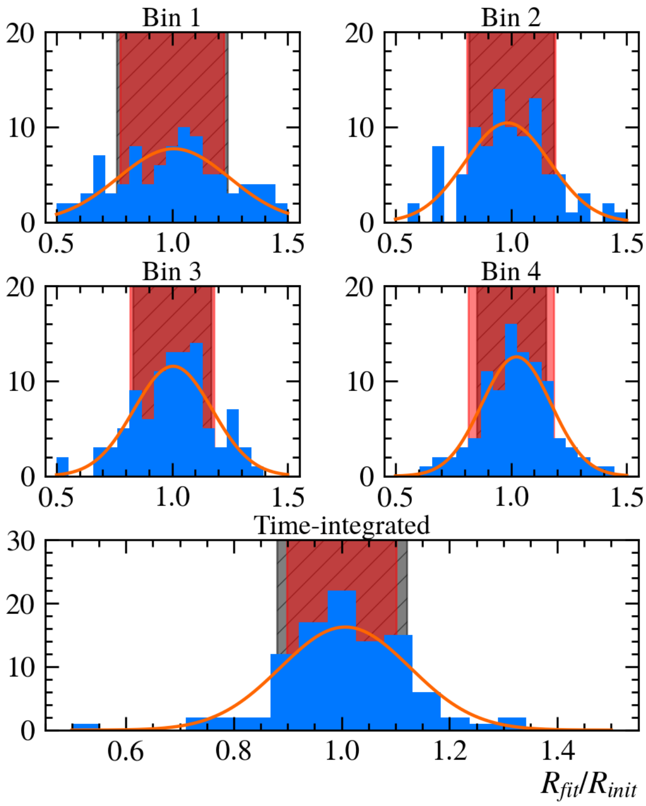

Figure 7.1: The results of the pseudo-experiments for each decay time bin are depicted, as well as a Gaussian distribution fitted to the distributions. The red field covers the one σ interval of the Gaussian and the hatched area is the fit uncertainty calculated by the fitter tool.

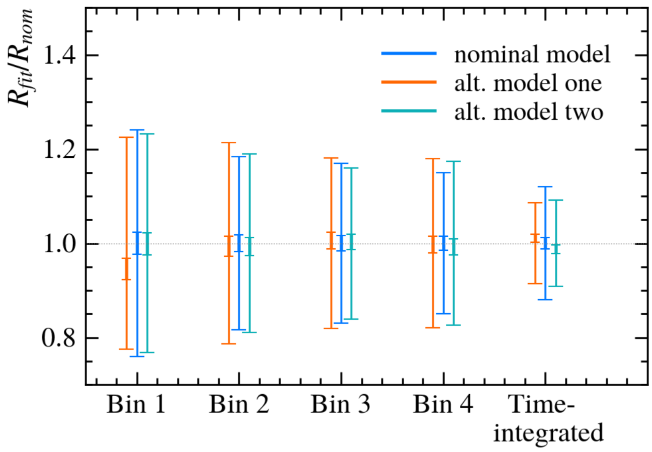

Figure 7.2: We compare the results of the ratio R, when different model are used to describe the distributions of the prompt tagged sample in all decay time bins. The inner error bars indicate the uncertainty of the mean, while the outer error bars indicate the uncertainty of an individual fit.

7.1.2 Model choice uncertainty

Since the model choice for signal and background is not purely dictated by the underlying physical process, the choice of model is a source of systematic uncertainty. In order to evaluate this uncertainty, we perform the fitting procedure with alternative models to describe the distributions. To factor out the statistical uncertainty, we first fit the nominal model and then sample from this distribution in the same manner described above. We again perform 100 of these pseudo-experiment fits. This lets us effectively factor out the fitting and statistical uncertainty so we can compare the mean of the distributions. The first alternative model removes one of the Gaussian distributions that make up the signal shape. A second alternative model replaces the Johnson S_U distribution with a double Crystal Ball function [46], *i.e.* a Gaussian distribution augmented with power law tails on both sides. The results are shown in figure 7.2. Only the time-integrated measurement and the alternative model in the first decay time bin give any indication of a possible bias. We include and evaluate this as a systematic uncertainty in chapter 10.

7.2 Semileptonic decays

To determine the yield in the semileptonic tagged sample, we fit the signal peak in the $m(K\pi)$ distribution. The signal is described by a Crystal ball function [46], which is defined as

Table 7.3: Results for the simultaneous fit of R in the semileptonic sample, given for each decay time bin.

Decay time bin [t/τ]	R [10^{-3}]
0.1 - 1.3	4.8 ± 0.6
1.3 - 2.0	5.8 ± 0.7
2.0 - 3.1	5.2 ± 0.7
3.1 - 7.5	6.5 ± 0.8
Time-integrated	5.56 ± 0.35

$$\mathscr{CB}(x;\mu,\sigma,\alpha,n) = \mathscr{N}_{\mathscr{CB}} \cdot \begin{cases} \exp\left(-\frac{(x-\mu)^2}{2\sigma^2}\right) & \text{if } \frac{x-\mu}{\sigma} > -\alpha, \\ A \cdot (B - \frac{x-\mu}{\sigma})^{-n} & \text{if } \frac{x-\mu}{\sigma} \leq -\alpha, \end{cases} \tag{7.4}$$

with

$$\begin{aligned} A &= \left(\frac{n}{|\alpha|}\right)^n \cdot \exp\left(-\frac{|\alpha|^2}{2}\right), \\ B &= \frac{n}{|\alpha|} - |\alpha|, \end{aligned} \tag{7.5}$$

and $\mathscr{N}_{\mathscr{CB}}$ as the normalisation factor. This distribution augments a Gaussian core with a polynomial low-end tail. We add an independent Gaussian distribution to the signal model.

The background model is a simple linear model, with the addition of a Gaussian peak in the lower sideband to catch the $D^0 \to KK$ contamination (see chapter 7), giving us a total distribution of:

$$\begin{aligned} \mathbb{P}^{\mathrm{Y}}(m) \quad &= N^{\mathrm{Y}}_{\mathrm{sig}}[f_{\mathrm{CB}}\mathscr{CB}(m|\mu_{\mathrm{J}},\sigma_{\mathrm{J}},\delta_{\mathrm{J}},\gamma_{\mathrm{J}}) \\ &\qquad + f_{\mathrm{G1}}\mathscr{G}(m|\mu_{\mathrm{G1}},\sigma_{\mathrm{G1}})] \\ &+N^{\mathrm{Y}}_{\mathrm{bkg}}[\mathscr{L}(m|a^{\mathrm{Y}},b^{\mathrm{Y}}) + f^{\mathrm{Y}}_{\mathrm{G2}}\mathscr{G}(m|\mu^{\mathrm{Y}}_{\mathrm{G2}},\sigma^{\mathrm{Y}}_{\mathrm{G2}})], \end{aligned} \tag{7.6}$$

where $Y = \{\mathrm{RS}, \mathrm{WS}\}$ so that the shape parameters of the signal are shared. As in the prompt tag case, we calculate $R = \frac{N^{\mathrm{WS}}_{\mathrm{sig}}}{N^{\mathrm{RS}}_{\mathrm{sig}}}$ as part of the simultaneous fit, thus including the full covariance between the yields of both fits. The distributions with the fit projections overlaid are reported in Appendix B. The results are listed in table 7.3.

7.2.1 Fitter bias

To evaluate the uncertainty and bias of the fits, we follow the same procedure as for the prompt sample. The distributions are depicted in figure 7.3 and the fitted mean

Table 7.4: Results of the fitter evaluation using pseudo-experiments in the semileptonic sample, given for each decay time bin.

Decay time bin [t/τ]	μ	σ
0.1 - 1.3	1.00	0.10
1.3 - 2.0	1.00	0.10
2.0 - 3.1	1.00	0.13
3.1 - 7.5	1.00	0.11
Time-integrated	1.01	0.05

and width are listed in table 7.4. We again see no evidence for a bias and that the fitter returned an accurate estimate for the uncertainty on R.

7.2.2 Model choice uncertainty

As in the prompt tagged sample, we evaluate the influence of model choice on the observed R value by repeating the measurement with altered models. The first alternative model implements a more complex background by using a second order Legendre Polynomial in place of a first order one. The second alternative model replaces the simple crystal ball function with a double crystal ball function, adding additional degrees of freedom to the signal shape. As in the prompt case, we factor out the statistical uncertainty with the use of pseudo-experiments. In figure 7.4 we see that for the individual bin, there are some deviations in the mean that could contribute to a bias on the order of two per cent. While these potential sources of bias are small compared to the statistical uncertainty, we will evaluate their influence on the measurement as a systematic uncertainty in chapter 10.

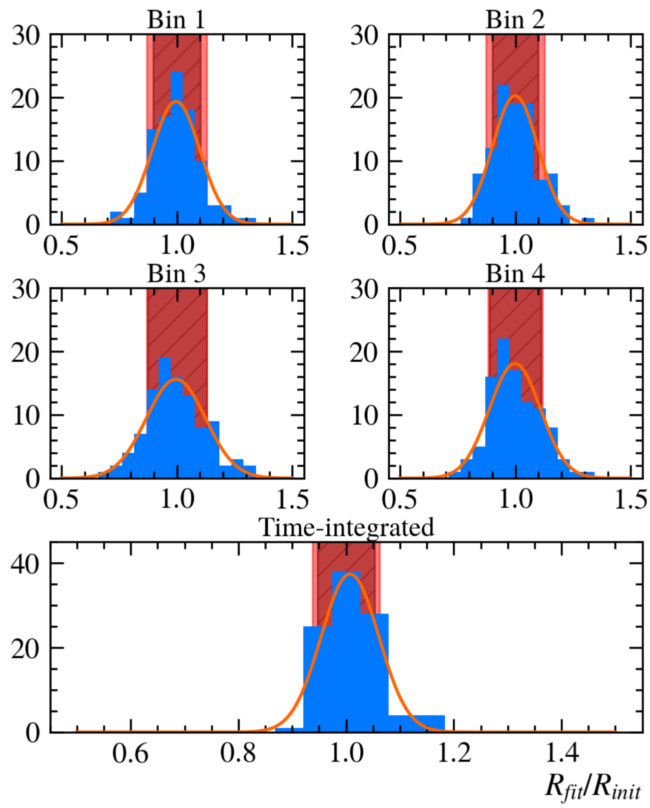

Figure 7.3: The results of the pseudo-experiments for each decay time bin are depicted, as well as Gaussian distributions fitted to the results of the pseudo-experiments. The red field covers the one σ interval of the Gaussian and the hatched area is the fit uncertainty calculated by the fitter tool.

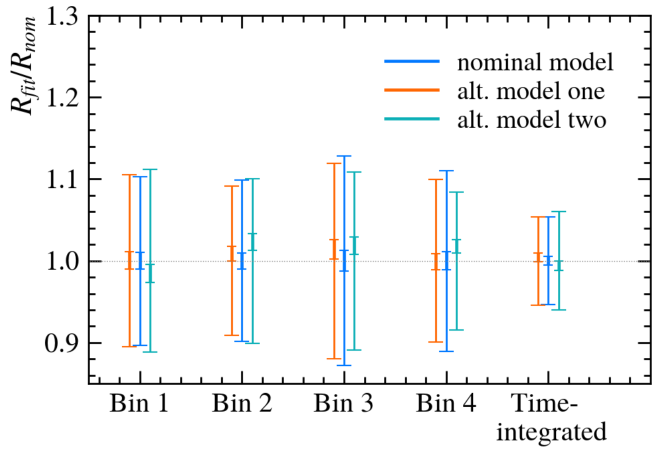

Figure 7.4: We compare the results of the ratio R, when different models are used to describe the distributions of the prompt tagged sample in all decay time bins. The inner error bars indicate the uncertainty of the mean, while the outer error bars indicate the uncertainty of an individual fit.

8 Peaking Background

Backgrounds that produce a narrow enhancement in the signal regions of the Δm or $m(K\pi)$ distributions are called peaking backgrounds. They can introduce a bias into the measurement of the WS-to-RS yield ratios and thus need careful consideration.

In this chapter, we use phase-space simulations to study the shape of potential backgrounds. These simulations are performed using the RapidSim [47] application. RapidSim does not perform a full simulation of the LHCb detector or the underlying proton-proton collision but still generates heavy-flavour hadron decays with realistic production kinematic distributions, efficiencies and momentum resolutions. In addition, it includes momentum smearing based on the finite detector resolution as observed in calibration measurements. We use events generated with RapidSim to investigate invariant mass distribution of several decays under altered mass hypothesis or with unreconstructed final state particles.

8.1 Prompt tagged sample

Any background that can introduce a narrow enhancement into the Δm signal range is a potential source of bias. The most important source are reflection backgrounds, *i.e.*D^0 decays of the form $D^0 \to h^+h^{(\prime)-}$, where $h, h^{(\prime)}$ are either pions or kaons, and one or both final-state particles are misidentified. These backgrounds are generally suppressed by PID or kinematic restrictions. These reflection backgrounds have, in general, $m(K\pi)$ values that do not coincide with the D^0 mass. However, in the calculation of the Δm we use the `DTF` algorithm that includes a constraint on the D^0 mass. Thus we still obtain a peaking contribution to the signal region.

In this chapter, we estimate the size of residual contamination. To study the effect of real charm decays with misidentified final states in the signal region, we investigate the kinematic suppression of the reflection backgrounds. Following Ref. [48] and previous WS-to-RS analysis [30], we use kinematic correlation to estimate the size of reflection backgrounds. This method exploits the correlation between the signed momentum imbalance of the $D^{*+} \to D^0(\to h^+h^{(\prime)-})\pi_s^+$ decay,

$$\beta^* = q(\pi_s)\frac{p_+ - p_-}{p_+ + p_-}, \tag{8.1}$$

where $q(\pi_s)$ is the charge of the soft pion and $p_\pm$ is the momentum of the positively- or negatively-charged D^0 decay product, respectively. This variable is set in relation to the D^0 mass calculated with the assumption of the charged pion mass for both D^0 decay products, *i.e.* $m(\pi\pi)$. Figure 8.1 show the distinctive shape of each

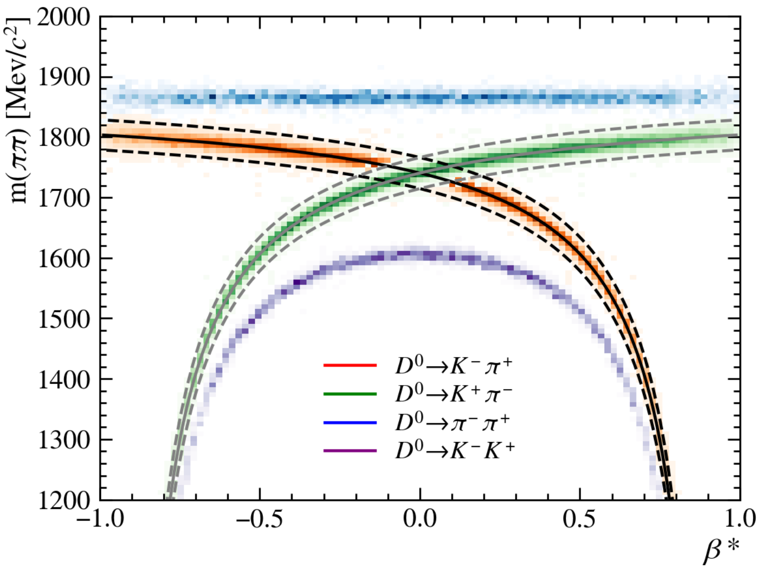

Figure 8.1: Illustration of the correlation between $m(\pi\pi)$ and β^* for the four possible $D^0 \to h^+h^{(\prime)-}$ decays. The coloured samples are simulated with momentum smearing. The black and grey lines indicate a band of $\pm 3\sigma$ around the analytical shape of RS and WS decays.

$D^0 \to h^+h^{(\prime)-}$ decay in this plane. We use this $(\beta^*, m(\pi\pi))$ plane to visualise and estimate the peaking background contribution to the signal region.

We study the peaking backgrounds in the two-dimensional sideband of $(\beta^*, m(\pi\pi))$ and extrapolate the size of the peaking contributions into the signal region $|m(K\pi) - m_{D^0}| < 24\,\text{MeV}/c^2$ as visualised in figure 8.2. The sideband is defined by $|m(K\pi) - m_{D^0}| > 40\,\text{MeV}/c^2$. Since the sideband is defined at a threshold equivalent to a 5σ deviation from the reconstructed D^0 mass, no signal is expected in it. In chapter 6 we outlined several requirements that restrict the D^0 mass and the D^0 mass reconstructed using different mass hypotheses for the D^0 decay products. In the following, we work with a sample to which these restrictions are not applied. This allows us to see the full size of the background and better estimate the relevant tails.

In order to understand the individual contributions to the sideband, we separate the following sidebands out of the WS and RS samples:

- $D^0 \to K^+K^-$ sideband, where we replace the pion mass with the kaon mass and select $|m(K^+K^-) - m_{D^0}| < 24\,\text{MeV}/c^2$;
- $D^0 \to \pi^+\pi^-$ sideband, where we replace the kaon mass with the pion mass and select $|m(\pi^+\pi^-) - m_{D^0}| < 24\,\text{MeV}/c^2$;
- and a $K\pi$-swap sideband, where we swap both kaon and pion masses and select $|m(K\pi_{sw}) - m_{D^0}| < 24\,\text{MeV}/c^2$.

Each of these samples also includes the general sideband requirement $|m(K\pi) -$

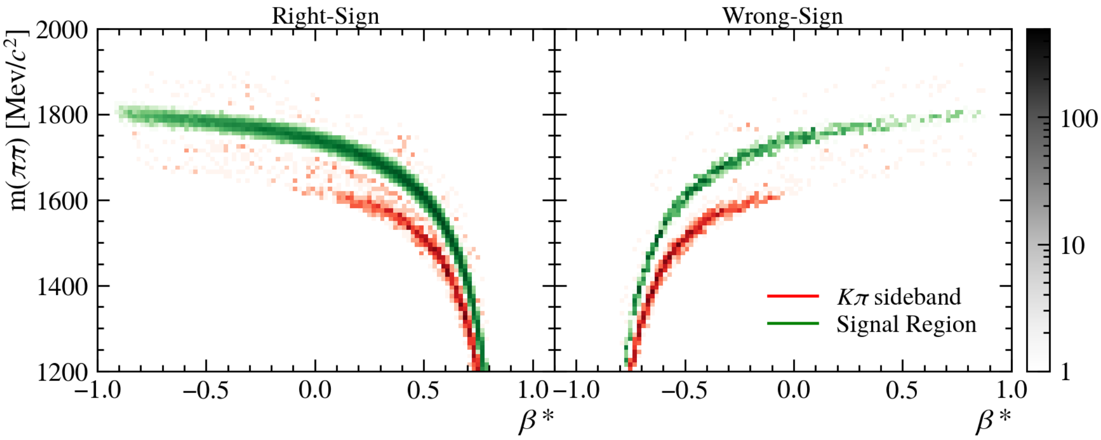

Figure 8.2: Sample decomposed into signal samples (green) meeting the $m(K\pi)$ mass requirement and the sideband (red) removed by 5 σ.

$m_{D^0}| > 40\,\text{MeV}/c^2$, so that we are certain these samples do not include any signal events and they are kinematically plausible to have originated from one of the other $D^0 \to hh^{(\prime)}$ decays. These sidebands are selected from both the RS and WS samples.

In the selection (see chapter 6) we require that the $D^0 \to K^+K^-$ and $D^0 \to \pi^+\pi^-$ decays are excluded with a 5σ mass requirement. However, we do not have a suppression requirement for the doubly misidentified background. In this case, a RS decay is included in the WS sample or vice versa. This kind of background falls into the signal region if the momenta are symmetric, *i.e.* the RS and WS bands in figure 8.1 overlap near $\beta^* = 0$. It is worth noting that this background is expected to be much larger in the WS sample since its size is proportional to the size of the RS sample. In the RS sample, the doubly misidentified background is proportional to the size of the WS sample and, therefore, about a factor R_D larger.

In figure 8.3 we show the samples with the sidebands as explained above. We see that neither sample contains a large sample of $D^0 \to \pi^+\pi^-$, while the $D^0 \to K^+K^-$ is strongly expressed in both the RS and the WS sample. The doubly misidentified background is more prominent in the WS sample.

To confirm that these sidebands also lead to narrow enhancements in the Δm signal region, we plot the Δm distributions of the sideband defined above, shown in figure 8.4. For the RS samples, the combined sidebands peak at about 3% of the signal peak size, with almost all the contributions coming from the $D^0 \to K^-K^+$ sideband (see left column, lower row in Fig. 8.4), which is easily suppressed kinematically. We can estimate the suppression by the selection requirement, $|m(K^+K^-) - m_{D^0}| > 40\,\text{MeV}/c^2$ and $|m(K^-\pi^+) - m_{D^0}| < 24\,\text{MeV}/c^2$ (see chapter 6) using RapidSim generated $D^0 \to K^+K^-$ decays, scaling the yield to match the sideband population. From this, we infer that any effect of the $D^0 \to K^-K^+$ background, after the full selection requirements are applied, is smaller than 0.1% of the RS yield. Therefore, we neglect them. The same is true for the $D^0 \to \pi^-\pi^+$ and doubly misidentified

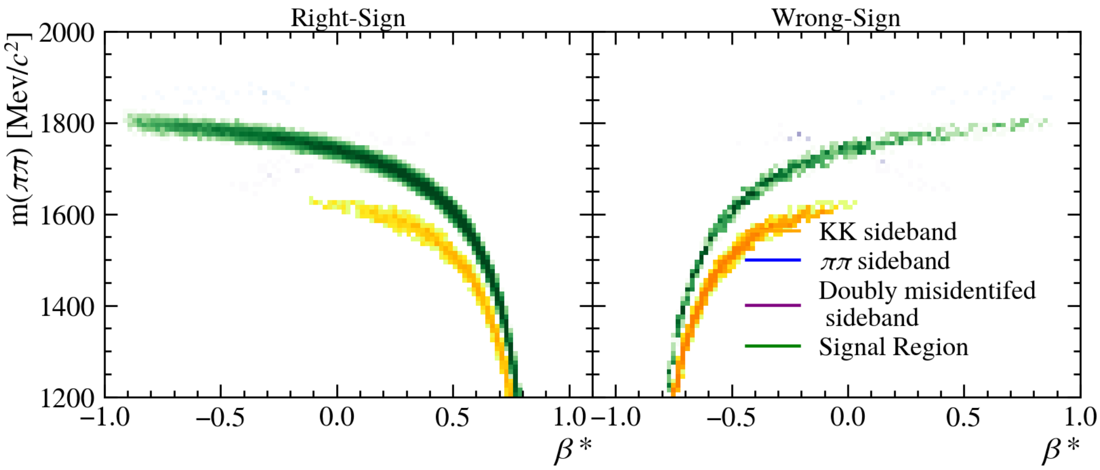

Figure 8.3: Sidebands decomposed into (Blue) $\pi\pi$-sideband, (orange) KK-sideband and the $K\pi$-swap sideband (Purple). RS and WS samples do not share the same scale and colourmap.

backgrounds in the RS sample. It is reasonable to neglect these small background contributions since the number of RS events is large and appears in the denominator of the WS-to-RS ratio. Thus the measurement is insensitive to them.

For the WS sample, we see in the right column of figure 8.4 that the total number of decays attributed to the sidebands is larger than the number of decays in the signal region. In the bottom right panel of figure 8.4 we see that the sideband is mostly made up of $D^0 \to K^+K^-$ background. We follow the same extrapolation as above and once again, we see that neither the $D^0 \to K^+K^-$ nor the $D^0 \to \pi^+\pi^-$ backgrounds are significant for the measurement. For the RS sample, it was reasonable to ignore the doubly misidentified background on size alone. However, this is not possible for the WS sample since the total number of WS signal events is much smaller and appears in the numerator of the WS-to-RS ratio. Therefore the analysis is sensitive to this background. We now further investigate the doubly misidentified background of the WS sample.

We need to extrapolate the size of the doubly misidentified background into the signal region. A good proxy for the doubly misidentified background shape in the Δm signal region is to take events from the RS signal sample and swap the mass hypothesis. In figure 8.5 (a), we see in dark blue the upper limit on the doubly misidentified background deduced from the RS sample, *i.e.* the properly reconstructed RS decays that after swapping the mass hypothesis still fall into the Δm signal region, scaled by a factor of 0.45%. The light blue distributions are the doubly misidentified background candidates in the sideband of the WS sample, *i.e.* those events in the WS sideband that are kinematically plausible to come from a doubly misidentified decay.

The scale factor (0.45%) of the shape taken from RS events is determined in a binned χ^2 fit of the RS shape (dark blue) to the WS doubly misidentified background

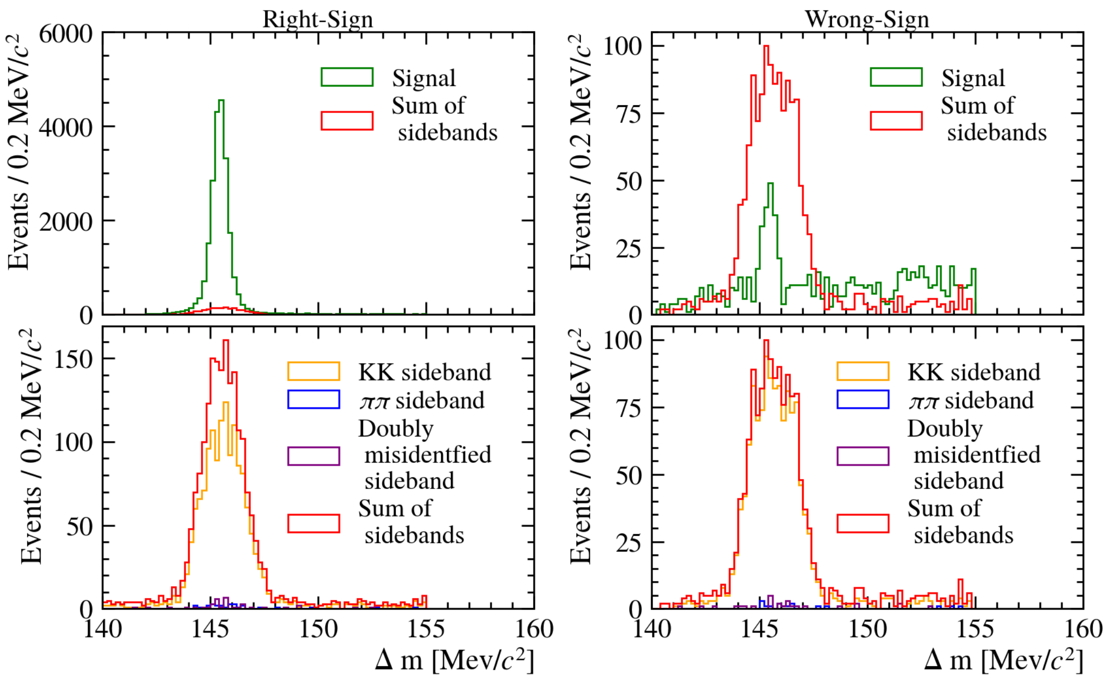

Figure 8.4: Δm distributions for RS samples on the left and WS samples on the right. Green (top row) events in the $K\pi$ signal region, red (all rows) are the events in the $K\pi$ sideband, in the second row orange events in the KK sideband, blue events in the $\pi\pi$ sideband and purple events in the doubly misidentified sideband.

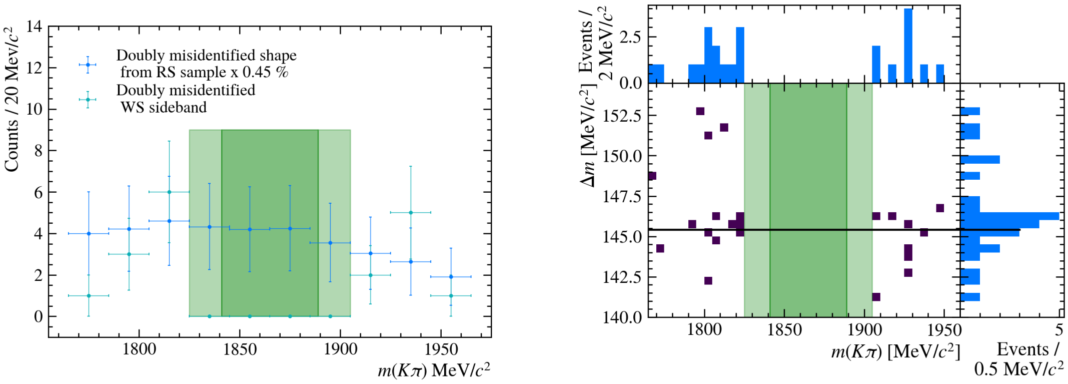

(a) (b)

Figure 8.5: a) The figure shows the peaking $K\pi$-swap contributions to the WS sample on both sides of the signal band in light blue. In dark blue, we model the expected shape by changing the mass hypothesis for events of the RS signal sample.
b) 2d distribution of the $K\pi$-swap background showing the reconstructed $K\pi$ mass as well as Δm.
In both figures, the dark green regions are the 3σ m(D^0) regions and the light green ones are the 5σ regions.

candidates in the sideband (light blue). This scale factor allows us to extrapolate the doubly misidentified sideband into the $m(K\pi)$ signal region. We assume that all these events are also peaking backgrounds in (Δm). This is justified by the two-dimensional distribution of the doubly misidentified sideband in the $(m(K\pi), \Delta m)$ plane, shown in figure 8.5 (b). From this, we can infer that the total contribution to the WS signal region by RS doubly misidentified signal would be about ten decays or two per cent of the total WS signal yield. This value is consistent with previous analyses. However, the uncertainty on this value is large as we have limited data. We assume a Poisson uncertainty for the peaking background, such that the size of the peaking background is estimated as $P = (10 \pm 3.2)$.

8.2 Semileptonic tagged sample

There are two important kinds of backgrounds in the semileptonic sample. First, there is the combination of a genuine $D^0 \to K\pi$ decay with a random muon in the event. Such events cannot be distinguished from a correctly tagged decay in the D^0 mass spectrum as a genuine D^0 decay was reconstructed. We also refer to this background as mistagged. The second kind of background is where no real $D^0 \to K\pi$ decay was reconstructed. These will generally result in deviations in the D^0 mass. The analysis of the semileptonic tagged sample is less susceptible to peaking background because we evaluate the WS-to-RS ratio directly on the $m(K\pi)$ distribution, which was, unlike Δm in the prompt sample, not reconstructed with a D^0 mass constraint. This has the trade-off that we are more susceptible to

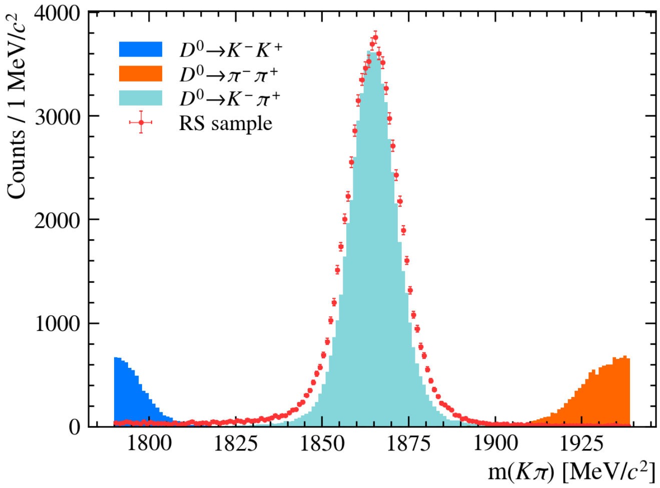

Figure 8.6: The invariant $m(K\pi)$ distributions of simulated $D^0 \to K^-K^+$, $D^0 \to \pi^-\pi^+$ and $D^0 \to K^-\pi^+$(RS) decays are shown. Overlaid is the invariant $m(K\pi)$ distribution of the RS data sample.

mistagging backgrounds.

To summarise, the backgrounds from misreconstructed D^0 decays do not peak in the signal $\mathrm{m}(K\pi)$ region. In the following, we explain possible sources of backgrounds and why they do not constitute peaking backgrounds. The relevant background for the semileptonic sample is the mistagging due to the association of random muons, explained at the end of this section.

8.2.1 Reflection background

Reflection backgrounds stem from two-body decays of D^0 mesons where the final state particles are misidentified, as discussed in the prompt case.

The dominant sources of reflection background for the RS decay are the singly Cabbibo-suppressed $D^0 \to K^+K^-$ and $D^0 \to \pi^+\pi^-$ decays. Both these contributions also arise in the WS sample with the addition of the doubly misidentified RS decay. We expect the $D^0 \to K^+K^-$ decays to be the most significant background contribution to the RS sample, as in the prompt case. In figure 8.6 we show the $m(K\pi)$ distributions of RapidSim generated $D^0 \to K^+K^-$ and $D^0 \to \pi^+\pi^-$ decays in dark blue and orange respectively. In light blue, we show the simulated RS decays. The simulated samples are scaled for visual presentation and the scales hold no physical meaning. We include these samples to show the shape and position of both backgrounds. In red, we include the RS sample, here, we see no appreciable peaks in the positions where the reflection backgrounds are expected. No peaking contributions in the $m(K\pi)$ signal region from the reflection backgrounds are expected.

We expect these backgrounds to be more prominent for the WS sample since the background sources are now Cabbibo favoured relative to the DCS signal decay.

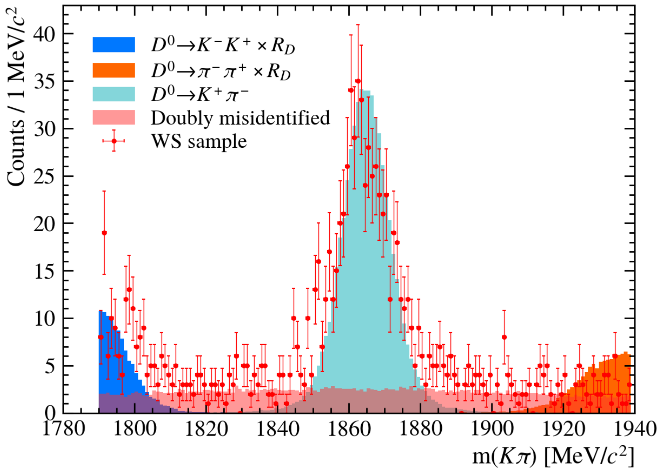

Figure 8.7: The invariant $m(K\pi)$ distributions of simulated $D^0 \to K^-K^+$, $D^0 \to \pi^-\pi^+$ and $D^0 \to K^+\pi^-$(WS) decays are shown. Overlaid is the invariant $m(K\pi)$ distribution of the WS data sample. In red is the distribution of the RS sample after the mass hypotheses are swapped and scaled down to 1%. This is the expected shape for doubly misidentified decays.

In figure 8.7 we now see enhancements in the lower sideband that we attribute to $D^0 \to K^-K^+$ backgrounds. However, this background is Gaussian shaped and does not peak in the $m(K\pi)$ signal region. So, as in the RS case, we do not expect peaking contributions from $D^0 \to K^+K^-$ and $D^0 \to \pi^+\pi^-$ decays. In addition, we would expect doubly misidentified decays to appear in significant numbers in the WS sample, as explained in the prompt case. We can simulate the shape of a doubly misidentified background by swapping the mass hypothesis of the RS sample. The background distribution is shown in red in figure 8.7, scaled to 1%, a similar value as obtained in the prompt case. We see that this background produces a flat $m(K\pi)$ distribution; thus, we do not expect a peaking background contribution from doubly misidentified decays.

8.2.2 Multibody *B* decays

Multibody B decays are dangerous backgrounds when a D^0 decay is incorrectly reconstructed from particles that result directly from the B decay.

Previous analyses of these channels, such as that described in Ref. [49], have identified the decays $B \to J/\psi\pi^{\pm}X$ or $B \to J/\psi K^{\pm}X$ as the dominant background in this category. In the case of $J/\psi \to \mu^+\mu^-$ one of the muons can be identified as the tag muon and the other is misidentified as a meson in the D^0 reconstruction. Since muons are more likely to be misidentified as kaons, we expect this background to be more prominent in the WS sample. However, since we require that foil material is located between the B decay vertex and the D^0 decay vertex, these two are not allowed to coincide, which should already suppress these backgrounds quite

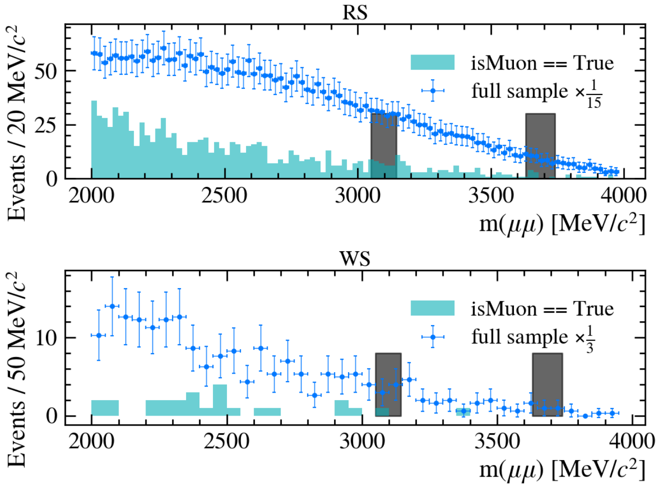

Figure 8.8: The invariant $m(\mu\mu)$ distributions for the RS (top) and WS (bottom) samples. The light blue distribution enforces the `isMuon` flag, while the dark blue distribution shows the full sample scaled down. The grey areas are those associated to the resonances.

aggressively. It is possible to remove this background by applying a veto to the charmonium resonances. This is done by selecting the muon and the oppositely charged D^0 decay product and calculating the invariant $\mu\mu$ mass. We remove events where the D^0 decay product with opposite charge of the muon tag charge has the `isMuon` PID flag and the reconstructed $m(\mu\mu)$ value falls in the regions of the J/ψ ($[3050, 3144]\,\mathrm{MeV}/c^2$) or $\psi(2S)$ ($[3630, 3740]\,\mathrm{MeV}/c^2$) resonances. The distribution of the $\mu\mu$ invariant mass is shown in figure 8.8, here, we can see that only the RS sample shows a peak in one of the veto regions (marked grey in the figure). These peaks are also significantly smaller than those in similar analyses without a material requirement. In addition, the analysis presented in Ref. [50] also showed that this does not result in a peak in the D^0 mass spectrum.

8.2.3 Multibody *D* decays

Decays of a D meson into three or more final state particles pose a potential background. However, these decays will generally not result in sharp peaks in the D^0 signal region, as one or more particles are misreconstructed or not reconstructed. Since the production rate of c-hadron is much larger than the production rate of b-hadron it is important to suppress D-mesons produced in the primary interaction. Our reconstruction process effectively filters out the background resulting from D produced in the primary interaction by requiring a minimum reconstructed B mass of $3.1\,\mathrm{GeV}/c^2$ and a displaced B vertex. In the following, we examine the kinematics of these backgrounds using events generated by RapidSim to evaluate if they can result in a peaking background.

Neutral $\boldsymbol{D}$ decays of the type $D^0 \to h^- h^{(\prime)+} h^0$ have higher branching fractions than their two body equivalents. In the decays $D^0 \to K^- K^+ h^0$ the neutral meson would be missed in the reconstruction and one of the kaons identified as a pion. Since both of these processes lead to a lower reconstructed D^0 mass, they do not contribute a peaking background. The $D^0 \to K^- \pi^+ h^0$ decay also has an unreconstructed particle and thus lower reconstructed mass and does not lead to a peaking contribution. The last case $D^0 \to \pi^- \pi^+ h^0$ is the most interesting, as lower mass is reconstructed due to the unreconstructed neutral meson. However, the pion to kaon misidentification adds to the reconstructed mass. This means we see decays in the signal region, but they do not peak and can be absorbed in the background model.

Charged $\boldsymbol{D}$ decays can be reconstructed as a D^0 decay missing a charged meson, most likely a pion. The decays $D^+ \to K^- \pi^+ \pi^+$ and $D^+ \to K^- K^+ \pi^+$ are favoured because of their branching fractions, but as above, do not contribute to the signal region due to the lower reconstructed mass. Only the decay $D^+ \to \pi^- \pi^+ \pi^+$ contributes to the signal region, but not in a peaking shape, as explained above.

$\boldsymbol{D_s^+}$ decays carry additional mass, which can compensate for lower reconstructed mass resulting from an unreconstructed particle. The obvious candidate $D_s^+ \to K^+ \pi^+ \pi^-$ has a low branching fraction but falls short of contributing to the signal region. The same is true for the more likely purely pionic decay $D_s^+ \to \pi^+ \pi^+ \pi^-$ gains mass in the reconstruction via a pion to kaon misidentification.

Semileptonic decays can contribute a background by misidentifying the charged lepton as a hadron. The misidentification of the lepton as a pion is more likely than as a kaon. Therefore the decays $D^0 \to K^- \ell^+ \nu_\ell$ and $D^+ \to K^- \pi^+ \ell^+ \nu_\ell$ are expected to be the leading contributions. From the RapidSim-generated events, we see that these decays do not contribute a peak to the signal region.

8.2.4 Baryonic background

The decay of $\Lambda_b \to \Lambda_c \mu X$ mimics the decay chain of the signal. The most likely Λ_c decay to lead to a background in the D^0 mass is $\Lambda_c \to p K^- \pi^+$, where one particle must always be missing in the reconstruction, thus leading to a loss in reconstructed D^0 mass. When either p or K are missing, the reconstructed masses are shifted so far that no decays are expected in the signal region. Only the reconstruction that misses the kaon and identifies the proton as a pion leads to a smooth tail reaching into the signal region. This background can be absorbed in our background model. No peaking backgrounds from baryonic decays are expected.

8.2.5 Random muon background leading to mistagging

In the yield determination for the semileptonic mode, we only fit the reconstructed D^0 mass. This means we cannot separate between the reconstruction of genuine semileptonic production of a D^0 or the combination of a real D^0 decay with a random muon. In the event selection (see chapter 6), we control against this background by having certain requirements on the decay topology. However, sources of random muons and prompt D^0 are plentiful and thus, random muon combinations can lead to a relevant background. Furthermore, since we expect an equal number of incorrectly tagged decays in the RS and WS samples, this leads to an enhancement in the WS-to-RS ratio. These events also have an incorrectly reconstructed decay time, thus leading to increased uncertainty in the measurement.

We perform a measurement of the muon mistag probability by investigating the Right-Sign doubly tagged sample, which contains $B \to D^{*+}(\to D^0\pi^+{}_s)\mu^{\pm}X$ decays. This doubly tagged decay gives us the opportunity to correctly attribute the decay to the RS sample. Like in the prompt tagged sample, we determine the yield by fitting the Δm distribution, which ensures a good soft pion tag. This allows us to determine if the muon tag is correct, *i.e.* a correct muon tag carries the opposite charge to the soft pion. [1]

The Right-Sign mistag probabilities can be defined as:

$$f_{MT} \equiv \mathbb{P}(\mu^+|D^0 \to K^-\pi^+) = \frac{N(D^{*+} \wedge \mu^+)}{N(D^{*+})}. \tag{8.2}$$

The offline selection of the doubly tagged sample combines the B reconstruction requirements of the semileptonic sample with the PID requirements of the soft pion used in the prompt selection (see chapter 6). In addition, we sample the doubly tagged RS sample to recreate the distribution of the semileptonic RS sample in the decay time, $m_{corr}(B)$ and both IP$\chi^2(B,\,\mu)$ variables. This ensures that these variables follow similar distributions as the semileptonic tagged sample that passed the material selection and thus, the results are applicable.

We perform a simultaneous fit to the Δm peak of the doubly tagged sample without restriction on the muon tag and the doubly tagged sample with a same sign muon tag, analogous to the procedure described in chapter 7 for the prompt tagged sample. The yield ratio gives us the mistag probability due to random muon association. In figure 8.9 we see the fit yielding a charge averaged mistag probability of:

$$f_{MT} = \mathbb{P}(\mu^+|D^0 \to K^-\pi^+) = (0.116 \pm 0.015)\%. \tag{8.3}$$

Since this method relies on soft pion tag and the semileptonic tag, the available sample size is much smaller than either the prompt or semileptonic tagged samples. Therefore, it is impossible to perform an independent measurement for the much rarer Wrong-Sign decay. However, due to the symmetry in the process, it is possible to assume that the Wrong-Sign sample will contain the same amount of random muon events as the Right-Sign sample in absolute numbers.

Since the random muon mistagging rate is on the same order of magnitude as the expected WS-to-RS ratios (around 0.5%), this leads to a significant bias in the observed ratio as:

[1] For this part of the analysis, only the samples corresponding to the years 2017 and 2018 can be used, as the same sign candidates were discarded in the 2016 selection.

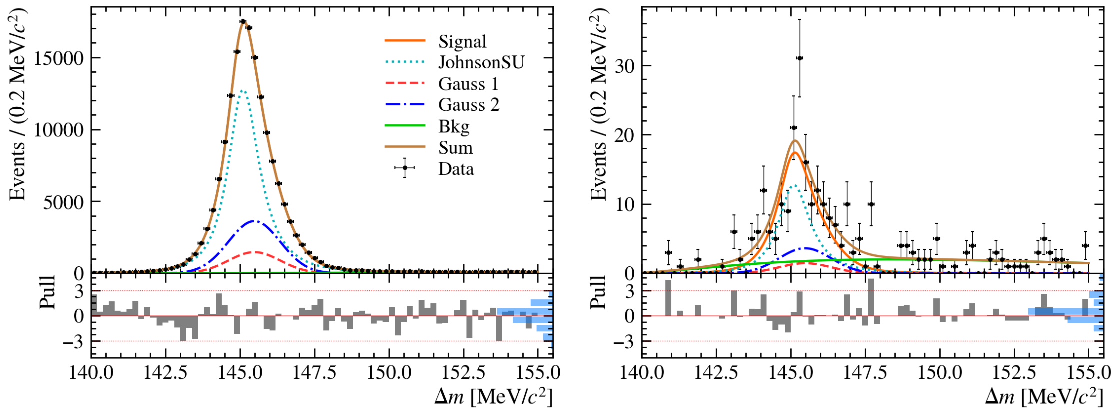

Figure 8.9: Simultaneous fit to Δm distributions of doubly tagged $D^{*+} \to K^-\pi^+$ decays, without restriction on the muon tag (left) and same sign muon tag (right).

$$\begin{aligned} R^{\text{obs}} &= \frac{N_{\text{WS}}^{\text{obs}}}{N_{\text{RS}}^{\text{obs}}} = \frac{N_{\text{WS}} + N_{\text{MT}}}{N_{\text{RS}} + N_{\text{MT}}} \approx \frac{N_{\text{WS}}}{N_{\text{RS}}} + N_{\text{MT}} \frac{N_{\text{RS}} - N_{\text{WS}}}{N_{\text{RS}}^2} + \mathcal{O}(N_{\text{MT}}^2) \\ &= R + f_{\text{MT}} \frac{N_{\text{RS}} - N_{\text{WS}}}{N_{\text{RS}}} + \mathcal{O}(f_{\text{MT}}^2) = R + f_{\text{MT}}(1 - R) + \mathcal{O}(f_{\text{MT}}^2) \end{aligned} \tag{8.4}$$

where the variables with the superscript $^{\text{obs}}$ are the values observed in the analysis and all variables without this superscript are the true values. The number of mistagged events per sample, $N_{\text{MT}} = f_{\text{MT}} N_{\text{RS}}$, is given as a fraction of the true number of RS decays, which is what we measure above.

The mistagging rate also leads to an increased uncertainty resulting from incorrect decay time on mistagged decays. The effect of this uncertainty will be investigated in chapter 10.

We also investigated a dependency of the mistag probability on D^0 decay time or the B flight distance. Although they do exist in general (for example, shown in [51]), we found that both effects are insignificant for the range accessible in this measurement.

9 Secondary D decays

9.1 Bias from secondary D decay contamination

Our sample of prompt tagged decays includes a background of secondary charm decays, *i.e.* charm mesons produced in b-hadron decays. These decays happen after some displacement, *i.e.* the flight distance of the b-hadron, and can thus introduce a bias in a time-dependent measurement since we calculate the decay time with respect to the primary vertex. This bias leads to larger reconstructed decay times since the primary vertex is further away than the real D^0 production (b-hadron decay) vertex. We follow the methodology used in previous analysis of this channel [8, 30, 52] to derive an upper bound of the effect. The observed ratio $R_{obs}(t)$ can be expressed in terms of the ratio of purely prompt produced decays $R(t)$ and a bias term $\Delta_B(t)$:

$$R_{obs}(t) = R(t)\left[1 - \Delta_B(t)\right]. \tag{9.1}$$

In turn, the bias term is constrained by

$$0 \leq \Delta_B(t) = f_B^{RS}(t)\left[1 - \frac{R_B(t)}{R(t)}\right] \leq f_B^{RS}(t)\left[1 - \frac{R_D}{R(t)}\right], \tag{9.2}$$

where f_B^{RS} is the fraction of secondary decays included in the prompt selected RS sample. $R_B(t)$ is the WS-to-RS ratio as a function of the properly reconstructed decay time for secondary decays. However, this proper decay time cannot be calculated reliably due to the bad vertex resolution of the $D^{*+} \to D^0\pi^+$ decay. In this vertex, both decay products are almost collinear, leading to a large uncertainty along the flight direction. Thus an upper limit can be imposed by assuming the worst case, *i.e.* t=0, such that $R_B(t = 0) = R_D$.

9.2 Size of secondary D contamination

To estimate the size of this effect, we calculate the fraction of secondary contamination f_B^{RS} in each individual decay time bin of our sample. In the selection process, we control the amount of secondary contamination by applying restrictions to the χ^2 of the D^0 and π_s impact parameters. The explicit requirement is

$$\mathrm{IP}\chi^2 \equiv \log(\mathrm{IP}\chi^2(D^0)) + 0.65 \cdot \log(\mathrm{IP}\chi^2(\pi_s)) < 3.5. \tag{9.3}$$

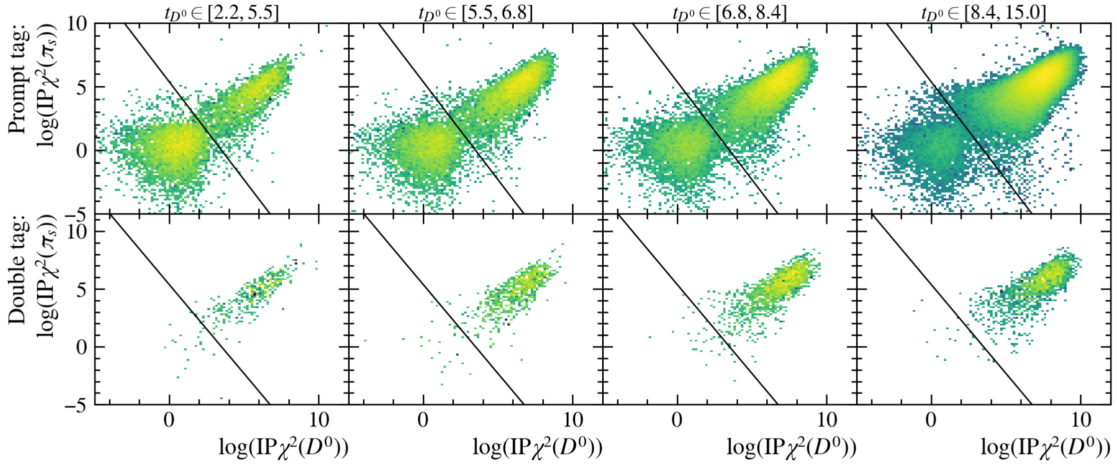

Figure 9.1: Distribution of the prompt (doubly) tagged samples is shown on the top (bottom) row. Columns show the different decay time bins under the prompt assumption. The black line indicates the requirment used to suppress secondary contamination, *i.e.* events in the bottom left pass the selection.

In the following, we will abbreviate this linear combination as IPχ^2. An illustration of these two parameters and the requirement is given in figure 9.1. Here we plot the distribution of the prompt (doubly) tagged sample in the top (bottom) row over the $(\log(IP\chi^2(D^0)), \log(IP\chi^2(\pi_s)))$-plane. The black line shows the IPχ^2 selection requirement, all events in the top right are vetoed. We include the doubly tagged sample as an example of secondary D^0 decays.

In addition, the displaced vertices also interact with the variable Δm, as calculated with the `DecayTreeFitter` algorithm that has requirements on both the D^0 mass and the primary vertex. A displaced vertex has a lower Δm value because the `DTF` forces the reconstructed D^0 to come from the primary vertex. For this analysis, these decays are removed with a `DTF` χ^2/ndf requirement. However, we still expect a tail contribution to the signal region. In figure 9.2, we show the distribution of the full, *i.e.* not time binned, RS sample in the (IPχ^2, Δm)-plane. In the top left, we see the peak corresponding to decays consistent with originating from a secondary vertex. At the bottom, we see the characteristic Δm signal peak. We determine the fraction of the secondary contamination to the signal peak by modelling the distributions and calculating the overlap of the background sample with the signal region.

In order to evaluate the size of this overlap, we use a sample of the RS prompt decays that follows the entire selection as seen in chapter 6, but does not enforce requirements on `DTF` χ^2/ndf or the requirement defined by equation 9.3.

We fit the distribution in IPχ^2 while restricting the Δm to a 3σ signal window. We adapt a methodology from the analysis presented in Ref. [53] and fit the prompt and secondary IPχ^2 distributions with a bifurcated Gaussian distribution f_{AGE}, which is modified to include exponential tails:

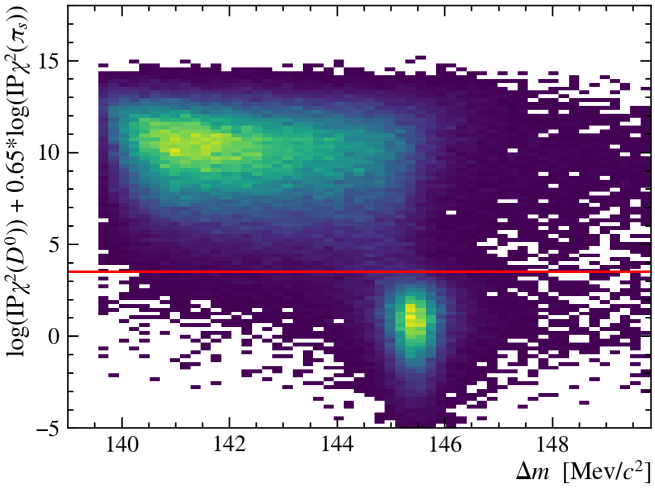

Figure 9.2: Distribution of the full RS sample in the IPχ^2 variable and Δm. The red line is the IPχ^2 selection requirement.

$$f_{\mathrm{AGE}}(x;\mu,\sigma,\epsilon,\rho_L,\rho_R) = \begin{cases} e^{\frac{\rho_L^2}{2}+\frac{\rho_L(x-\mu)}{\sigma(1-\epsilon)}} & \text{if } x<\mu-\rho_L\sigma(1-\epsilon), \\ e^{-\frac{(x-\mu)^2}{2\sigma^2(1-\epsilon)^2}} & \text{if } \mu-\rho_L\sigma(1-\epsilon)\le x<\mu, \\ e^{-\frac{(x-\mu)^2}{2\sigma^2(1+\epsilon)^2}} & \text{if } \mu\le x<\mu+\rho_R\sigma(1+\epsilon), \\ e^{\frac{\rho_R^2}{2}+\frac{\rho_R(x-\mu)}{\sigma(1+\epsilon)}} & \text{if } x\ge\mu+\rho_R\sigma(1+\epsilon). \end{cases} \tag{9.4}$$

The parameter μ is the mode of the distribution, σ is the average of both widths, ϵ models the asymmetry in widths and $\rho_{L/R}$ the exponential tails.

When measuring the contamination by secondary decays, we are very sensitive to variations in the upper tail parameter ρ_R of the signal distribution and the lower tail parameter of the background distribution ρ_L. It is not feasible to determine both parameters in the same fit since they end up being highly correlated and the fit is unstable.

A solution to this problem is to determine one of the parameters in an independent fit. The easiest way is to fit the background distribution in the lower Δm sideband. This assumes that the background shape is independent of the Δm variable. We can evaluate the uncertainty arising from this assumption by performing the measurement with the background shape taken from three independent Δm bins. These three background samples are defined by:

- $\Delta m \in [140.5, 141.5]\,\mathrm{MeV}/c^2$,
- $\Delta m \in [141.5, 142.5]\,\mathrm{MeV}/c^2$,
- $\Delta m \in [142.5, 143.5]\,\mathrm{MeV}/c^2$.

This is done for each of the decay time bins used in chapter 7. We then fix the shape parameters of the background shape, with the exception of the μ and σ parameters, to these values. In the next step, we fit both the signal and background in the signal region $\Delta m \in [144.7, 146.3]\,\mathrm{MeV}/c^2$. The fraction f_B^{RS} is determined with a numerical integral of both models in the range $x = \log(\mathrm{IP}\chi^2(D^0)) + 0.65 \cdot \log(\mathrm{IP}\chi^2(\pi_s)) < 3.5$, such that:

$$f_B^{RS} = \frac{\int_{-\infty}^{3.5} f_{\mathrm{AGE}}^{\mathrm{Background}}(x)\mathrm{d}x}{\int_{-\infty}^{3.5} f_{\mathrm{AGE}}^{\mathrm{Background}}(x) + f_{\mathrm{AGE}}^{\mathrm{Signal}}(x)\mathrm{d}x} \tag{9.5}$$

The fits to the signal region and the central background bin are shown in Appendix C.

The leading uncertainty on f_B^{RS} results from the fit uncertainty, not due to the choice of Δm sideband, as determined from the three different sideband bins. We report the combination of both in table 9.1 alongside the mean value.

One possible reason we could overestimate the contamination is clear when looking at figure 9.2. Specifically, the density of the background peak drops drastically within the Δm signal range. This could introduce a bias in the measurement.

Table 9.1: Fraction of secondary contamination in the RS prompt tagged sample.

Decay time bin [t/τ]	f_B^{RS} [%]
2.2 - 5.3	1.0 ± 0.19
5.3 - 6.6	1.4 ± 0.34
6.6 - 8.2	1.88 ± 0.23
8.2 - 15.0	1.31 ± 0.15
Time-integrated	1.32 ± 0.10

The effect of this contamination on the final result is accounted for using these values in chapter 10.

10 Results

10.1 Time-dependent fit

We fit the decay time dependence of the observed ratios (Tabs. 7.1 and 7.3) to determine the mixing parameters (R_D, y', x'^2). The fit minimises a χ^2 variable that includes terms to correct for biases of the observed ratios,

$$\chi^2 = \sum_{i=1}^{4} \left[\left(\frac{r_i^{SL} - \hat{R}_i^{SL}}{\sigma_i^{SL}} \right)^2 + \left(\frac{r_i^{PR} - \hat{R}_i^{PR}}{\sigma_i^{PR}} \right)^2 \right] + \chi^2_{p,\,PR} + \chi^2_{sec} + \chi^2_{MT}. \tag{10.1}$$

The measured WS-to-RS yield ratio in the i bin and the respective statistical uncertainty is denoted by r_i and σ_i for the prompt and semileptonic sample. The predicted value for the WS-to-RS ratios $\hat{R}_i$ is based on the time-integral over the i-th bin of eq. 4.1 and some correction for different sources of bias:

$$\begin{aligned}
\hat{R}_i^{SL} &= R_i^{SL} + f_{MT}(1 - R_i^{SL}), \\
\hat{R}_i^{PR} &= R_i^{PR}(1 - \Delta_i) + p_i^{PR}, \\
\Delta_i &= b_i \left(1 - \frac{R_D}{R_i^{PR}} \right), \\
R_i^{PR,\,SL} &= R_D + \sqrt{R_D} y' \langle t \rangle_i^{PR,\,SL} + \frac{y'^2 + x'^2}{4} \langle t^2 \rangle_i^{PR,\,SL}.
\end{aligned} \tag{10.2}$$

The term Δ_i accounts for biases due to the contamination of the prompt sample by secondary D decays, the contamination of the prompt sample with peaking backgrounds is accounted for by the term p_i^{PR} and f^{MT} accounts for the mistagging in the semileptonic tagged sample.

The parameters associated with these terms can be varied independently as part of the fit, facilitated by their respective χ^2 terms:

$$\begin{aligned}
\chi^2_{p,\,PR} &= \sum_{i=1}^{4} \left(\frac{p_i^{PR} - P_i^{PR}}{\sigma_i(P^{PR})} \right)^2, \\
\chi^2_{sec} &= \sum_{i=1}^{4} \left(\frac{b_i - B_i}{\sigma_i(B)} \right)^2, \\
\chi^2_{MT} &= \sum_{i=1}^{4} \left(\frac{f_i^{MT} - F_i^{MT}}{\sigma_i(F^{MT})} \right)^2.
\end{aligned} \tag{10.3}$$

The capitalised variables are the mean values we determine in this analysis and the lowercase variables as those that can vary within a Gaussian constraint based on the uncertainty of the measurement. P_i^{PR} are based on the results reported at the end of section 8.1. There we only performed a time-integrated measurement of the peaking background. We assume this to be distributed uniformly over the decay time bins. The secondary decay fractions B_i were reported in table 9.1 and the mistagging fractions F_i^{MT} for the semileptonic sample are based on the measurement of the mistagging rate reported in table 8.3.

10.1.1 Evaluation of the fitting tool

This fitting method is an extension of a model used in previous studies [52], where it was shown that their fit returns unbiased estimates of the mixing parameters and uncertainties. We perform our own test of the fitter based on 10^4 pseudo experiments, where the ratios are generated based on the world-average mixing parameters and the effects of the nuisance parameters for secondary decays, peaking prompt background and the random muon tags are included. We calculate the mean mixing parameters and their asymmetric uncertainty intervals. The distributions of the fitter results based on these experiments are given in figure 10.1, plotting the pulls to the world-average charm mixing parameters. The results of these pseudo-experiments indicate that the fitter has a small bias and that the confidence intervals returned by the fitter are asymptotically correct.

10.1.2 Result

The results of the fit and the relevant correlations are reported in table 10.1. They generally agree with the world-average values as seen in Ref. [19] but have large uncertainties. In the next subsection, we explain how the systematic uncertainties are determined. The large correlations are also in line with those previously observed [30]. A visualisation of the χ^2 fit is given in figure 10.2. There we show the observed WS-to-RS ratios and the expected ratios $\hat{R}_i$ based on the fitted charm mixing parameters and the corrections outlined in the definition of the χ^2. We also show the $R(t)$ plots based on the fitted and world-average charm mixing parameters. The χ^2 value of 1.2 for five degrees of freedom is rather low, corresponding to a p-value of 0.10. This is a plausible value and does not necessarily indicate a problem with the fit.

10.1.3 Systematic uncertainties

As explained above, systematic uncertainties arising from the contamination of the prompt sample with secondary D decays and peaking background contributions to both samples are included via nuisance parameters in the time-dependent fit. We can decouple these uncertainties by performing the fit again, but with the nuisance parameters fixed to the nominal values and subtracting the uncertainties in quadrature. To determine the systematic uncertainty resulting from the secondary

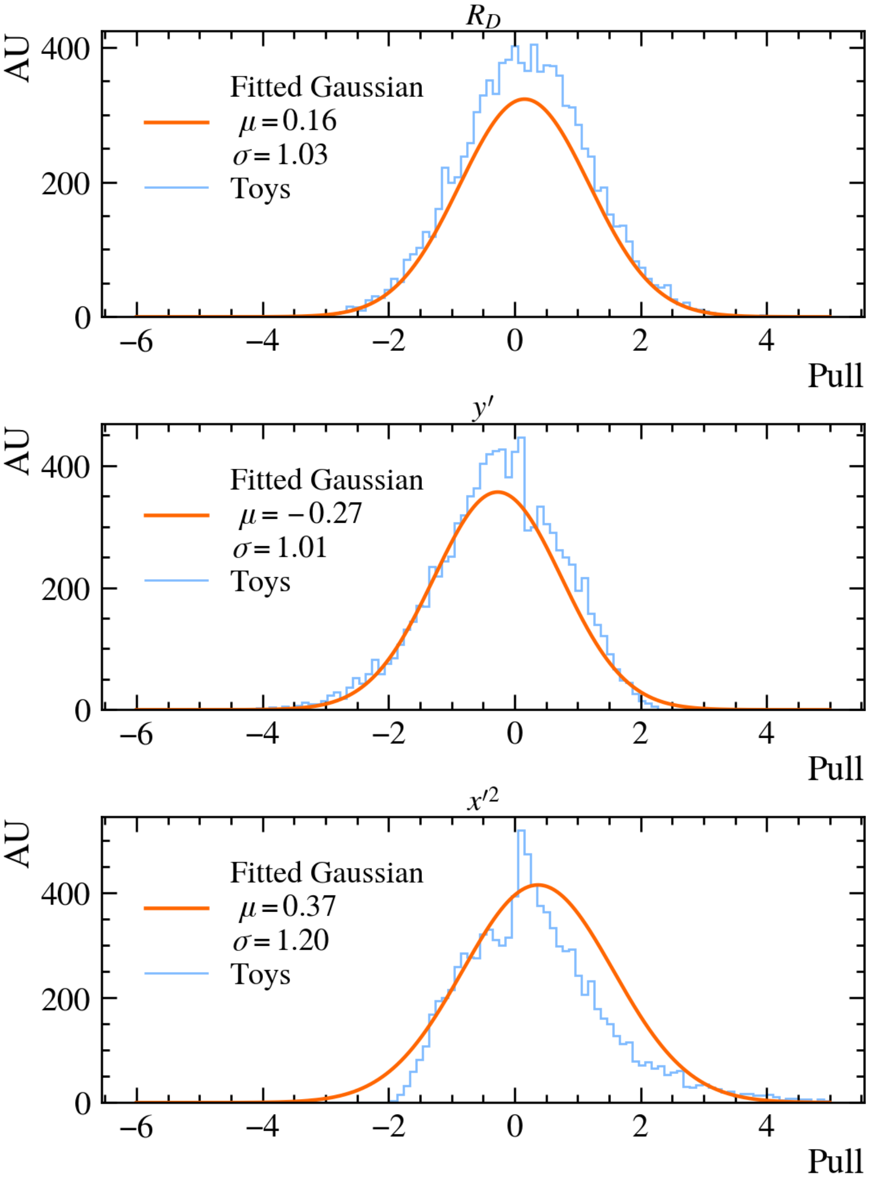

Figure 10.1: Distribution of the estimated mixing parameters pulls based on the pseudo experiments.

Table 10.1: Results of the time-dependent χ^2 fit to determine the mixing parameters. The first uncertainty given is statistical and the second systematic.

	Parameters	Correlations		
	$[10^{-3}]$	R_D	y'	x'^2
R_D	$3.5 \pm 0.8 \pm 0.2$	1.00	−0.91	0.83
y'	$6\ ^{+8}_{-10}\ ^{+2}_{-4}$		1.00	−0.98
x'^2	$0.0\ ^{+0.4}_{-0.2}\ ^{+0.2}_{-0.1}$			1.00
χ^2/ndof		1.19/5		

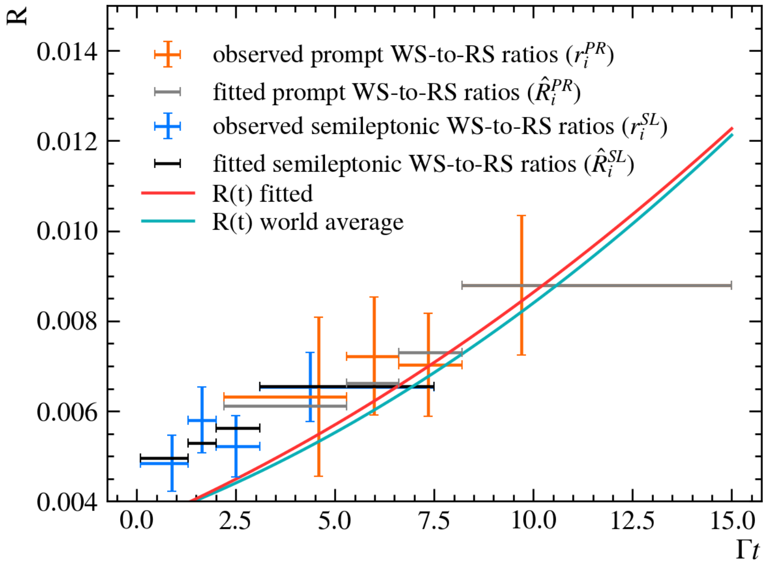

Figure 10.2: The observed WS-to-RS ratios of the semileptonic (blue) and prompt (orange) samples are shown. The mixing parameters are determined based on these, yielding the red $R(t)$ plot. The $R(t)$ plot based on the World-average charm mixing values is included in turquoise as a point of comparison. We also show the predicted base WS-to-RS ratios in grey and black, *i.e.* $\hat{R}_i$.

Table 10.2: Results of simulated experiments to determine the systematic uncertainties. The results are averaged over 1000 simulated experiments. The individual systematic uncertainties are obtained by subtraction in quadrature of the uncertainty of a fit, where the effect is neglected or fixed from a fit, where it is included as a constrained parameter.

Source	$\Delta \pm \sqrt{\Delta\sigma^2}$		
	$R_D[10^{-3}]$	$y'[10^{-3}]$	$x'^2[10^{-3}]$
Secondary D decays	$0.019^{+0.087}_{-0.091}$	$-0.355^{+1.097}_{-0.785}$	$0.018^{+0.035}_{-0.070}$
Prompt peaking background	$0.000^{+0.062}_{-0.062}$	$-0.001^{+0.985}_{-0.735}$	$0.000^{+0.023}_{-0.047}$
Random muon background	$-0.004^{+0.320}_{-0.322}$	$0.074^{+3.466}_{-2.289}$	$-0.004^{+0.057}_{-0.148}$
Decay time smearing from random muon background	$0.000^{+0.019}_{-0.019}$	$0.000^{+0.236}_{-0.159}$	$0.000^{+0.005}_{-0.012}$
Choice of signal shape	$0.000^{+0.074}_{-0.074}$	$0.001^{+0.993}_{-0.779}$	$0.000^{+0.023}_{-0.036}$
Total syst. uncertainty	${}^{+0.346}_{-0.349}$	${}^{+3.902}_{-2.651}$	${}^{+0.075}_{-0.174}$
Statistical uncertainty	${}^{+0.747}_{-0.748}$	${}^{+8.392}_{-6.782}$	${}^{+0.187}_{-0.329}$

contamination, we set the fraction of secondary decays to zero instead. We consider additional sources of systematic uncertainty in the following.

Any charge-dependent asymmetry in the samples is expected to cancel out in this flavour-averaged measurement.

The decay time resolution can be influenced by several factors, the absolute length scale of LHCb, the world-average value of the D^0 mass and the LHCb momentum resolution. The first two effects have been measured to not significantly bias the measurement of (y', x'^2) in previous analysis [30] and are thus negligible for his analysis. The latter is not relevant due to the large size of our decay time bins, such that bin swapping is not a relevant problem.

The semileptonic mistagging via random muon combination also leads to an incorrect decay time. We can model this effect by smearing the decay time of these decays with $\sigma = \tau$. We evaluate the effect with pseudo experiments.

The systematic uncertainty of the model choice on the observed WS-to-RS ratios is measured in chapter 7. We propagate these uncertainties to the charm mixing parameters with the help of pseudo experiments. We adjust the measurement of the ratios according to the results obtain in figures 7.2 and 7.4. Since we already include ratios determined with two different models in the time-dependent fit, a model choice uncertainty is already included in their uncertainty. We obtain the systematic uncertainties of the model choice by subtracting the uncertainties in quadrature.

As can be seen from the uncertainties listed in table 10.2 the uncertainties are expected to be mostly statistical in origin. We also see that any biases (Δ in tab. 10.2) associated with the individual uncertainties are small compared to their respective uncertainties.

Table 10.3: Results of the systematic uncertainties studies on the observed WS-to-RS ratios, *i.e.* the real measurement. The individual systematic uncertainties are obtained by subtraction in quadrature of the uncertainty of a fit, where the effect is neglected or fixed from a fit, where it is included as a constrained parameter.

Source	$\Delta \pm \sqrt{\Delta\sigma^2}$		
	$R_D[10^{-3}]$	$y'[10^{-3}]$	$x'^2[10^{-3}]$
Secondary D decays	$0.000^{+0.090}_{-0.078}$	$-0.042^{+0.828}_{-1.270}$	$0.005^{+0.049}_{-0.013}$
Prompt peaking background	$0.001^{+0.046}_{-0.018}$	$-0.019^{+0.280}_{-0.636}$	$0.001^{+0.026}_{-0.002}$
Random muon background	$0.000^{+0.180}_{-0.167}$	$-0.022^{+1.257}_{-2.091}$	$0.001^{+0.090}_{-0.078}$
Choice of signal shape	$0.072^{+0.033}_{-0.030}$	$-1.235^{+1.829}_{-2.579}$	$0.046^{+0.180}_{-0.100}$
Total syst. uncertainty	${}^{+0.209}_{-0.188}$	${}^{+2.385}_{-3.612}$	${}^{+0.211}_{-0.106}$
Statistical uncertainty	${}^{+0.830}_{-0.831}$	${}^{+7.750}_{-9.704}$	${}^{+0.385}_{-0.220}$

We also perform the same study to determine the systematic uncertainties with the real results. This does not include the systematic effect from decay time smearing from random muon background since this study is not easily implemented without pseudo-experiments and they show the effect to be small. The results are summarised in table 10.3. These uncertainties are the basis of those reported in table 10.1.

When comparing the systematic uncertainties as determined from the observed WS-to-RS ratios with those determined from pseudo-experiments, we see that both broadly agreea further sign for the validity of the fit.

10.2 Time-integrated Wrong-Sign to Right-Sign ratio

In a second measurement, we compare the time-integrated WS-to-RS ratios of both the prompt and semileptonic tagged sample to their predicted values based on the world average charm-mixing parameters [19] without any terms accounting for material interactions. The calculation of the probability distributions (blue in figure 10.3) include the same corrections for systematic effects explained for the time-dependent fit above (see 10.1). We also include the statistical uncertainty as determined in chapter 7. This allows us to perform a hypothesis test of the Null-hypothesis, *i.e.* the RF-foils material has no effect on the mixing of D^0 mesons. In figure 10.3 we show the obverse ratio for both samples with reference to the probability distribution of the Null-hypothesis. Based on these values we cannot reject the Null-hypothesis[1].

In figure 10.3 we also decompose the width of the probability distributions into a statistical and systematic part. The size of the systematic uncertainty is determined by subtracting the statistical uncertainty as determined in chapter 7 from the total uncertainty. We see that the statistical uncertainty is still the dominant source of

[1]Rejection at 5 (3) σ happens for p-values smaller than $2.86 \cdot 10^{-7}$ ($1.35 \cdot 10^{-3}$).

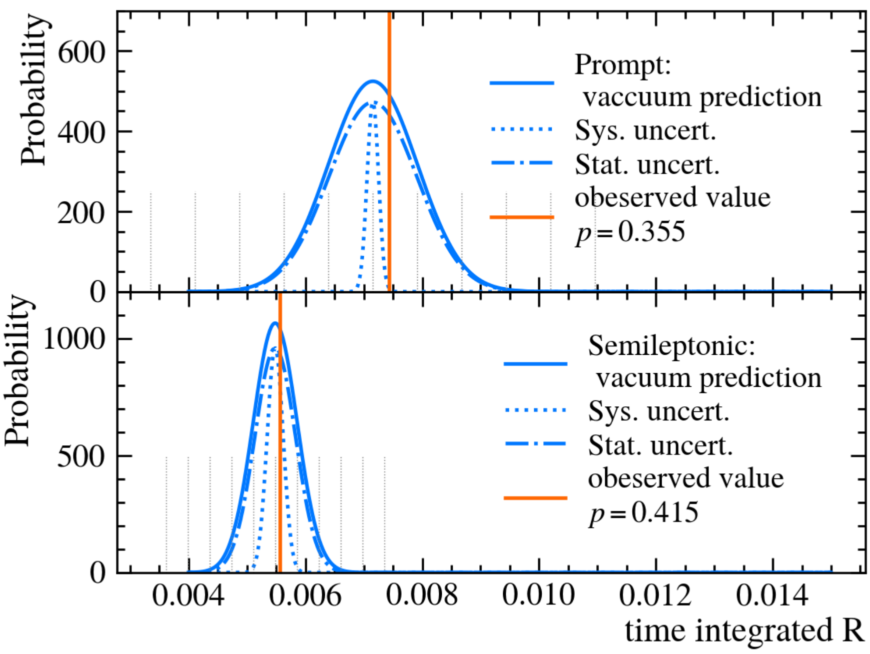

Figure 10.3: The blue line shows the probability distribution of the time-integrated R measurement under the assumption of propagation in vacuum for the prompt (semileptonic) tagged sample on top (bottom). The systematic and statistical components of this probability distributions are also indicated. The orange lines indicate the observed values of R and the grey dotted lines indicate the integer σ intervals of the distribution.

uncertainty.

Table 10.4: Results of the Null-hypothesis test.

Tag type	**p-value**
Prompt	0.352
Semileptonic	0.415

11 Conclusion

This thesis presents the first measurement of the neutral charm meson mixing parameters with D^0 mesons that have passed through material. Using the LHCb Run 2 data set (5.6 fb^{-1}) from prompt $D^{*+} \to D^0\pi^+$ and semileptonic $B^- \to D^0\mu^- X$ decays, we measure the charm mixing parameters to be:

$$
\begin{aligned}
R_D &= (3.5 \quad \pm 0.8 \quad \pm 0.2 \quad)\cdot 10^{-3},\\
y' &= (6 \quad {}^{+8}_{-10} \quad {}^{+2}_{-4} \quad)\cdot 10^{-3},\\
x'^2 &= (0.0 \quad {}^{+0.4}_{-0.2} \quad {}^{+0.2}_{-0.1} \quad)\cdot 10^{-3},
\end{aligned}
$$

where the first uncertainty is statistical and the second systematic. This measurement has large uncertainties, compared to measurements at LHCb using only D^0 mesons decaying in the primary vacuum [30], and does not show any significant deviations from the world-average neutral charm mixing parameters [19].

For these measurements, new models of the RF-foils of the VELO detector are created. A combined time-dependent fit of two differently tagged D^0 samples is used, which allows for the coverage of a wide spectrum of decay times and cross-validates the measurement.

In a further time-integrated measurement, we separate the two tagging methods and perform a test of the hypothesis that no mixing in excess of the vacuum-mixing is seen. For neither sample, any effect beyond the D^0- $\overline{D}^0$ mixing in vacuum is observed.

The uncertainty of this measurement is dominated by statistical uncertainty. The analysis tools used in this thesis could be used in LHCb Run 3 and beyond. The analysis would expect a large reduction in statistical uncertainty due to the improved charm trigger strategy, increased luminosity and the new VELO detector bringing material even closer to the interaction point. Larger data sets would also enable future analyses to perform tag and flavour-specific determinations of the neutral charm mixing parameters. Flavour-specific measurements are especially promising to detect the effect of material interactions on D^0- $\overline{D}^0$ mixing.

A Appendix: Theory of material mixing

In this Appendix, we propose an extension of the mixing theory to include an effect of material interaction. We also run some pseudo-experiments based on this theory to predict the signature of material interactions on our measurement.

A.1 Effect of material interactions on mixing

The addition of material interactions to the vacuum propagation of a flavoured neutral meson results in a phenomenon that has historically been called regeneration. The phenomenon was first predicted and an experiment was proposed by A. Pais and O. Piccionio [3]. Their proposed experimental setup is depicted in figure A.1. In this setup, a pure beam of K_L is directed through some medium, upon exiting the material the K beam has regenerated a K_S component. This predicted effect was first used to measure the mass difference in the Kaon system by H. Good *et al.* [4].

Regeneration results from the interaction of the particle with baryonic matter, which is fundamentally CP asymmetric. This means that the interaction cross section is different for P^0 and $\overline{P}^0$, *i.e.* the meson with heavy flavour valence quark, s for the $\overline{K}^0$ and c for D^0, can combine with the valence quarks of protons and neutrons to produce flavoured baryons, *e.g.*Σ or Λ for $\overline{K}^0$. The same cannot be said for their partner as they contain the respective anti-quark, but ordinary matter lacks the necessary valence anti-quarks to form anti-baryons. Kaons proved to be very suitable to observe the effect due to the large difference in decay times between both physical states. This enables experimenters to produce a pure K^0_{L} beam, to be shot on a target. In addition, the neutral Kaon has CP specific decay channels that simplify the analysis as mass and CP eigenstates are almost identical. The starting position for the D^0 system is different as the meson will not evolve far from the initial flavour-eigenstate due to the small mixing effect.

We try to amend the treatment of mixing in chapter 2.5 by an additional term in the effective Hamiltonian to account for the material effect. For the treatment of kaons, a diagonal addition to the effective Hamiltonian in the flavour space was proposed [54]. We try to apply the same principle to the charm sector.

We will use the CP limit as discussed in table 2.2 and equations 2.32 to get a simplified amended effective Hamiltonian

$$\mathscr{H} = \begin{pmatrix} M - \frac{i}{2}\Gamma & \frac{\Delta M}{2} - \frac{i}{2}\frac{\Delta\Gamma}{2} \\ \frac{\Delta M}{2} - \frac{i}{2}\frac{\Delta\Gamma}{2} & M - \frac{i}{2}\Gamma \end{pmatrix} + \begin{pmatrix} F' & \\ & \bar{F} \end{pmatrix}. \tag{A.1}$$

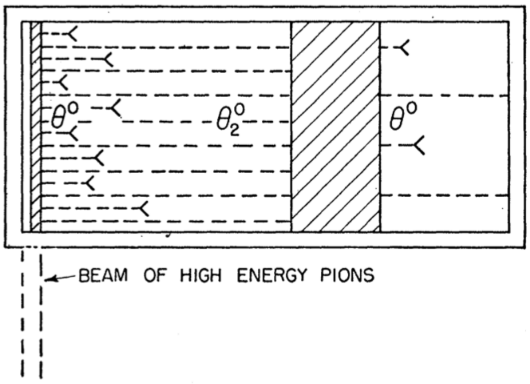

Figure A.1: Figure used to explain the regeneration effect in kaons, taken from [3]. The outdated notation θ is used for kaons and θ_2^0 for K^0_{L}. The V-shaped vertices indicate decays to two pions associated with K^0_{S} decays. A pure K^0_{L} beam enters the target and decays, which are specific to K^0_{S}, can be found after the target.

For the charm system, we assume $F' > \bar{F}$ since the system with a positive charm number should experience a larger potential in material as

$$\sigma_M(D^0 N) > \sigma_M(\overline{D}^0 N). \tag{A.2}$$

In the next step, we decompose F', $\bar{F}$ into a mean and differences:

$$F = \frac{F' + \bar{F}}{2}, \qquad \Delta F = F' - \bar{F}. \tag{A.3}$$

Since the physical meaning of the terms in $\mathscr{H}$ becomes much clearer in the CP limit, we can perform some additional simplifications. The real part $\mathcal{R}e(F)$ can be dropped since it leads to an overall phase in the time evolution, which has no physical effect. So can the imaginary part $\mathcal{I}m(F)$, as it leads to a total increase in the decay rate, which is physically meaningful but ultimately disappears in our measurement since we only select particles that decay in vacuum. So we can drop the F term and remain with

$$\mathscr{H} = \begin{pmatrix} M - \frac{i}{2}\Gamma & \frac{\Delta M}{2} - \frac{i}{2}\frac{\Delta\Gamma}{2} \\ \frac{\Delta M}{2} - \frac{i}{2}\frac{\Delta\Gamma}{2} & M - \frac{i}{2}\Gamma \end{pmatrix} + \begin{pmatrix} \Delta F & \\ & -\Delta F \end{pmatrix}. \tag{A.4}$$

Following the vacuum case, we calculate eigenvectors and eigenvalues:

$$
\begin{aligned}
\lambda_1 &= \frac{1}{4}\left(4M - 2i\Gamma + \sqrt{(2\Delta M - i\Delta\Gamma)^2 + 16\Delta F^2}\right), \\
\lambda_1 &= \frac{1}{4}\left(4M - 2i\Gamma - \sqrt{(2\Delta M - i\Delta\Gamma)^2 + 16\Delta F^2}\right), \\
v_1 &= \begin{pmatrix} 4\Delta F + \sqrt{16\Delta F^2 + (2\Delta M - i\Delta\Gamma)^2} \\ 2\Delta M - i\Delta\Gamma \end{pmatrix}, \\
v_1 &= \begin{pmatrix} 4\Delta F - \sqrt{16\Delta F^2 + (2\Delta M - i\Delta\Gamma)^2} \\ 2\Delta M - i\Delta\Gamma \end{pmatrix}.
\end{aligned} \tag{A.5}
$$

We see that the limit $\Delta F \to 0$ recovers the results of no mixing in the CP limit. For better interpretability, we can substitute dimensionless parameters:

$$
\begin{aligned}
\lambda_1 &= \frac{M}{\Gamma} - \frac{i}{2} + \frac{1}{2}\sqrt{(x - iy)^2 + 4f^2}, \\
\lambda_2 &= \frac{M}{\Gamma} - \frac{i}{2} - \frac{1}{2}\sqrt{(x - iy)^2 + 4f^2}, \\
v_1 &= \begin{pmatrix} 2f + \sqrt{(x - iy)^2 + 4f^2} \\ x - iy \end{pmatrix}, \\
v_2 &= \begin{pmatrix} 2f - \sqrt{(x - iy)^2 + 4f^2} \\ x - iy \end{pmatrix},
\end{aligned} \tag{A.6}
$$

where we introduced the additional dimensionless parameter $f = \frac{\Delta F}{\Gamma}$. We see that the mass eigenstates that were orthogonal from the *CP* conserving limit are now again non-orthogonal due to the material effect. We can again diagonalise $\mathscr{H}$ to perform the time evolution

$$
\Sigma(t) = \mathbf{S} \begin{pmatrix} e^{-i\lambda_1 t} & 0 \\ 0 & e^{-i\lambda_2 t} \end{pmatrix} \mathbf{S}^{-1} \qquad \text{with } \mathbf{S} = (v_1, v_2). \tag{A.7}
$$

Calculating a value for f from first principles is beyond the scope of this thesis, but we can infer some of the properties it should have. From the optical theorem, we know that the cross section for forward scattering is given by:

$$
\sigma_T = \mathcal{I}m\tilde{f}(0)\frac{4\pi}{k}, \tag{A.8}
$$

where $\tilde{f}$ is the scattering amplitude. Thus the cross section and f should have an inverse momentum dependence. In addition, the material effect should depend on the amount of nucleons in the flight path of the meson:

$$f \sim \frac{\text{flight distance in material}}{momentum} \tag{A.9}$$

This assumes a constant nuclear density of the target material. In the following section, we present simulations of the effect on the measurement for different values of f.

A.2 Signature of material effects on charm mixing

Based on the model explained in section A.1, we perform simulations of potential signatures of the effect material has on charm mixing.

First, we investigate the effect of the amended effective Hamiltonian on the mixing probability on the level of an individual meson. In figure A.2, we plot the time development of the $D^0 \rightleftarrows \overline{D}^0$ transition probabilities. However, for the decay times indicated by the blue shaded background, we exchanged the effective Hamiltonian for vacuum with one, including a material effect of size $|f| = 0.005$. We see there that the effect is asymmetric with respect to the initial flavour state and highly dependent on the phase of f.

Since the effect is flavour asymmetric, it is not immediately obvious what the implication for our measurement would be. We simulate time- and flavour-integrated measurements using the real momentum, decay time, tag and flight path data used for the actual measurement. We are calculating the alternative hypothesis to the Null-hypothesis used in chapter 10.2.

We also introduce a momentum dependence into $f = \frac{df_0}{p}$, where d is the flight distance in RF-foil material and p the momentum in MeV/c. We run 1000 pseudo-experiments for four different values of $|f_0|$ and see in figure A.3 that for each of these time and flavour integrated measurements, we would expect an enhancement of the WS-to-RS ratio irrespective of the phase of f_0 and the flavour-averaging. Here the size of f_0 was purely chosen to produce a visible effect.

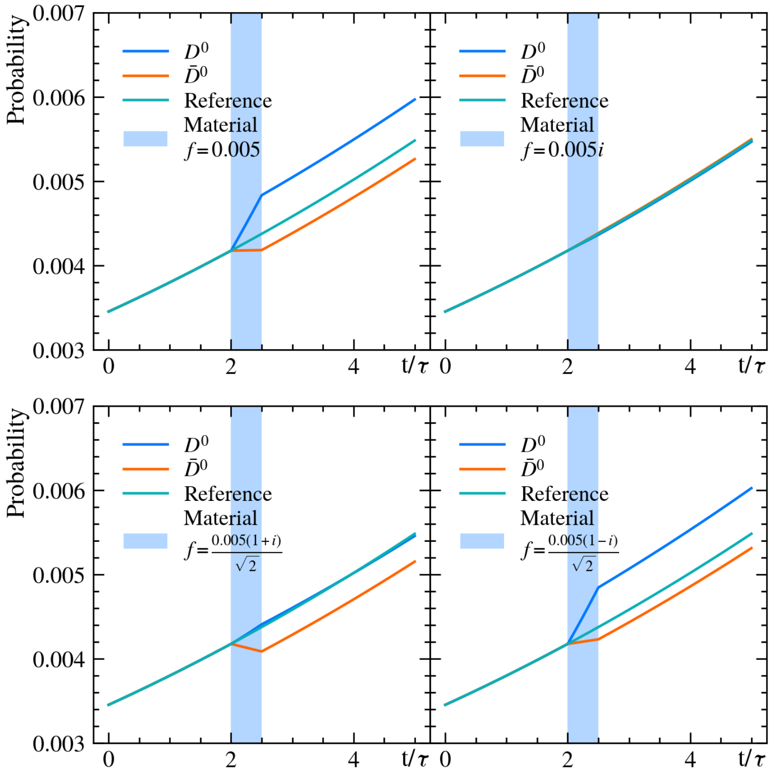

Figure A.2: We show the effect of the material effective Hamiltonian on the expected $D^0 \rightleftarrows \overline{D}^0$ transition probabilities. We transition from the vacuum effective Hamiltonian to the material effective Hamiltonian for decay time indicated with a blue-shaded background. The effects are split for initial D^0 and $\overline{D}^0$ states. Here shown is $|f| = 0.005$ with four different phases. The included reference line indicated the development without any material effect, *i.e.* $f = 0$.

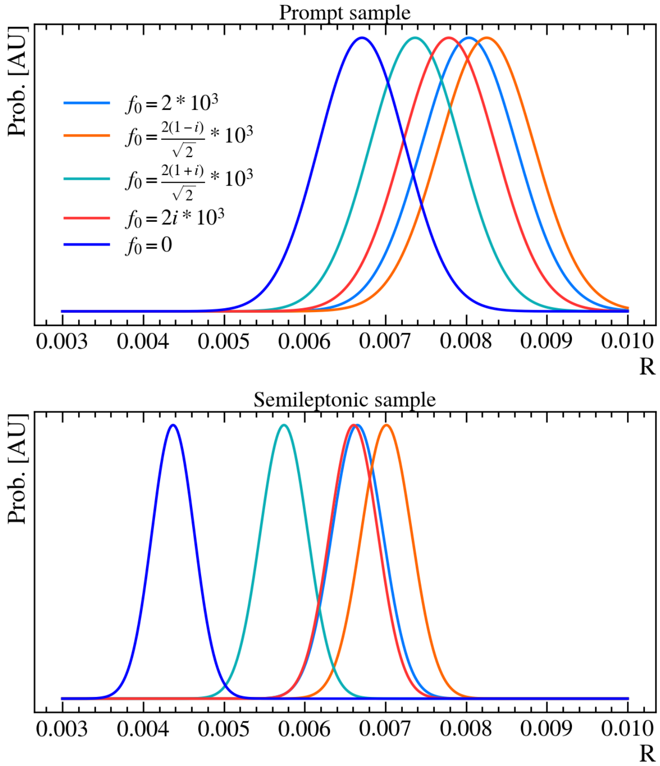

Figure A.3: Simulated Effect of material interaction in the foil on the time and flavour integrated measurement, parameters are based on the real samples, the calculation is based on several phase configurations of f_0. The absolute size of f_0 is chosen purely to create a visible effect.

B Appendix: Determination of WS-to-RS ratios

Here we show the Δm distributions of the RS and WS prompt samples in the different decay time bins and overlay the result of the simultaneous fits used to determine the WS-to-RS ratios.

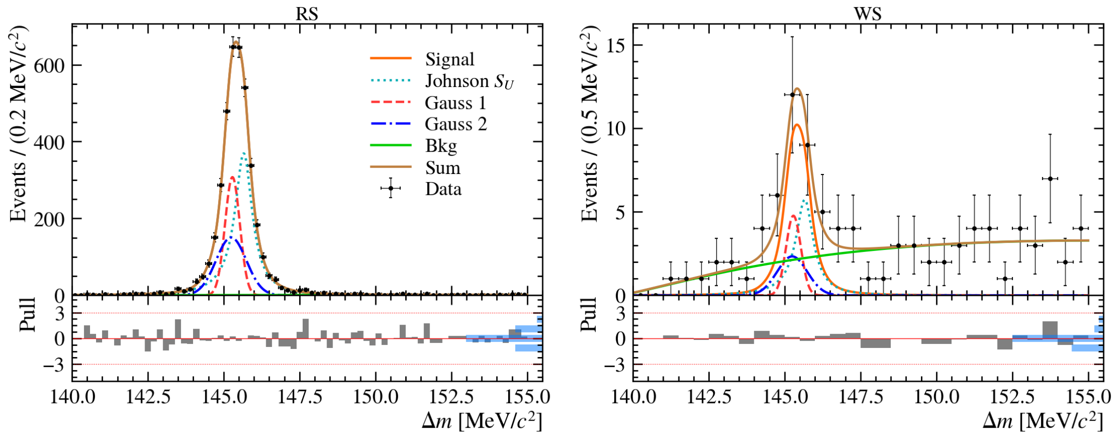

Figure B.1: The Δm distributions of the RS and WS prompt tagged samples in the first decay time bin $\Gamma t \in [2.2, 5.3]$ are shown. The result of the simultaneous fit are overlaid. The pulls of the fit are shown in the bottom part.

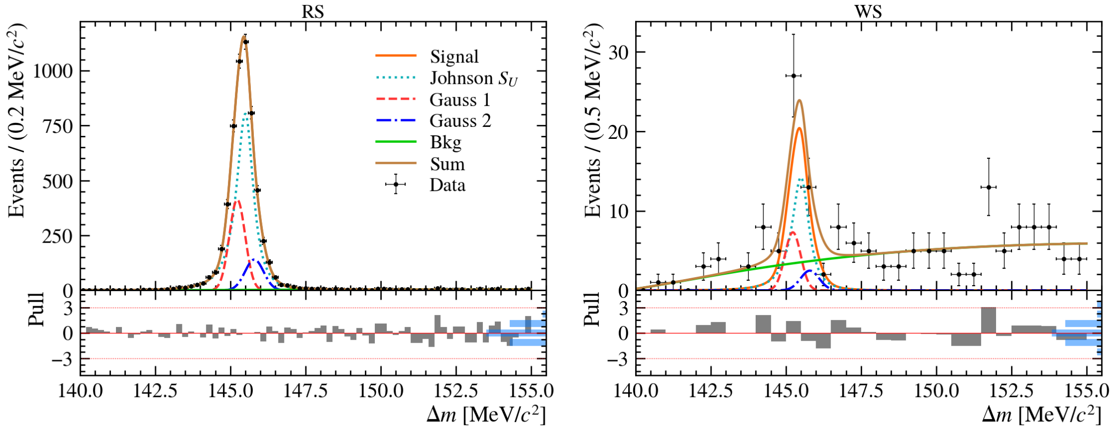

Figure B.2: The Δm distributions of the RS and WS prompt tagged samples in the second decay time bin $\Gamma t \in [5.3, 6.6]$ are shown. The result of the simultaneous fit are overlaid. The pulls of the fit are shown in the bottom part.

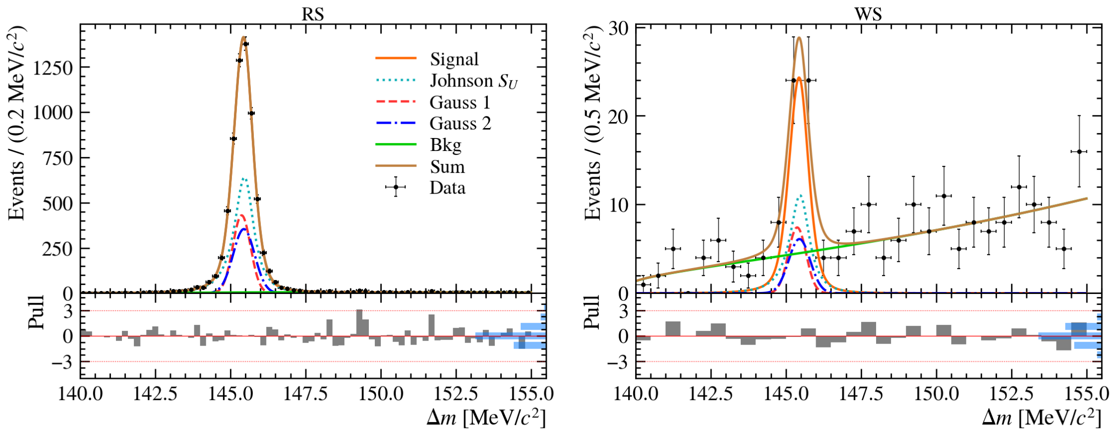

Figure B.3: The Δm distributions of the RS and WS prompt tagged samples in the third decay time bin $\Gamma t \in [6.6, 8.2]$ are shown. The result of the simultaneous fit are overlaid. The pulls of the fit are shown in the bottom part.

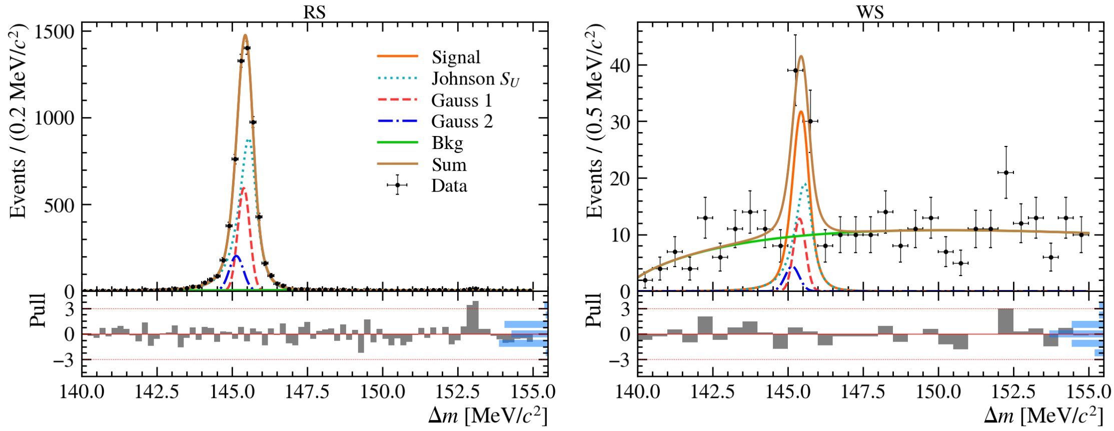

Figure B.4: The Δm distributions of the RS and WS prompt tagged samples in the fourth decay time bin $\Gamma t \in [8.2, 15]$ are shown. The result of the simultaneous fit are overlaid. The pulls of the fit are shown in the bottom part.

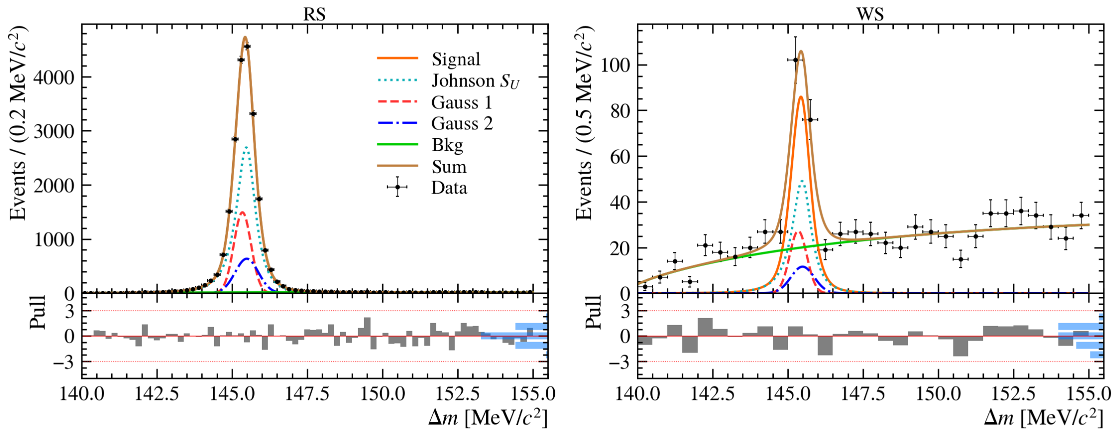

Figure B.5: The Δm distributions of the RS and WS prompt tagged samples in the decay time integrated measurement $\Gamma t \in [2.2, 15]$ are shown. The result of the simultaneous fit are overlaid. The pulls of the fit are shown in the bottom part.

Here we show the $m(D^0)$ distributions of the RS and WS semileptonic tagged samples in the different decay time bins and overlay the result of the simultaneous fits used to determine the WS-to-RS ratios.

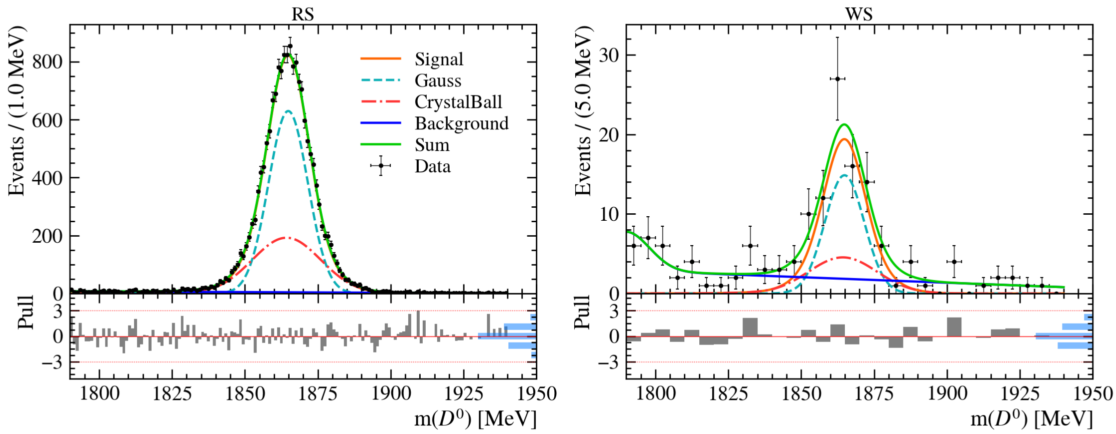

Figure B.6: The Δm distributions of the RS and WS semileptonic tagged samples in the first decay time bin $\Gamma t \in [0.1, 1.3]$ are shown. The result of the simultaneous fit are overlaid. The pulls of the fit are shown in the bottom part.

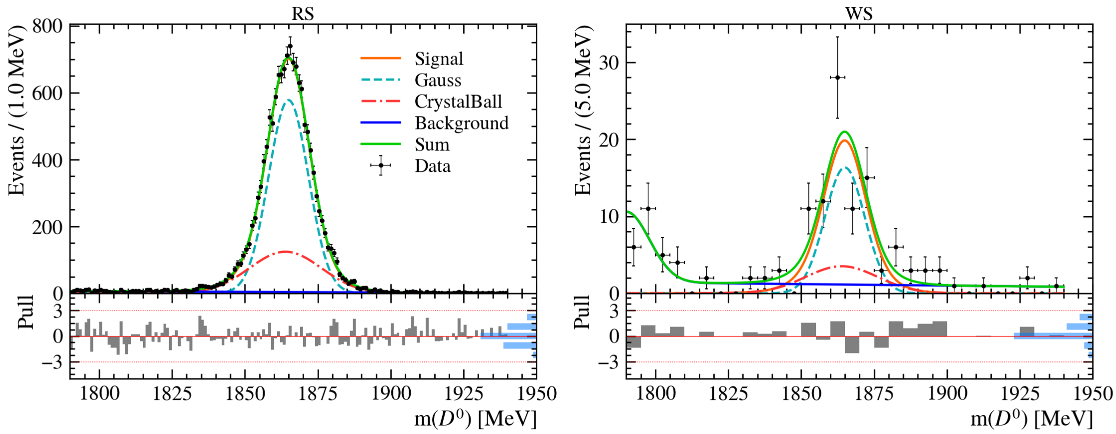

Figure B.7: The Δm distributions of the RS and WS semileptonic tagged samples in the second decay time bin $\Gamma t \in [1.3, 2.0]$ are shown. The result of the simultaneous fit are overlaid. The pulls of the fit are shown in the bottom part.

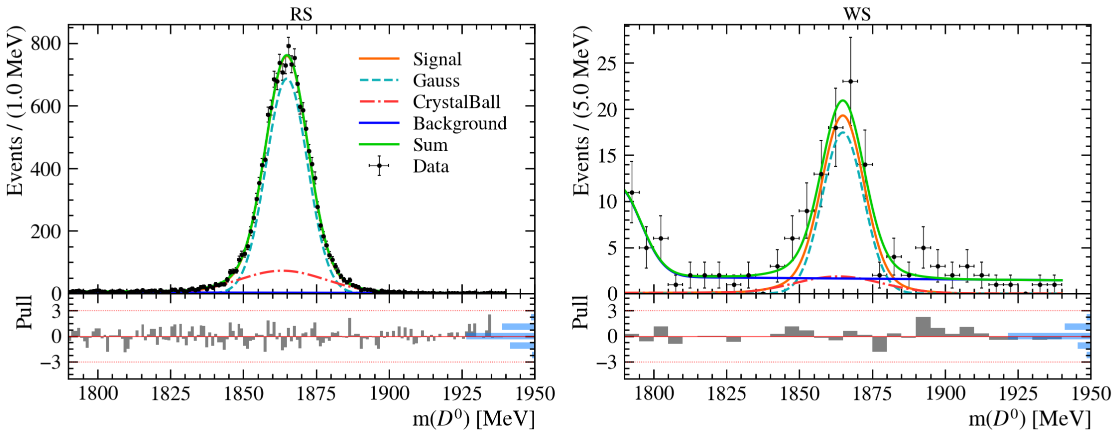

Figure B.8: The Δm distributions of the RS and WS semileptonic tagged samples in the third decay time bin $\Gamma t \in [2.0, 3.1]$ are shown. The result of the simultaneous fit are overlaid. The pulls of the fit are shown in the bottom part.

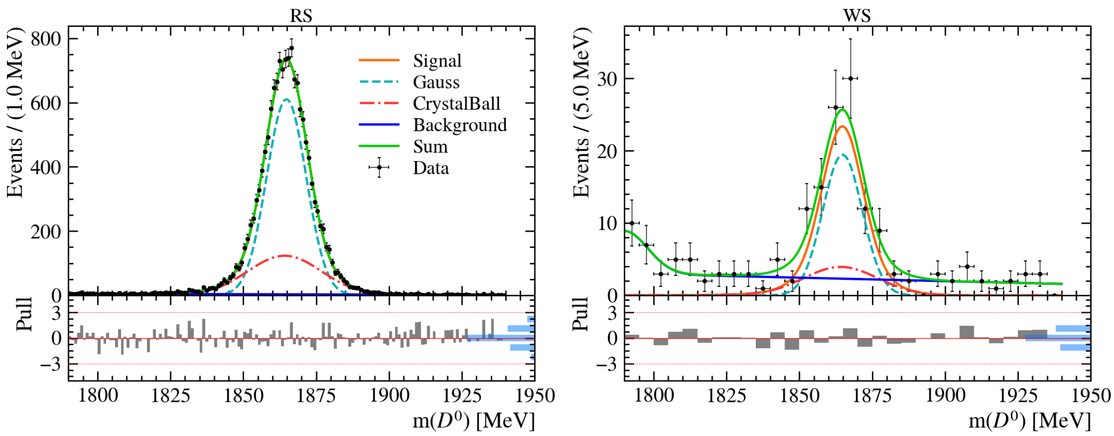

Figure B.9: The Δm distributions of the RS and WS semileptonic tagged samples in the fourth decay time bin $\Gamma t \in [3.1, 7.5]$ are shown. The result of the simultaneous fit are overlaid. The pulls of the fit are shown in the bottom part.

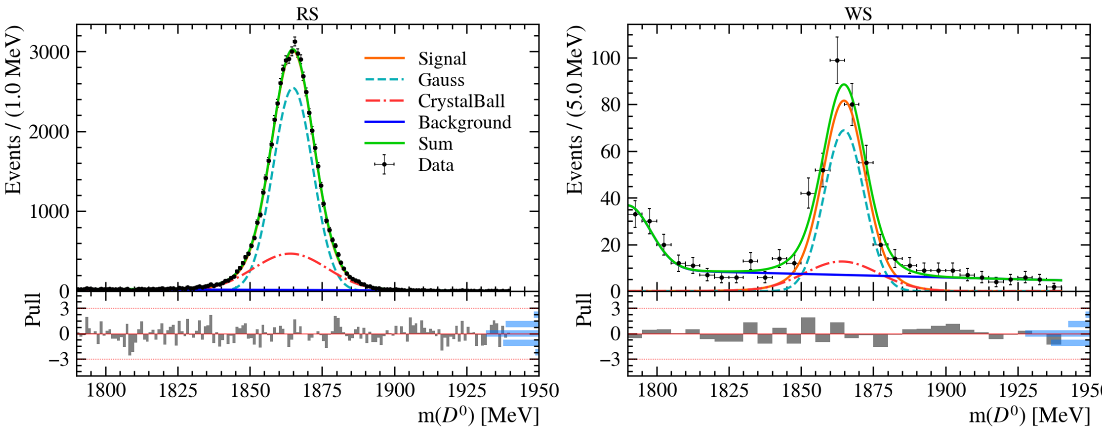

Figure B.10: The Δm distributions of the RS and WS semileptonic tagged samples in the decay time integrated measurement $\Gamma t \in [0.1, 7.5]$ are shown. The result of the simultaneous fit are overlaid. The pulls of the fit are shown in the bottom part.

C Appendix: Secondary D decays

The fits to calculate the secondary decay contamination are shown below.

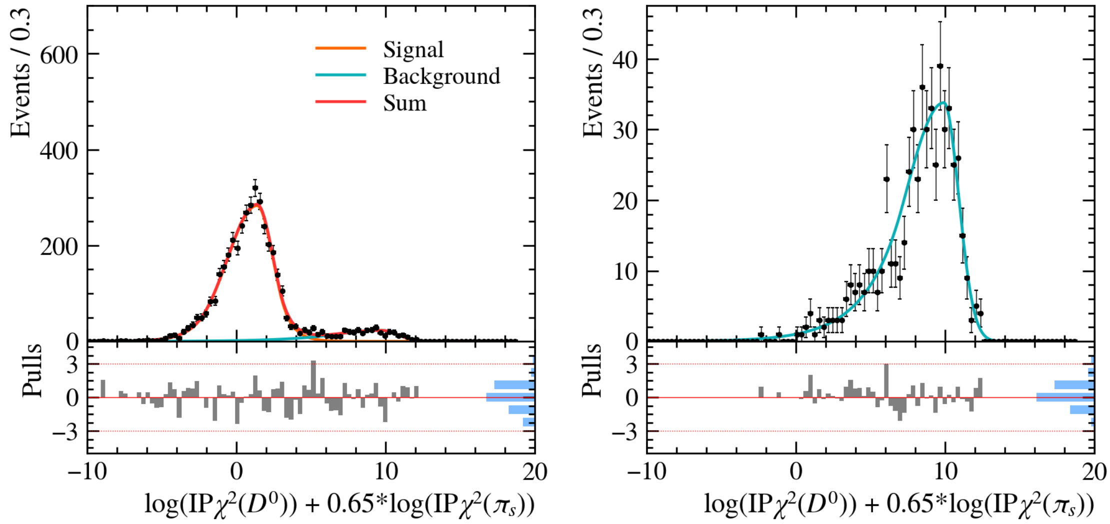

Figure C.1: First decay time bin $t_{D^0}/\tau \in [2.2, 5.3]$. Left: Fit to the signal region $\Delta m \in [144.7, 146.3]\,\mathrm{MeV}/c^2$. Right: Fit to the sideband $\Delta m \in [141.5, 142.5]\,\mathrm{MeV}/c^2$.

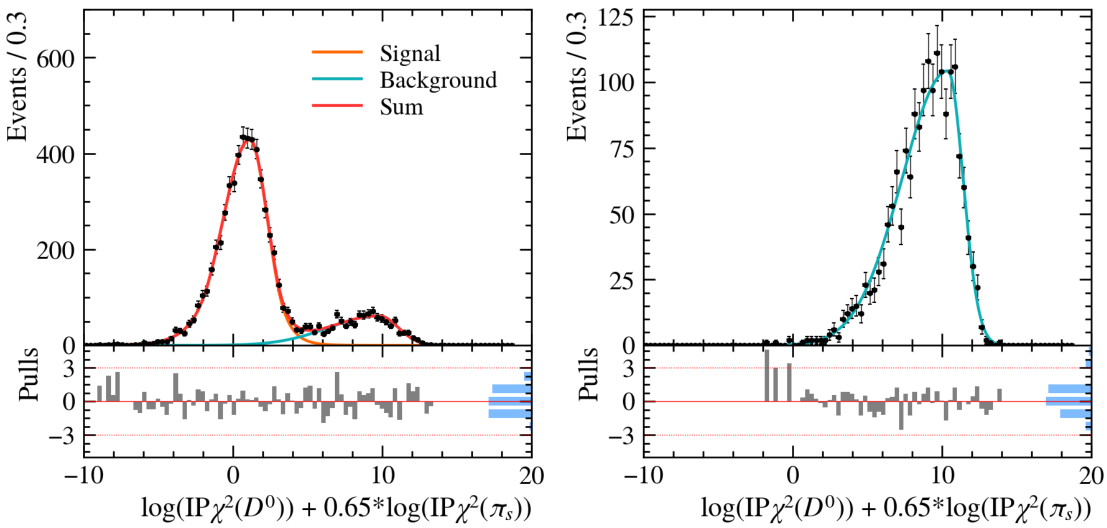

Figure C.2: Second decay time bin $t_{D^0}/\tau \in [5.3, 6.6]$. Left: Fit to the signal region $\Delta m \in [144.7, 146.3]\,\text{MeV}/c^2$. Right: Fit to the sideband $\Delta m \in [141.5, 142.5]\,\text{MeV}/c^2$.

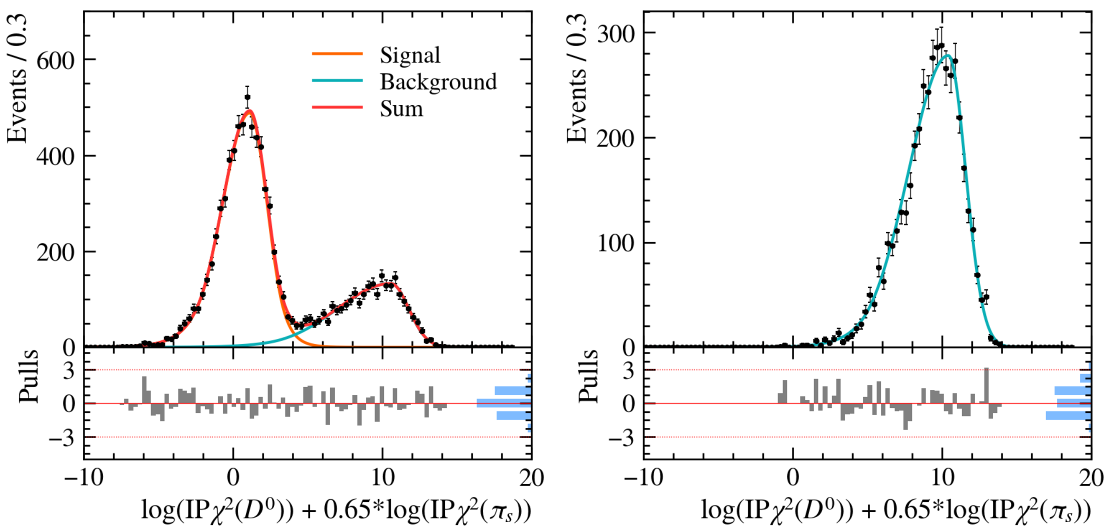

Figure C.3: Third decay time bin $t_{D^0}/\tau \in [6.6, 8.2]$. Left: Fit to the signal region $\Delta m \in [144.7, 146.3]\,\text{MeV}/c^2$. Right: Fit to the sideband $\Delta m \in [141.5, 142.5]\,\text{MeV}/c^2$.

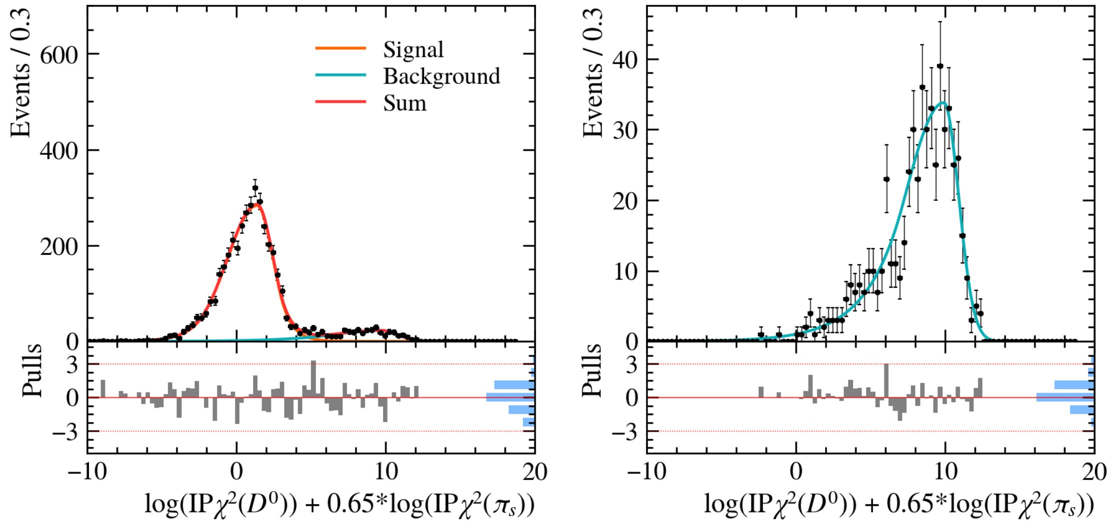

Figure C.4: Fourth decay time bin $t_{D^0}/\tau \in [8.2, 15.0]$. Left: Fit to the signal region $\Delta m \in [144.7, 146.3]\,\mathrm{MeV}/c^2$. Right: Fit to the sideband $\Delta m \in [141.5, 142.5]\,\mathrm{MeV}/c^2$.

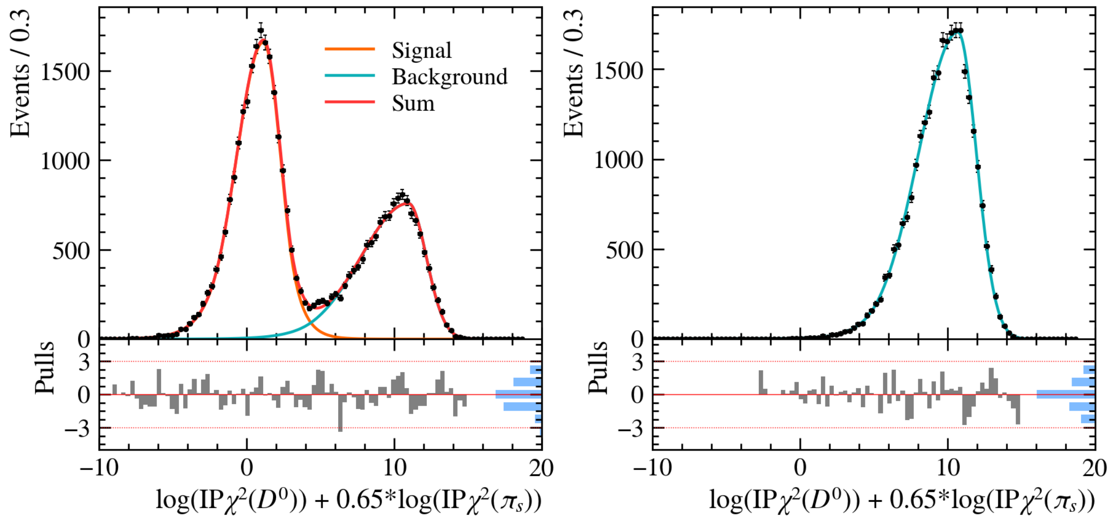

Figure C.5: Decay time-integrated $t_{D^0}/\tau \in [8.2, 15.0]$. Left: Fit to the signal region $\Delta m \in [144.7, 146.3]\,\mathrm{MeV}/c^2$. Right: Fit to the sideband $\Delta m \in [141.5, 142.5]\,\mathrm{MeV}/c^2$.

D Lists

D.1 List of Figures

D.2 List of Tables

E Bibliography

[1] G. D. Rochester and C. C. Butler, *Evidence for the existence of new unstable elementary particles*, Nature **160** (1947) 855.

[2] M. Gell-Mann and A. Pais, *Behavior of neutral particles under charge conjugation*, Phys. Rev. **97** (1955) 1387.

[3] A. Pais and O. Piccioni, *Note on the decay and absorption of the* θ^0, Phys. Rev. **100** (1955) 1487.

[4] R. H. Good *et al.*, *Regeneration of neutral K mesons and their mass difference*, Phys. Rev. **124** (1961) 1223.

[5] J. H. Christenson, J. W. Cronin, V. L. Fitch, and R. Turlay, *Evidence for the 2π decay of the k_2^0 meson*, Phys. Rev. Lett. **13** (1964) 138.

[6] H. Albrecht *et al.*, *Observation of b0-b0 mixing*, Physics Letters B **192** (1987) 245.

[7] CDF Collaboration, A. Abulencia *et al.*, *Observation of $B_s^0 - \overline{b}_s^0$ oscillations*, Phys. Rev. Lett. **97** (2006) 242003.

[8] LHCb collaboration, R. Aaij *et al.*, *Observation of D^0–$\overline{D}^0$ oscillations*, Phys. Rev. Lett. **110** (2013) 101802, `arXiv:1211.1230`.

[9] Particle Data Group, P. A. Zyla *et al.*, *Review of particle physics*, Prog. Theor. Exp. Phys. **2020** (2020) 083C01.

[10] F. Englert and R. Brout, *Broken symmetry and the mass of gauge vector mesons*, Phys. Rev. Lett. **13** (1964) 321.

[11] P. W. Higgs, *Broken symmetries and the masses of gauge bosons*, Phys. Rev. Lett. **13** (1964) 508.

[12] N. Cabibbo, *Unitary symmetry and leptonic decays*, Phys. Rev. Lett. **10** (1963) 531.

[13] M. Kobayashi and T. Maskawa, *CP-violation in the renormalizable theory of weak interaction*, Prog. Theor. Phys. **49** (1973) 652.

[14] L. Wolfenstein, *Parametrization of the kobayashi-maskawa matrix*, Phys. Rev. Lett. **51** (1983) 1945.

[15] V. Weisskopf and E. P. Wigner, *Calculation of the natural brightness of spectral lines on the basis of Dirac's theory*, Z. Phys. **63** (1930) 54.

[16] V. Weisskopf and E. Wigner, *Over the natural line width in the radiation of the harmonius oscillator*, Z. Phys. **65** (1930) 18.

[17] M. S. Sozzi, *Discrete symmetries and CP violation: From experiment to theory*, Oxford University Press, 2008.

[18] LHCb collaboration, R. Aaij *et al.*, *Observation of the mass difference between neutral charm-meson eigenstates*, Phys. Rev. Lett. **127** (2021) 111801, arXiv:2106.03744.

[19] Y. Amhis *et al.*, *Averages of b-hadron, c-hadron, and τ-lepton properties as of 2021*, arXiv:2206.07501.

[20] L. Evans and P. Bryant, *LHC machine*, Journal of Instrumentation **3** (2008) S08001.

[21] E. Lopienska, *The CERN accelerator complex, layout in 2022. Complexe des accélérateurs du CERN en janvier 2022*, , General Photo.

[22] LHCb collaboration, A. A. Alves Jr. *et al.*, *The LHCb detector at the LHC*, JINST **3** (2008) S08005.

[23] LHCb collaboration, R. Aaij *et al.*, *LHCb detector performance*, Int. J. Mod. Phys. **A30** (2015) 1530022, arXiv:1412.6352.

[24] LHCb collaboration, Christian Elsässer, *$\bar{b}b$ production angle plots*, https://lhcb.web.cern.ch/lhcb/speakersbureau/html/bb_ProductionAngles.html.

[25] R. Lindner, *LHCb layout*, https://cds.cern.ch/record/1087860, 2008. LHCb Collection.

[26] R. Aaij *et al.*, *Performance of the LHCb Vertex Locator*, JINST **9** (2014) P09007, arXiv:1405.7808.

[27] LHCb Collaboration, W. Baldini *et al.*, *Overview of LHCb alignment*, doi: 10.5170/CERN-2007-004.197.

[28] R. Aaij *et al.*, *Performance of the LHCb trigger and full real-time reconstruction in Run 2 of the LHC*, JINST **14** (2019) P04013, arXiv:1812.10790.

[29] R. Aaij *et al.*, *A comprehensive real-time analysis model at the LHCb experiment*, JINST **14** (2019) P04006, arXiv:1903.01360.

[30] LHCb collaboration, R. Aaij *et al.*, *Updated determination of D^0–$\overline{D}^0$ mixing and CP violation parameters with $D^0 \to K^+\pi^-$ decays*, Phys. Rev. **D97** (2018) 031101, arXiv:1712.03220.

[31] M. Artuso, B. Meadows, and A. A. Petrov, *Charm meson decays*, Annual Review of Nuclear and Particle Science **58** (2008) 249.

[32] G. Burdman and I. Shipsey, - *mixing and rare charm decays*, Annual Review of Nuclear and Particle Science **53** (2003) 431.

[33] S. Bianco, F. L. Fabbri, D. Benson, and I. Bigi, *A cicerone for the physics of charm*, La Rivista del Nuovo Cimento **26** (2004) 1200.

[34] G. Blaylock, A. Seiden, and Y. Nir, *The role of CP violation in mixing*, Physics Letters B **355** (1995) 555.

[35] LHCb collaboration, R. Aaij *et al.*, *Search for dark photons produced in 13 TeV pp collisions*, Phys. Rev. Lett. **120** (2018) 061801, arXiv:1710.02867.

[36] M. Alexander *et al.*, *Mapping the material in the LHCb vertex locator using secondary hadronic interactions*, JINST **13** (2018) P06008, arXiv:1803.07466.

[37] T. Chen and C. Guestrin, *XGBoost: A scalable tree boosting system*, in *Proceedings of the 22nd ACM SIGKDD International Conference on Knowledge Discovery and Data Mining*, KDD '16, (New York, NY, USA), 785–794, ACM, 2016.

[38] R. Aaij *et al.*, *Tesla: an application for real-time data analysis in High Energy Physics*, Comput. Phys. Commun. **208** (2016) 35, arXiv:1604.05596.

[39] W. D. Hulsbergen, *Decay chain fitting with a Kalman filter*, Nucl. Instrum. Meth. **A552** (2005) 566, arXiv:physics/0503191.

[40] P. Koppenburg, *Statistical biases in measurements with multiple candidates*, arXiv:1703.01128.

[41] LHCb collaboration, R. Aaij *et al.*, *Observation of CP violation in charm decays*, Phys. Rev. Lett. **122** (2019) 211803, arXiv:1903.08726.

[42] F. Archilli *et al.*, *Performance of the muon identification at LHCb*, JINST **8** (2013) P10020, arXiv:1306.0249.

[43] J. Eschle, A. Puig Navarro, R. Silva Coutinho, and N. Serra, *zfit: Scalable pythonic fitting*, SoftwareX **11** (2020) 100508.

[44] N. L. Johnson, *Systems of frequency curves generated by methods of translation*, Biometrika **36** (1949) 149.

[45] H. Albrecht *et al.*, *Search for hadronic bu decays*, Physics Letters B **241** (1990) 278.

[46] M. Oreglia, *A Study of the Reactions $\psi' \to \gamma\gamma\psi$*, other thesis, 1980.

[47] G. A. Cowan, D. C. Craik, and M. D. Needham, *RapidSim: an application for the fast simulation of heavy-quark hadron decays*, Comput. Phys. Commun. **214** (2017) 239, `arXiv:1612.07489`.

[48] CDF Collaboration, A. Abulencia *et al.*, *Observation of $B_s^0 \to K^+K^-$ and measurements of branching fractions of charmless two-body decays of B^0 and B_s^0 mesons in $\overline{p}p$ collisions at $\sqrt{s} = 1.96$ TeV*, Phys. Rev. Lett. **97** (2006) 211802.

[49] LHCb collaboration, R. Aaij *et al.*, *Measurement of CP asymmetry in $D^0 \to K^-K^+$ and $D^0 \to \pi^-\pi^+$ decays*, JHEP **07** (2014) 041, `arXiv:1405.2797`.

[50] LHCb collaboration, R. Aaij *et al.*, *Search for direct CP violation in $D^0 \to h^-h^+$ modes using semileptonic B decays*, Phys. Lett. **B723** (2013) 33, `arXiv:1303.2614`.

[51] LHCb Collaboration, *Model-independent measurement of charm mixing parameters in $\bar{B} \to D^0(\to K_S^0\pi^+\pi^-)\mu^-\bar{\nu}_\mu X$* , CERN, Geneva, 2022. All figures and tables, along with any supplementary material and additional information, are available at https://cern.ch/lhcbproject/Publications/p/LHCb-PAPER-2022-020.html (LHCb public pages).

[52] LHCb collaboration, R. Aaij *et al.*, *Measurement of D^0–$\overline{D}^0$ mixing parameters and search for CP violation using $D^0 \to K^+\pi^-$ decays*, Phys. Rev. Lett. **111** (2013) 251801, `arXiv:1309.6534`.

[53] LHCb collaboration, R. Aaij *et al.*, *Measurements of prompt charm production cross-sections in pp collisions at $\sqrt{s}$ =13 TeV*, JHEP **03** (2016) 159, Erratum ibid. **09** (2016) 013, Erratum ibid. **05** (2017) 074, `arXiv:1510.01707`.

[54] G. Amelino-Camelia and J. I. Kapusta, *Neutral Kaon System in Dense Matter and Heavy-Ion Collisions*, Phys. Lett. B **465** (1999) 291.

F Acknowledgements

This master thesis needed many people to make it happen, and all of them deserve my thanks.

I want to express my gratitude to Prof. Stephanie Hansmann-Menzemer for supervising my thesis and encouraging me to pursue this exciting project with the University of Manchester. Without your extraordinary support of this thesis, it would not have been possible. In many ways, you're responsible for getting me into particle physics.

My sincerest thanks go to Prof. Marco Gersabeck for suggesting this exciting topic and welcoming me into the LHCb Manchester group. I appreciate the effort it took to organise and supervise this thesis. You allowed me to investigate my own ideas while still getting me back on the right path when I strayed too far.

This thesis and my studies are generously supported by the Studienstiftung des deutschen Volkes.

I want to thank Aodhán Burke, Dr. Adam Davis, Dr. Evelina Mihova Gersabeck and Prof. Marco Gersabeck for our weekly discussions. Your feedback and expertise were invaluable.

My gratitude goes to the whole LHCb Manchester group and the HEP postgraduate community in Manchester for their warm welcomes.

Ohne die Unterstützung meiner Eltern wäre mein Studium nicht möglich gewesen. Vielen Dank für eure Ermutigung und Untersützung!

Thank you! Danke!

G Deposition

Erklärung:

Ich versichere, dass ich diese Arbeit selbstständig verfasst habe und keine anderen als die angegebenen Quellen und Hilfsmittel benutzt habe.

Heidelberg, den 07.10.2022 ....